Studies on microstructural and mechanical properties of Ti-15V-3Al-3Cr-3Sn electron beam and gas tungsten arc welds

A
Synopsis
of the thesis to be submitted in partial fulfillment of the requirements
for the award of the degree of

DOCTOR OF PHILOSOPHY

by

KARNI VAMSI KRISHNA
(Roll No.718149)

Supervisor

Dr. NAGUMOTHU KISHORE BABU

DEPARTMENT OF METALLURGICAL AND MATERIALS ENGINEERING
NATIONAL INSTITUTE OF TECHNOLOGY WARANGAL

August 2023

Dedicated to My Parents

DEPARTMENT OF METALLURGICAL AND MATERIALS ENGINEERING

NATIONAL INSTITUTE OF TECHNOLOGY

WARANGAL-506004, INDIA.

CERTIFICATE

This is to certify that the work presented in the thesis entitled "**Studies on microstructural and mechanical properties of Ti-15V-3Al-3Cr-3Sn electron beam and gas tungsten arc welds"** which is being submitted by **Mr. Karni Vamsi Krishna** (Roll No. 718149), is a bonafide work submitted to National Institute of Technology, Warangal in partial fulfillment of the requirement for the award of the degree of **Doctor of Philosophy** in Metallurgical and Materials Engineering.

To the best of our knowledge, the work incorporated in the thesis has not been submitted to any other university or institute for the award of any degree or diploma.

Date:

Dr. N. Kishore Babu
Thesis Supervisor
Associate Professor
Department of Metallurgical and Materials Engineering
National Institute of Technology, Warangal, India.

DEPARTMENT OF METALLURGICAL AND MATERIALS ENGINEERING

NATIONAL INSTITUTE OF TECHNOLOGY

WARANGAL-506004, INDIA.

DECLARATION

This is to certify that the work presented in the thesis entitled "**Studies on microstructural and mechanical properties of Ti-15V-3Al-3Cr-3Sn electron beam and gas tungsten arc welds**", is a bonafide work done by me under the supervision of Dr. N. Kishore Babu and was not submitted elsewhere for the award of any degree.

I declare that this written submission represents my idea in my own words and where other's ideas or words have not been included. I have adequately cited and referenced the original sources. I also declare that I have adhered to all principles of academic honesty and integrity and have not misinterpreted or fabricated or falsified any idea/data/fact/source in my submission. I understand that any violation of the above will be a cause for disciplinary action by the Institute and can also evoke penal action from the sources that have thus not been properly cited or from whom proper permission has not been taken when needed.

Date:

Place:

(Mr. K. Vamsi Krishna)

Research Scholar

Roll No. 718149

ACKNOWLEDGMENTS

It is my pleasant duty to acknowledge the people who have helped me during the tenure of the research work reported in the present thesis.

I express special gratitude to my supervisor and mentor **Dr. N. Kishore Babu**, Associate Professor, Department of Metallurgical and Materials Engineering (MMED), National Institute of Technology Warangal for his inspiring guidance, keen interest, motivation, involvement, and constant supervision throughout the course of this work and preparation of the thesis. Without his patient mentorship, constant inspiration, valuable discussions, and suggestions, this thesis would not have been possible.

I am grateful to Prof. Bidyadhar Subudhi, Director, of NIT Warangal for giving me an opportunity to carry out research work at the institute. Additionally, I wish to express my gratitude to Prof. N. V. Ramana Rao, former Director, of NIT Warangal affording me the chance to pursue research within the institute.

Besides my supervisor, I take this privilege to thank all my Doctoral Committee (DSC) members Prof. Mahesh Kumar Talari, Professor (Chairman, MMED), Dr. Sreedevi .V, Assistant professor (MMED), Dr. Rangadhara Chary V (MMED) and Prof. Joseph Davidson M, Professor (Department of Mechanical Engineering) for their useful suggestions and periodical review of my progress during this course of PhD work. I also would like to thank all the faculty members of MMED for their support and help during the course of PhD.

I would like to express my sincere thanks to Dr. P. Mastanaiah (Scientist 'F', Head, Special Fabrication Division, DRDL Hyderabad) for providing the research facilities required during my Ph. D work. I also thank Mr. Chaudhary (DMRL, Hyderabad) for his help in metal fabrication work during this research work.

I would also express my sincere thanks to Dr. Bharat Bandi (Warwick University, UK) for carrying out Electron Backscatter Diffraction (EBSD) and Dr. Sriharitha Rowthu (IIT Gandhinagar, India) for carrying out the Transmission Electron Microscopy (TEM). X-ray diffraction.

I thank the help of the technical staff and office staff of the Metallurgical and Materials Engineering Department, NIT Warangal for their help during this research work.

I take this opportunity to acknowledge with sincere gratefulness to my friends and colleagues Mr. C. Gopi Krishna, Mr. Md. Jawed Quamar, Mr. P. Anil Kumar, Mr. G. Dhamodar Naidu,

Mr. Kiran, Mr. C. Krishna Teja and all present and past research scholars of NIT Warangal for their valuable assistance and support during this research work.

Finally, I express my sincere thankfulness to my family for their love, patience and encouragement.

K. Vamsi Krishna

ABSTRACT

The main aim of the current investigation was to study the microstructural features and mechanical properties, such as hardness and tensile strength of Ti-15V-3Al-3Cr-3Sn (Ti-15-3) weldments created through electron beam welding (EBW) and gas tungsten arc welding (GTAW) at varying welding speeds. Additionally, investigated the effect of Nickel (Ni) and Silicon (Si) modified fillers on microstructural and mechanical characteristics of Ti-15-3 welds during GTAW. The studies made on weldments in as-welded and post-weld heat treatment (PWHT) conditions.

Ti-15-3 alloy sheets of 3mm thickness received in the form of solution treated condition, were used in the present investigation. Autogenous full penetration bead-on-plate EB welds (by varying welding speeds - 500, 700, and 800 mm/min) and GTA welds (by varying welding speeds - 15, 20, and 25 cm/min) were made on coupons. In order to obtain complete penetration several initial trails were made with varying heat input in both welding processes. Also, welds prepared using Ni and Si modified fillers on Ti-15-3 coupons by GTAW. The varying compositions of prepared fillers are Ti-15-3-xNi (x = 0.15, 0.3, 0.5) and Ti-15-3-xSi (x = 0.15, 0.3, 0.5), respectively. Tensile test specimens were fabricated by electric discharge machining (EDM). Few tensile test specimens were subjected to a PWHT of pre-aging at 300°C for 4 h, followed by aging at 500°C for 7 h in vacuum atmosphere and furnace cooled to room temperature.

Microstructural observations were made by light microscope, scanning electron microscope (SEM) and transmission electron microscope (TEM). Mechanical properties were made by hardness and tensile testing. Hardness was measured across the weldments. Tensile tests were carried out on transverse weld samples at room temperature. The fractured surfaces of tensile tested samples were examined in a SEM.

The microstructure of the fusion zone (FZ) in the as-welded condition, revealed a coarse columnar β grains and the heat-affected zone (HAZ) displays coarse equaixed β grains in both EB and GTA welds. Conversely, the base metal (BM) retains fine equaixed β grains across all welding speeds in both welding conditions. The average width of the fusion zone (FZ) decreased with an increase in welding speed in both cases, primarily due to reduced heat input and increased cooling rates. The EB welds produced at a higher welding speed of 800 mm/min

resulted in greater ultimate tensile strength (UTS) at 751 MPa and increased hardness at 245 HV, surpassing the values obtained from welds produced at a lower welding speed of 500 mm/min, with UTS at 670 MPa and hardness at 235 HV. A similar trend has been observed in welds made subjected to GTAW. The GTAW welds prepared at a higher welding speed (25 cm/min) exhibited superior UTS of 654 ± 5 MPa and hardness measuring 240 HV, surpassing the performance of welds produced at a lower speed (15 cm/min), which had a UTS of 593 ± 5 MPa and hardness of 230 HV. The enhanced strength observed at the higher welding speed can be attributed to the reduced width of columnar β grains and the development of equiaxed grains at both the weld root and center in both welding conditions. The welds after PWHT exhibited a significant rise in UTS and hardness but expense of ductility. However, this increase in UTS and hardness attributed to the presence of uniform α precipitates within the β matrix, as confirmed by TEM analysis.

Microstructural examination of welds with Ni and Si modified fillers revealed equaixed grains and refined prior-β grains and characterized by nonlinear grain boundaries within the FZ. The welds prepared using Ti-15-3-0.5 Ni filler exhibited a yield strength (YS) of 688 ± 6 MPa, UTS of 721 ± 5 MPa, and % elongation (%El) of 9 ± 0.5% and Ti-15-3-0.5 Si filler (YS = 693 ± 6 MPa, UTS = 725 ± 5 MPa, %El = 8 ± 0.5%) showed higher strength compared to autogenous weld (YS = 575 ± 4 MPa, UTS = 597 ± 4 MPa, %El = 11 ± 0.5%). The increased strength in welds produced using Ti-15-3-0.5 Ni filler and Ti-15-3-0.5 Si filler can be ascribed to the reduced columnar width of β grains and the development of equiaxed grains within the FZ. A significant enhancement in both UTS and hardness were evident in samples that underwent PWHT of weldments, as compared to the as-welded specimens.

Keywords: Gas tungsten arc welding, Electron beam welding, post-weld two-step aging, Ti-15V-3Al-3Cr-3Sn, Tensile strength, and hardness.

LIST OF TABLES

LIST OF FIGURES

ABBREVIATIONS

EBW	Electron beam welding
GTAW	Gas tungsten arc welding
PWHT	Post-weld heat treatment
SEM	Scanning electron microscope
TEM	Transmission electron microscope
FZ	Fusion zone
HAZ	Heat-affected zone
CP-Ti	Commercial pure titanium
BM	Base metal
UTS	Ultimate tensile strength
YS	Yield strength
CET	Columnar to equiaxed transition
XRD	X-ray diffractometry
EBSD	Electron backscatter diffraction
BCC	Body centred cubic
HCP	Hexagonal close packed
MoE	Molybdenum Equivalency
GMAW	Gas metal arc welding
LBW	Laser beam welding
PAW	Plasma arc welding
DC	Direct current
AC	Alternating current
P-GTAW	Pulsed GTAW
C-GTAW	Conventional GTAW
CCT	Continuous cooling transformation
TTT	Time-temperature transformation
GRF	Growth restriction factor
LAAM	Laser-aided additive manufacturing
UTM	Universal testing machine
HF	Hydrofluoric acid
EDS	Energy dispersive spectroscopy
EDM	Electro-discharge wire-cut machine
IPF	Inverse pole figure
CSZ	Constitutionally supercooled zone

NOTATIONS

O	Oxygen
H	Hydrogen
N	Nitrogen
β	beta
α	alpha
R	growth rate
R	thermal gradient
Ti	Titanium
Be	Beryllium
B	Boron
C	Carbon
Ni	Nickle
Si	Silicon
Sc	Scandium
°C	Centigrade
h	Hour
K	Kelvin
wt. %	Weight percentage
cm	Centimetre
mm	Millimetre
min	Minute
V	Vanadium
Al	Aluminium
Sn	Tin
Mo	Molybdenum
Zr	Zirconium
α'	Alpha prime
α''	Alpha double prime
β'	Beta prime
ω	Omega
M_s	Martensitic start
ω_a	athermal omega
ω_{iso}	isothermal omega
Cr	Chromium
La	Lanthanum
Fe	Iron
He	Helium
Ar	Argon
I_b	background current
I_p	peak current
T_p	Peak Time
T_b	background current
θ_p	fraction of time at peak current
S/L	solid-liquid
m	liquidus line slope
k	partition coefficient of solute

C_l	solute contents of the liquid
C_s	solute contents of the solid
C_o	solute content of the alloy
Q	Growth restriction factor
D	diffusion coefficient
ΔT_n	undercooling parameter
ρ	Density
f	Fraction
d	Grain size
kV	Kilo volt
MPa	Mega pascal
kJ	Kilo joule
mA	Milli ampere
Hz	Hertz
µm	Micrometre
s	Second
g	gram
P	Load
dl	diagonal length
kg	Kilogram
kN	Kilo newton
HV	Vickers Pyramid Number
Wm^{-2}	Weber per meter square

Contents

Page No.

1. INTRODUCTION

1.1 Background of the study:

Titanium (Ti) stands as a robust and lightweight refractory metal. Its alloys find extensive application in numerous sectors such as aerospace, medical, automotive, biomedical, and petrochemical industries. This prevalence is owed to their exceptional qualities, including low density, high strength, corrosion resistance, favorable fatigue properties, and biocompatibility. [1]. These alloys also exhibit a low coefficient of thermal expansion and low coefficient of thermal conductivity which can tolerate high temperatures making these alloys well-suited for high-temperature applications [2]. As Ti alloys are relatively expensive, there is a need to minimize the cost of processing and shaping for manufacturing of industrial components. One of the economic ways to achieve this is through efficient welding of Ti alloys. But welding of titanium alloys is difficult as these alloys are more susceptible to gases elements such as oxygen (O), hydrogen (H), and nitrogen (N) above 500 °C which diminish the mechanical properties. Therefore, the main conditions to be fulfilled for welding titanium alloys are protecting the weld zone from contamination by providing an inert or vacuum atmosphere [3]. GTAW and EBW are usually preferred welding techniques for Ti alloys due to their ease of application for producing clean and high-quality welds.

Titanium (Ti) exhibits an allotropic transformation, transitioning from the body-centered cubic (bcc) beta (β) phase at elevated temperatures to the hexagonal-close packed (hcp) alpha (α) phase at lower temperatures. Generally, for commercial pure titanium (CP-Ti) this transformation occurs at 882 ˚C. The transformation temperature is influenced by the presence of substitutional and interstitial alloying elements in the material. The elements which will stabilize the α phase at high temperatures are known as α stabilizers (O, C, N, Al, etc.) whereas the elements which will stabilize the β phase at low temperatures are known as β stabilizers (Mo, V, Cr, Ni, Nb, etc.). The neutral elements (Sn, Zr) have only a minor influence on the β-transus temperature [4]. It was often said that stability of β-phase is described in terms of molybdenum equivalency (MoE = [Mo] + 0.2[Ta] + 0.28[Nb] + 0.4[W] + 0.67[V] + 1.25[Cr] +1.25[Ni] + 1.7[Mn]

+ 1.7[Co] + 2.5[Fe] (all the elements correspond to their respective wt. %)). This MoE range of 8 – 30 wt. % are termed as metastable β-Ti alloys and beyond which termed as stable β-Ti alloys. Both metastable and stable β-Ti alloys contain sufficient amounts of β stabilizers to suppress the transformation of martensitic phase and to retain the bcc crystal structure on quenching (or) even after rapid cooling to room temperature [5]. The alloy chosen for this current study is a metastable β-Ti alloy, Ti-15V-3Cr-3Al-3Sn (Ti-15-3) with a MoE of 10.9%.

1.2 Problem statement:

The Weld FZ microstructure of metastable β-Ti alloy exhibits coarse columnar grains due to thermal cycles experienced during welding. These coarse columnar grains in FZ adversely affect the tensile strength of these β-Ti welds in relation to the BM [6]. Hence, grain refinement in the FZ from coarse columnar to equiaxed transition (CET) is necessary to improve weld performance. Fine equiaxed grains in the weldment promote the superior response on mechanical properties and also reduce the segregation effects [7]. Numerous techniques have been documented to enhance the β grain size within the FZ of Ti weldments. These approaches encompass methods such as arc manipulation, pulsed current welding, inoculation, vibration techniques, electromagnetic stirring, filler material modification, introduction of nucleating agents, and control of welding speed and current, among others [8-12]. However PWHT was thus becomes necessary to improve the weld strength to an acceptable level [13].

The welding speed constitutes a critical welding parameter with a direct impact on both the cooling rate (calculated as the product of growth rate R and thermal gradient G) and the heat input. The control of welding speed in the both GTAW and EBW may lead to metallurgical advantages, which include control of segregation in the weld zone, reduced width of the HAZ, fine grain structure in the FZ, etc., which altogether can enhance the mechanical properties of weld [14]. Also, inherent properties of the EBW technique, such as a high depth-to-width ratio and protection of weld from contamination by creating a vacuum leading to cleaner welds, make it stand out. EBW also offers additional advantages like higher cooling rates, reduced heat input, and the capability to weld various plate thicknesses without the need for any filler material [15]. However, EBW can produce high-quality welds, but the operational costs of these processes are high as compared to GTAW. The strength and ductility can be improved

by varying the welding parameters like pulsing, welding speed. This results in varying heat input during solidification leading to thermal fluctuations, resulting in periodic interruptions in the grain growth process. As a consequence, the FZ β-grain microstructure is significantly refined. The reduction in grain size results in enhanced strength and ductility of the weldments in their as-welded condition [16, 17].

An alternative approach for avoiding the FZ grain coarsening of metastable β-Ti alloys could be filler modification [18]. The addition of insoluble elements such as Beryllium (Be), Boron (B), Carbon (C), Nickle (Ni), and Silicon (Si) to cast titanium alloys can modify the as-cast microstructure and grain size [19-21]. A study has been done on GTAW of Ti-15-3 using B and C-modified Ti-15-3 fillers observed significant refinement of β grain size in FZ thereby improving strength [22]. Similarly, Deng et al. [23] also investigated the influence of traces of Si and Scandium (Sc) addition on grain size refinement during the vacuum arc melting of Ti-6Al-4V (Ti-64) alloy. They found that both Si and Sc play a prominent role in grain refinement as well as improve the creep resistance of the alloy.

The strengthening of metastable β-Ti-alloy welds can also be achieved by uniform dispersion of fine α precipitates in the β matrix, which can be accomplished by suitable PWHT. The studies of Lin et al. [24] on the EBW of Ti-15-3 have reported the PWHT at 538°C for 8 h resulted in higher tensile strength compared to the as-welded condition. This phenomenon is associated with the emergence of small nano α precipitates within the FZ. A similar findings has been observed by Balachander et al. [16] and Becker and Baeslack [25] in GTA welds of Ti-15-3 subjected to PWHT. However, few studies have revealed that the two-step aging results in the formation of a more uniform and fine precipitation of α phase compared to the single-step aging treatment and results in the improvement of the mechanical properties of metastable β Ti alloys [26][27]. For instance, Yumak et al. [28] demonstrated that two-step aging (523 K, 10 h + 723 K, 20 h) of the Ti-15-3 alloy leads to the formation of fine α precipitates uniformly distributed in β matrix as compared to single-step aging (823 K, 10 h). They showed the increase in hardness is due to duplex aging of the alloy. Similar findings have been made by Kuroda et al. [29] while studying the age-hardening behavior of Ti-15-3 welded by GTAW. They reported a high degree of hardening in duplex aging (673 K, <8 h + 773 K, 24 h). Recently, Santosh et al. [30] have also proved that duplex aging of Ti-15-3 alloy resulted in better fatigue life because of a higher density of α precipitation.

From the aforementioned literature, it is evident that limited research work has been done on the EBW and GTAW of Ti-15-3 alloy, and the effect of welding speed on the mechanical behaviour of welds is rarely studied. Also, there is a paucity of information concerning the GTAW of Ti alloys utilizing Ni and Si-modified fillers. Hence an attempt was made to study these aspects in this present work. All these studies were conducted on weldments in the as-welded as well as PWHT conditions.

The entire thesis consists of 8 chapters. In Chapter 1, an introduction to the thesis is presented, emphasizing the significance, objectives, and relevance of the work. Chapter 2 is dedicated to a thorough examination of the existing literature. This section encompasses a range of topics, including the physical metallurgy of Ti-15-3, the weldability of titanium alloys, welding parameters in processes such as EBW and GTAW, the grain refinement mechanism of Ti alloys, PWHT, and the correlation between microstructure and mechanical characteristics in β-Ti alloys. Chapter 3 provides an intricate overview of the experimental procedures carried out in the course of this study. Chapter 4, 5 and 6 extensively discusses the results and provides a thorough analysis of the various studies conducted within this research project. The conclusions drawn from the various parts of the current research are outlined in Chapter 7. Suggestions for future research avenues are listed in Chapter 8. A list of research papers that have been published based on the findings of this work are presented at the end.

1.3 Research objectives:

The aim of this study is to perform GTAW and EBW of Ti-15-3 metastable β titanium alloys and investigate the weld grain refining mechanisms, weld microstructure and mechanical behaviour with respect to the heat input, welding speed. To study the influence of filler modification on the grain refinement and properties, fillers with composition modification were prepared for GTA welding of Ti-15-3 metastable β titanium alloys. The research objectives, drawn from the problem statements outlined in Section 1.2, are as follows:

1. To determine the optimum welding speed that produces the highest grain refinement in EBW and GTAW of 3 mm thickness Ti-15-3 metastable β titanium alloy plates.

2. To study the influence of Ni and Si on grain refinement of Ti-15-3 GTA welds using Ti-15-3-x wt. % Ni/Si (x = 0.15, 0.3, 0.5 wt. %) modified fillers.
3. To investigate the effect of post-weld two-step aging treatment on Ti-15-3 EBW and GTAW welds at different welding speeds; GTAW welds prepared using Ni and Si added Ti-15-3 fillers, in terms of the morphology and distribution of α phase, and their influence on the mechanical properties.

1.4 Scope of research:

The scope of the research work is outlined as follows:

1. A metastable β titanium alloy, Ti-15-3 was used as a base metal and filler material for welding.
2. While welding Ti-15-3, the welding speed in GTAW is limited to 15 cm/min to 25 cm/min, whereas in the case of EBW is limited to 500 mm/min to 800 mm/min.
3. The Ni/Si modified fillers were prepared with the argon arc melting furnace on a water-cooled copper hearth. The filler composition is maintained as Ti-15-3-x wt. % Ni/Si (x = 0.15, 0.3, 0.5 wt. %) modified fillers.
4. Autogenous Ti-15-3 welds and welds prepared with Ti-15-3 modified fillers were performed by the pulsed GTAW method.
5. Post-weld two-step heat treatment (PWHT) of as-welded samples was carried out in a vacuum furnace.
6. Microstructural analysis methods comprised of X-ray diffractometry (XRD), optical microscopy (OM), transmission electron microscopy (TEM), scanning electron microscopy (SEM) and electron backscatter diffraction (EBSD).
7. Mechanical testing of welded samples involved a universal tensile test and Vickers hardness test. All mechanical tests were performed in accordance with the relevant ASTM standards.

2. LITERATURE REVIEW

2.1 Introduction:

Ti alloys are a class of metallic materials primarily composed of Ti, accompanied by other elements like Al, V, Cr etc. These alloys possess a unique combination of properties that render them valuable materials across diverse industries. Aerospace applications extensively use Ti alloys for components like landing gears, sheets and wings owing to their high tensile strength, good fatigue resistance, excellent toughness and other remarkable mechanical characteristics. These components often come in intricate shapes and can be single castings or complex fabrications. Welding is a common method used to produce individual components, followed by heat treatment when required. Due to the high material cost and strict geometrical tolerances in the aerospace industry, along with the growing pressure to reduce the duration of product manufacturing, continuous research in welding techniques has become essential. This ongoing research aims to address these challenges and further enhance the efficiency and reliability of aerospace component manufacturing.

2.2 Classification of titanium alloys:

Although pure Ti possess high ductility, it exhibits relatively low strength. Nevertheless, the metal becomes significantly more valuable when its strength is enhanced through alloying. The alloying elements are classified into four groups, determined by how they affect the ratios of the α and β phases below the β transus temperature, as shown in Fig 2.4. Based on the alloying elements the classification of Ti alloys as follows [31]:

- Alpha (α) alloys
- Near alpha alloys
- Alpha-beta (α-β) alloys
- Beta (β) alloys

α alloys: Aluminium (Al) serves as the primary alloying element in these alloys, along with tin, which has a minimal impact on the transformation temperature but imparts substantial solid solution strengthening. But Al content should not exceed 9% to prevent embrittlement. Oxygen (O) and Nitrogen (N) present as impurities give interstitial strengthening. These alloys exhibit good high-temperature stability but are not suitable for heat treatment to induce microstructural modifications. Ti-5Al-2.5Sn is one such alloy [31].

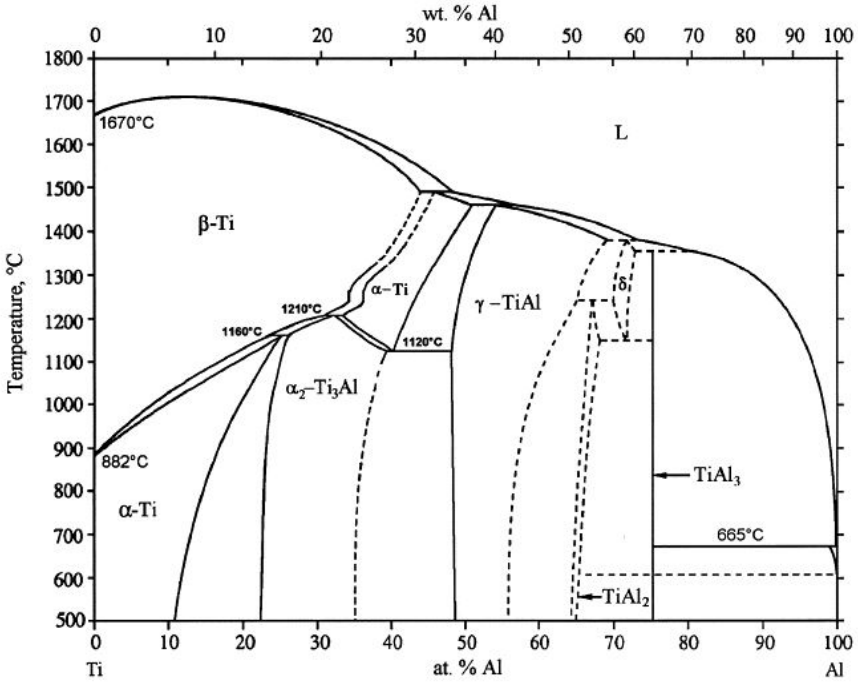

Fig 2.1: Ti-Al binary phase diagram [32]

Fig 2.1 shows the Ti-Al phase diagram contains various phases and phase boundaries that exist at various temperatures and compositions. At temperature (below 882°C) and low Al concentrations (typically less than about 8wt% Al) the Ti-Al alloy primarily consists of an α phase. Whereas at temperature (above 882°C) and higher Al concentrations (usually between about 8wt% and 40wt% Al), the alloy undergoes a phase transformation to a β phase. The development of Ti-Al alloys has arisen primarily because of their significant applications in components for automotive and aerospace engines. These alloys exhibit a superior specific modulus (elastic modulus per mass density) compared to that of other Ti alloys and Ni-based alloys. But welding of these alloys can be challenging, but with the right techniques, equipment, and precautions, it is possible to produce strong and reliable welds in these materials [33].

Near α alloys: These alloys contain a relatively small amount of β stabilizers, typically up to 2% by weight, which stabilize a small volume fraction of the β phase. As a result, they exhibit superior creep resistance when compared to other classes of titanium alloys. A significant number of these alloys also incorporate Silicon (Si) to further enhance their creep resistance [31].

α-β alloys: These alloys have a notable content of β stabilizers (around 4-6%) along with α stabilizers. Additionally, they might include Zirconium (Zr) and Tin (Sn) for solid solution

strengthening. Heat treatment is applicable to these alloys, for enhancing the mechanical properties. Compared to α -Ti alloys titanium alloys, they exhibit good strength and formability. However, their creep strength is lower than that of α-alloys. One of the most widely used alloys in this category is Ti-6Al-4V (Ti-64) [31].

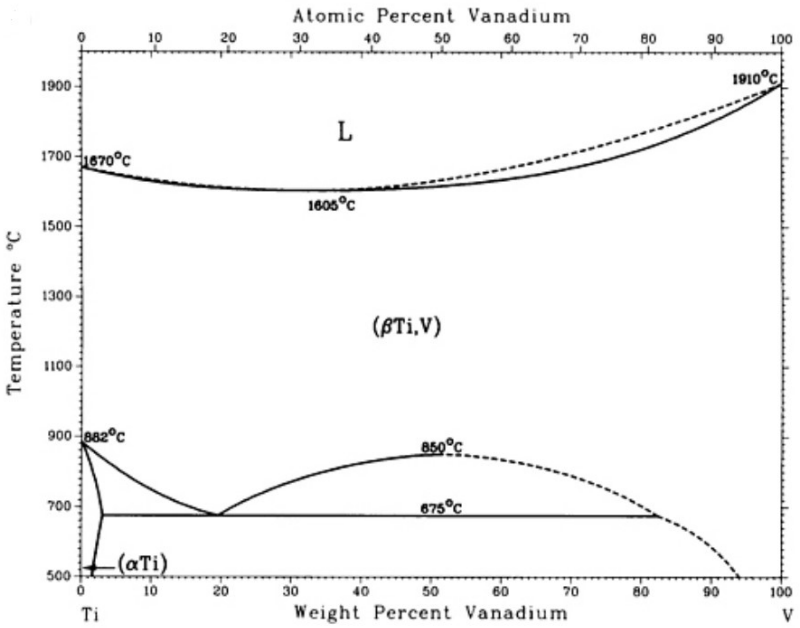

Fig 2.2: Ti-V phase diagram [32]

Numerous commercial titanium alloys designed for non-medical structural applications are rooted in titanium-vanadium (Ti-V) systems, as depicted in Fig 2.2. Examples include Ti–6Al–4V, Ti–15V–3Al–3Cr–3Sn and Ti–10V–2Fe–3Al chosen for their superior mechanical properties, lightweight characteristics, and cost-effectiveness. V exhibits significantly greater solubility in Ti compared to Mo, Nb, W, or Ta, all of which form analogous phase diagram characteristics. However, in most Ti-V alloys with higher V content, metastable phases (α' or α'') can readily form from the β phase, resulting in a higher Young's modulus but at expense of ductility. The addition of tin (Sn) to these alloys is anticipated to lower the Young's modulus while enhancing strength, making them more suitable for structural applications [34].

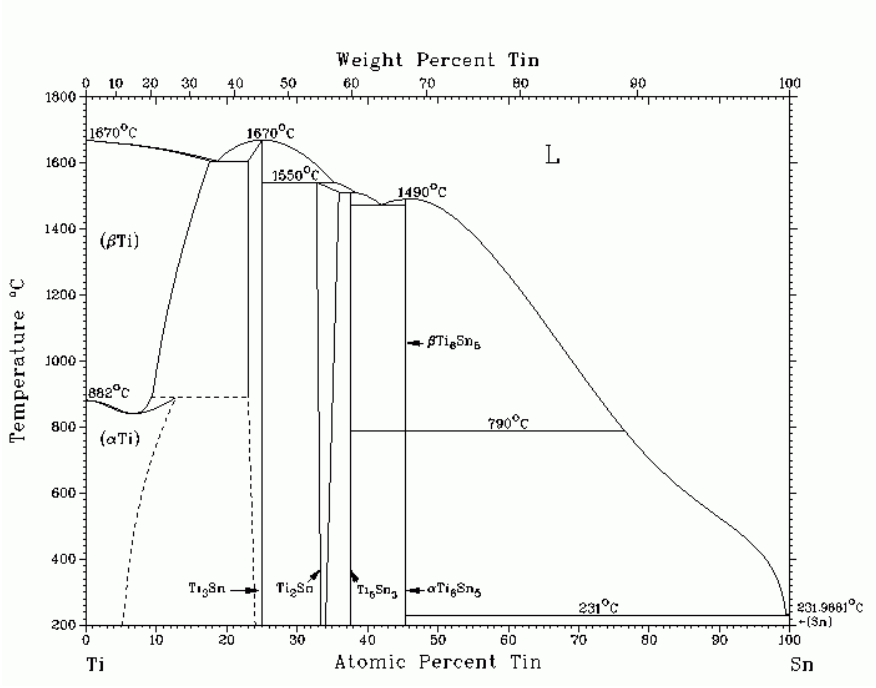

Fig 2.3: Ti-Sn phase diagram [35]

The binary Ti–Sn alloys (Fig 2.3) was developed due to their favourable mechanical properties. It is observed from the phase diagram of Ti-Sn system at higher content of Sn in Ti leads to formation of various intermetallic (Ti_3Sn, Ti_2Sn, Ti_6Sn_3 and Ti_6Sn_5) which makes the alloy more brittle while processing. Especially, in dental applications, elements like Al, V and Ni addition in Ti will be harmful due to their toxicity. In such instances, the addition of Sn can be considered a safe choice as an alloying element with Ti. It has been evaluated as non-toxic and capable of enhancing the alloy's strength [36].

β alloys: These alloys possess a significant quantity of β stabilizers (>10%) to maintain the β phase. It is mentioned that two categories of β stabilizers exist namely isomorphous and eutectoid. Isomorphous stabilizers encompass elements like Mo, V, Ta, and Nb while eutectoid stabilizers include Cr, Mn, Co, Fe, Cu, and Ni. The quantity of stabilizers present within an alloy determines whether the alloy assumes a metastable β or stable β state. Metastable β-Ti alloys are those containing adequate β stabilizers to inhibit the martensitic transformation process and retain the high-temperature BCC structure upon cooling or quenching to room temperature [31]. In theory, the incorporation of higher amounts of stabilizer elements would reduce the β transus temperature to below room temperature, resulting in the formation of a stable β alloy. But alloys with single phase β are not had commercial importance, hence the term ‘β alloys’ is commonly used to refer to the ‘metastable β alloys’. All of these alloys are classified as metastable β-Ti alloys since they are positioned within the region of α+β phase in

the phase diagram as shown in Fig 2.5. These alloys are heat-treatable, can be more readily cold-formed into sheets compared to other alloys [37]. The alloy selected for this study, Ti-15V-3Al-3Cr-3Sn, is a metastable β alloy.

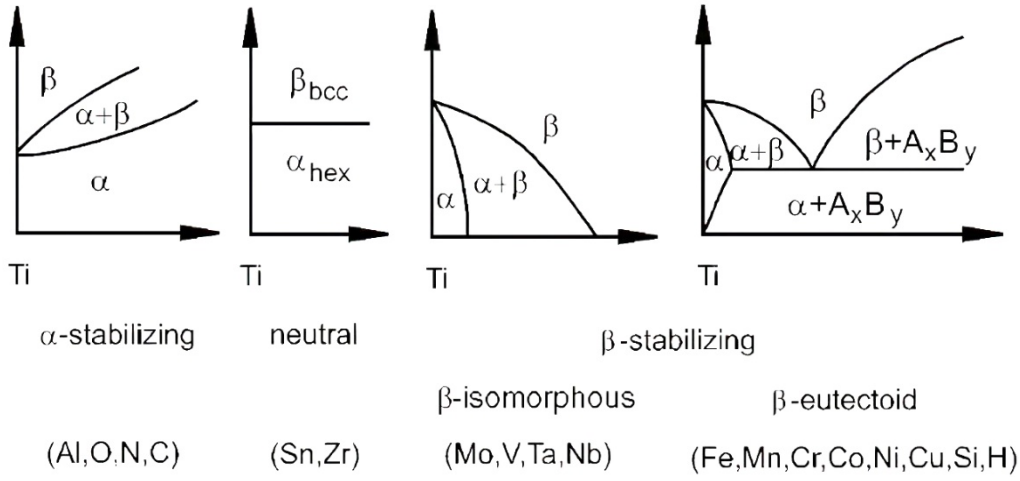

Fig 2.4: Alloying elements in Titanium [31]

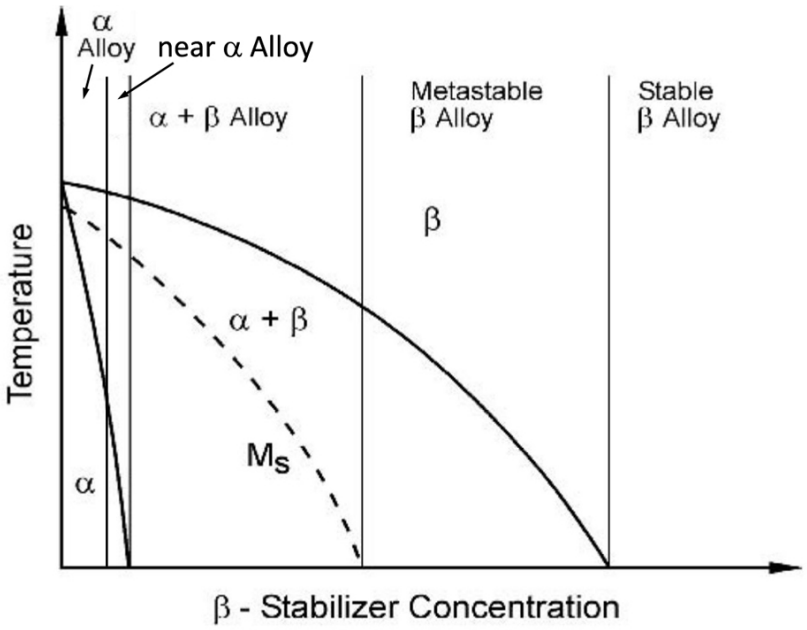

Fig 2.5: β isomorphous phase diagram showing the different categories of alloys [31].

2.3 Phase Transformations:

The metallurgical phases found in titanium play a crucial role in determining the properties of the material. These phases can be intentionally modified through heat treatment.

Therefore, to enhance the properties of Ti alloys, it is vital to gain control over the distribution, morphology and size of these phases.

In Ti alloys, the phases can be broadly classified into three categories: equilibrium phases, metastable phases, and intermediate phases. The equilibrium phases include α and β phases, while the metastable phases encompass α' and metastable β phases and intermediate phases include ω, and β' phases as shown in the Fig 2.6. The stability of these phases is closely linked to factors such as the alloying elements, rate of heating/cooling, as well as the temperature and duration of the heat treatment [5].

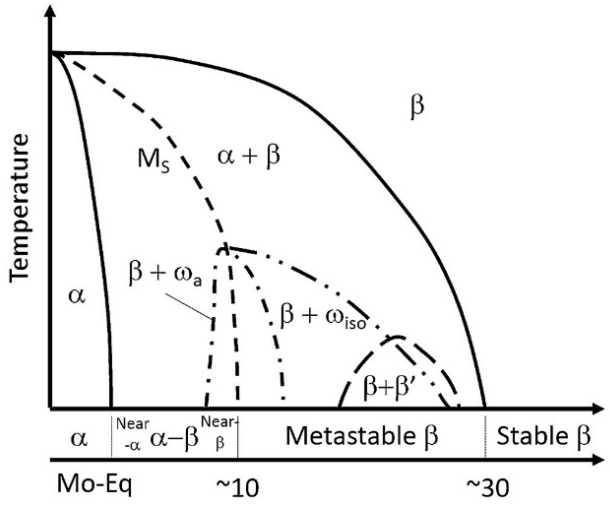

Fig 2.6: Pseudo binary Ti-beta isomorphous phase diagram [5].

Some common phase transformations in titanium alloys include:

2.3.1 β to α diffusional transformation:

The BCC β phase in titanium alloys can undergo two types of transformations, depending on the cooling rate and composition. It can either transform into the HCP α phase through nucleation and growth or adopt a martensitic transformation during the cooling. Nucleation and growth occur when the β phase is slowly cooled from the β phase region into the α+β phase region, resulting in the formation of a lamellar structure. As the cooling continues, a diffusional transformation takes place, where α phase nucleate and grow in within β grains as parallel plates (Fig 2.7), effectively separating the prior β matrix into layers. This combination of plates is referred to as an α-lamellar colonies which was displayed in Fig 2.7. These α colonies continue to grow until they encounter other colonies with different orientations. As the cooling rate rises, both the dimensions of α colonies and the thickness of individual α plates decrease [38].

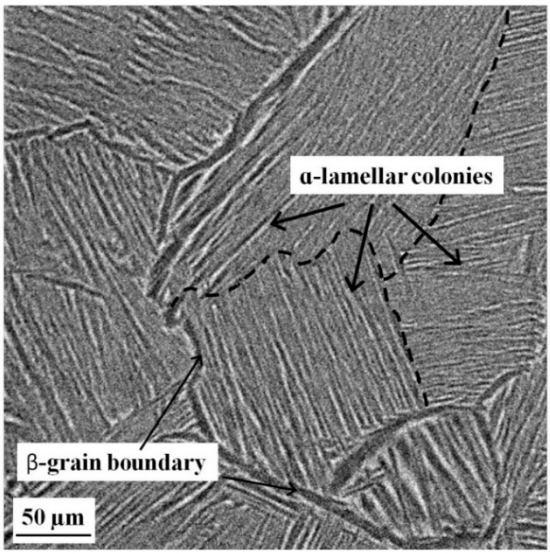

Fig 2.7: Example of microstructure of fully lamellar titanium alloys [39].

2.3.2 β to α' martensitic transformation:

The martensitic transformation encompasses the coordinated motion of atoms via a shear-type mechanism, leading to a diffusionless transition from the β phase to the α phase. Martensitic phases can be categorized based on their morphologies as “massive” martensite and "acicular" martensite, both possessing HCP crystal structures defined as alpha prime (α'). Massive martensite is characterized by a notably extensive, irregular region and is exclusive to pure titanium and its alloys featuring an exceptionally high M_s (martensitic start) temperature. As an example, the grade 2 CP-Ti shows the morphology of massive martensitic alpha phase in Fig 2.8 [40]. Acicular martensite consists of α laths and is found in α-β alloys. This transformation occurs when the alloy subjected to air cooling from β phase results in acicular α (Fig 2.9b). However, rapid cooling, like quenching in water from this temperature, leads to the creation of an α' (martensite) matrix (Fig 2.9c). If the cooling takes place from below the β transus temperature, where the alloy exhibits an primary α + β phase, different phase constituents can be observed at room temperature. Air-cooled alloy shows a combination of primary α grains in a matrix of transformed β, which includes acicular α (Fig 2.9d). A rapid cooling rate results in equiaxed primary α with in an α' matrix (Fig 2.9e) [38].

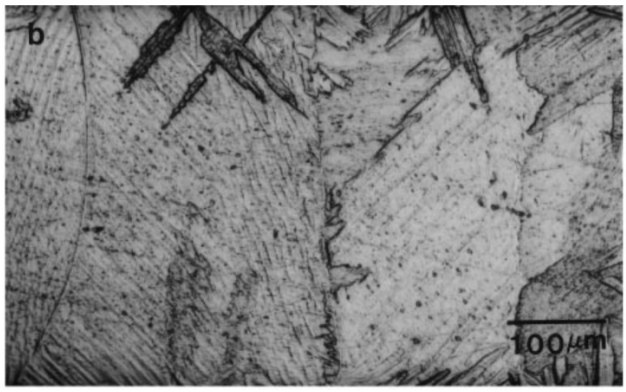

Fig 2.8: Optical micrograph of a grade 2 CP-Ti cooled from β phase field [40]

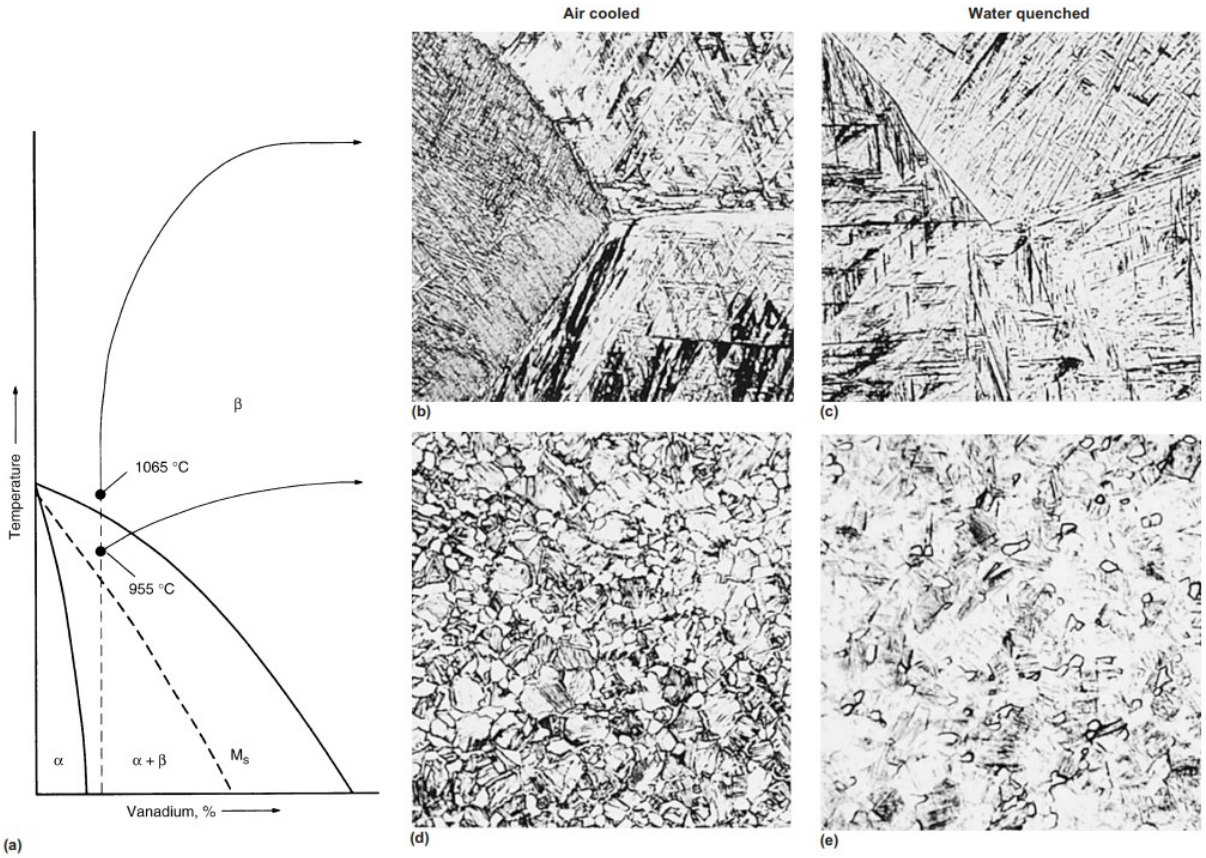

Fig 2.9: Pseudo phase diagram, along with microstructures of an annealed α-β alloy (Ti-6Al-4V), subjected to cooling from various regions within the phase field (a) the diagram, annotated with the Ti-6Al-4V composition. (b) Acicular α structures with prior β grain boundaries. (c) Martensitic α' matrix with β regions (dark) and prior β grain boundaries. (d) Grains composed of primary α (light) within a matrix of transformed β, featuring acicular α structures. (e) Equiaxed primary α structures within an α' (martensite) matrix.[41].

2.3.3 β to ω transformation:

In specific metastable β-Ti alloys, a metastable product called the omega-phase (ω) can coexist. Also, these alloys do not undergo martensitic transformation. As indicated in the pseudo phase diagram (Fig 2.6), the M_s temperature is below the room temperature for these alloys. Further, the ω-phase can form under three conditions, such as rapid cooling, aging, and room temperature deformation.

- The omega phase that emerges during rapid cooling is denoted as "athermal omega" (ω_a). This particular ω phase has been proposed to serve as a precursor to the martensitic transformation. The ω_a phase displays a trigonal symmetry structure and is more prone to develop in β-alloys with low solute content when subjected to rapid cooling. Nonetheless, it's not assured to manifest in all instances of rapid cooling, as the emergence of the hexagonal α' phase may take precedence in certain rapidly quenched samples. Nevertheless, subjecting these alloys to reheating above the M_s temperature can trigger the precipitation of the ω phase. [38].
- The ω-phase formed during ageing is referred to as isothermal omega (ω_{iso}). It typically forms by aging a retained β structure within a temperature range of 200 to 500 °C. The extent of ω_{iso} formation primarily depends on the composition of alloy and ageing time, although the kinetics of this transformation being relatively rapid. Prolonged aging within the aging temperature range eventually leads to the formation of equilibrium alpha. This type of ω phase has been suggested to act as a precursor for the nucleation site of α-phase [38]. The morphologies of ω_{iso} precipitates in some alloys like Ti-16Mo and Ti-8Fe subjected to aging are showed in Fig 2.10 [31].

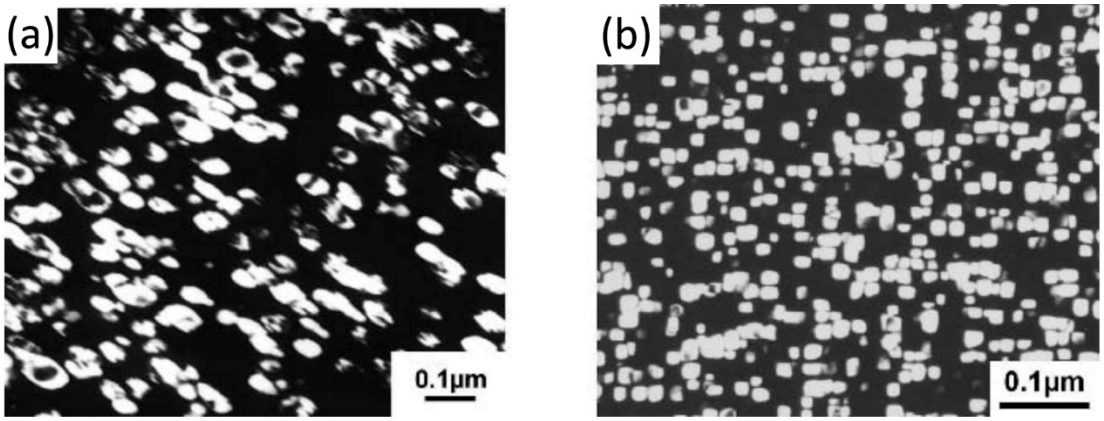

Fig 2.10: Dark field micrographs reveal (a) ellipsoidal ω precipitates in an aged Ti-16Mo alloy and (b) cuboidal precipitates in an aged Ti-8Fe alloy. [31].

- In the last case, the formation of ω-phase in β-Ti alloys is strongly influenced by the presence of impurities such as O or N that initiate pressure required for deformation-

induced ω phase formation (Fig 2.11). Under certain conditions, such as deformation during a room temperature tensile test, leads to the formation of ω-phase particles [42].

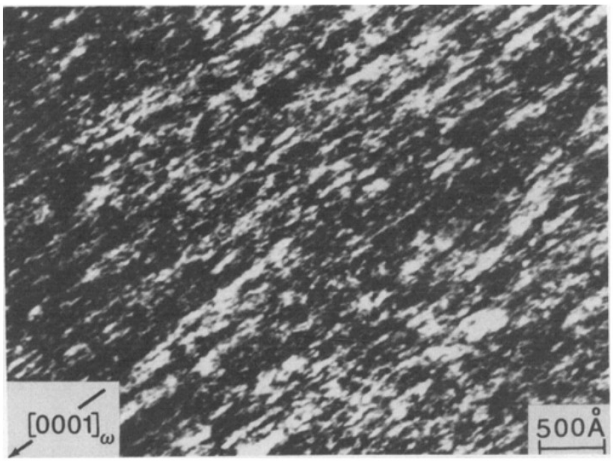

Fig 2.11: Dark field image from the stress-induced ω plate formed in Ti-V alloy system [43].

2.3.4 β to β' transformation:

When there is a higher concentration of β stabilizing elements (solute rich alloys) in a material, a phase separation occurs, resulting in the formation of $\beta \rightarrow \beta$ (solute rich) $+ \beta'$ (solute lean) phases. These metastable phases act as sites for heterogeneous nucleation of the equilibrium hcp α-phase. Both of these phases have BCC crystal structure but possess different lattice parameters. The formation of ω and β' phases is coherent and sheared during deformation. However, the presence of such precipitations is typically undesirable due to the emergence of localized slip bands. These bands can lead to early crack nucleation and reduced ductility. To mitigate these issues, aging and step aging treatments are commonly employed. These treatments serve to precipitate the α phase while using ω and β' as nucleation sites for controlled and improved material properties [38].

2.4 Effect of alloying elements:

The presence of alloying elements significantly influences the characteristics and performance of Ti alloys. Ti itself is a strong and lightweight metal, but its properties can be further improved by adding specific elements to the alloy. Some common alloying elements used in titanium alloys include Aluminium, Vanadium, Molybdenum, chromium, and others. Some of strengthening effects of alloying elements in titanium as follows:

Aluminium (Al): Addition of Al to Ti increases the solid solution strengthening of Ti alloys, especially at elevated temperatures. Al also enhances corrosion resistance and improves weldability. It substantially enhances the strength of titanium, and its ductility remains excellent up to 8% Al. However, an excessive amount of Ti_3Al can lead to embrittlement. Furthermore, when Al is combined with neutral elements like tin and zirconium, they can also cause embrittlement or reduce ductility, especially after exposure to creep conditions [44].

Vanadium (V): From a metallurgical perspective, V plays a key role as the primary stabilizer of the beta phase and acts as a solid-solution strengthened alongside Chromium (Cr). Although V improves the strength and hardenability of Ti alloys, its usage will be limited in the alloy formulation due to its negative impact on oxidation resistance [44].

Molybdenum (Mo): The alloys containing 5 to 7% Al in combination with 1 to 4% V or Mo (or both) exhibit lower sensitivity to atmospheric gases. Additionally, Ti is alloyed with elements like Pelladium (Pd), Ruthenium (Ru), Nickel (Ni), along with Mo to significantly enhance corrosion resistance, especially in slightly reducing environments where the formation of a protective oxide film on the metal surface might be hindered. β-Ti alloys, particularly those containing Mo, demonstrate remarkable immunity to stress-corrosion cracking when exposed to seawater [44].

Chromium (Cr): Incorporating Cr into Ti alloys regulates the alloy's anodic behaviour and enhances titanium's propensity to undergo passivation. Also, introduction of a small amount of Cr, typically around 2 to 3%, into certain Ti alloys contributes to increased ductility. Alloys containing the ternary Laves phase $Ti(Cr,Al)_2$ exhibit exceptional oxidation resistance. The interaction between Cr and Al does not promote the stabilization of the ω phase within the β phase, thereby mitigating alloy embrittlement [44].

Tin (Sn): Sn and Zr are regarded as neutral elements due to their minimal influence on the alpha or beta phase boundary. However, in terms of strength, they deviate from neutrality by predominantly reinforcing the alpha phase. The promotion of coherent precipitates serves as efficient impediments to dislocation glide and climb. In high-temperature titanium alloys, the Ti_3Al (α_2) particles volume fraction is elevated, largely attributed to the introduction of Sn facilitated by the formation of α_2. These coherent α_2 particles substantially augment the yield stress [44].

Silicon (Si): The incorporation of Si can significantly bolster the creep resistance of specific Ti alloys, particularly those closely related to α-phase titanium alloys. As Si precipitate as silicides along dislocations at elevated temperatures, effectively impeding dislocation climb, an important deformation mechanism in creep. However, Si not only improve the creep properties of near-alpha Ti alloys at elevated temperatures but also influence the microstructure. Because of the high Si content (0.45 wt.%) in the near- alpha alloy, minimizes the prior β grain size in lamellar microstructures significantly increases ductility [44].

Nickel (Ni): Ni alloyed with Ti to achieve a notable enhancement in corrosion resistance, especially in slight reducing environments where circumstances aren't favourable for the development of the required protective oxide film on the metal's surface. As Ni into Ti alters the potential at which hydrogen (H) undergoes reduction (hydrogen overvoltage). This shift in turn adjusts the corrosion current, leading to a decrease in the extent of corrosion attack [44].

2.5 Processing and microstructure:

2.5.1 Alpha Ti alloys:

Generally, commercial pure (CP) titanium grades categorized as α titanium alloys. Within this classification, the microstructure primarily consists of the α phase, accompanied by a minor volume fraction of the β phase. These alloys exhibit minimal alloying additions that remain unresponsive to heat treatment. However, thermomechanical processing is employed on these alloys to regulate grain size and crystallographic texture, although it is not utilized to modify the phase constitution [31].

A common processing sequence for α alloys comprises a series of three operations: homogenization, deformation, and recrystallization, as illustrated in Figure 2.12. In contrast to most high-strength alloys, many α alloys exhibit the ability for extensive cold rolling. However, α alloys are rarely employed in the unrecrystallized state. This is due to the limited strength gain achieved through cold working of Ti, due to its low work hardening characteristics. Additionally, the cold-worked alloy experiences reduced ductility, which limits subsequent manufacturing possibilities for components. Consequently, the term 'processing' in the context of CP titanium generally encompasses recrystallization annealing following the final rolling stage. Following processing, the microstructure of α alloys

predominantly comprises recrystallized α grains along with dispersed β phase. The presence of the β phase can be attributed to the inherent presence of a small quantity of iron (Fe) in all grades of CP titanium. Because of its constrained solubility within the α phase, iron (Fe) undergoes segregation to create the β phase, during the solidification. This β phase maintains its stability even at room temperature [31].

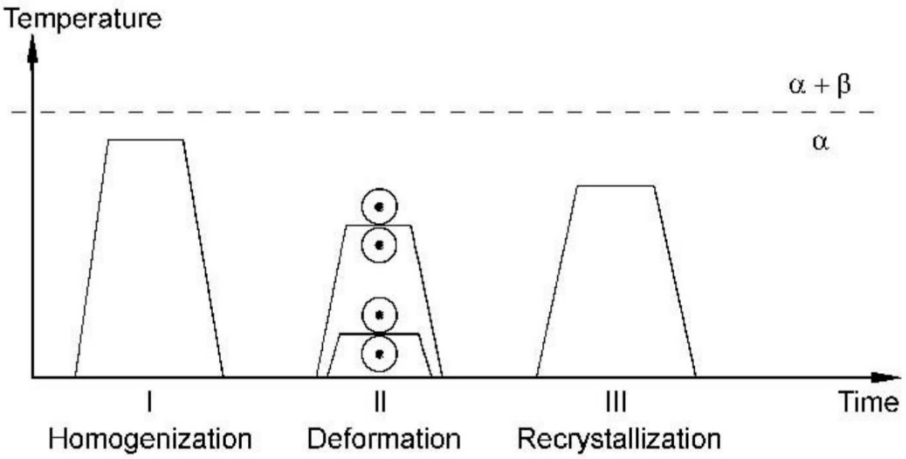

Fig 2.12: Schematic of the processing route for CP-Ti and α-phase Ti alloys [31].

2.5.2 Alpha-beta Ti alloys:

The typical processing route in α+β alloys leads to the formation of lamellar microstructures, which can be easily attained through an annealing heat treatment within the β-phase region, known as β recrystallization. This microstructure is often referred to as the "β-annealed" structure due to this process. In the schematic representation of the complete processing sequence (Fig 2.13), this recrystallization step within the β phase region is denoted as step III. The deformation step (Step II) may encompass either rolling or forging, occurring either within the (α+β) phase region or the β-phase region. In industrial applications, initial deformation typically occurs within the β phase region due to its lower flow stress, followed by subsequent deformation within the (α+β) phase region to prevent excessive β grain size. Likewise, during step III, it is typically advisable to keep the recrystallization temperature within a range of approximately 30-50°C above the β transus to efficiently manage the size of β grains. Consequently, fully lamellar microstructure of α and β phase exists. However, during step III, the rate of cooling from the β phase region emerges as the crucial determinant within the processing sequence. This cooling rate governs the dimensions and configurations of α lamellae (α plates), the size of α colonies, and the thickness of α layers at the boundaries of β grains [31].

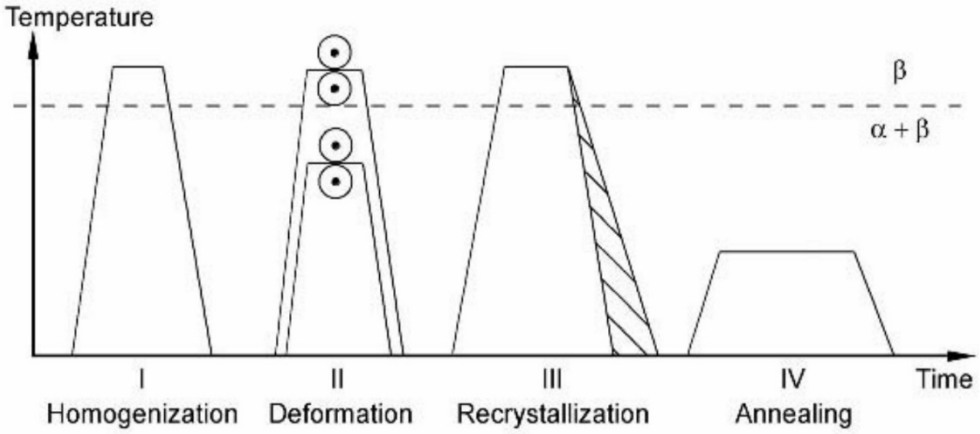

Fig 2.13: Schematic of processing pathway for achieving lamellar microstructures of α+β Ti alloys [31].

For example, the microstructures observed at lower and higher cooling rates of Ti-6242 alloy have been provided here. When the alloy is subjected to forced air cooling with an intermediate cooling rate of 1°C/min and 100°C/min results in lamellar microstructure with a reduction in α colonies as cooling rate increases (as observed in Figs. 2.14a and 2.14b). If the cooling rate further increase to critical cooling rate this transition transforms from a colony microstructure to a martensitic structure, which is inherently influenced by the alloy composition. However, for the most prevalent α+β Ti-6242 alloy, this transformation takes place at cooling rates exceeding 1000°C/min. Consequently, martensitic microstructures are infrequently encountered in structural components composed of α+β alloys. However, these martensitic structures are not of commercial significance, hence this can be transformed into fine α+β lamellar microstructures through annealing (step IV in Fig. 2.13) [31].

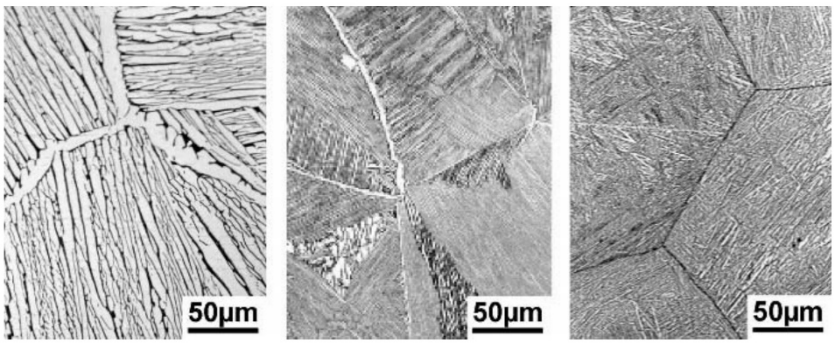

Fig 2.14: Influence of cooling rate on Ti-6242 alloy from β phase region on lamellar microstructures, (a) 1°C/min (b) 100 °C/min (c) 8000 °C/min [31]

2.5.3 Beta Ti alloys:

Unlike α+β alloys, β alloys do not experience martensitic transformation when rapidly cooled to room temperature, leading in the persistence of a metastable β phase. The α phase can then precipitate from this metastable β phase in the form of extremely fine, non-deformable particles (platelets) with a substantial volume fraction. As a result, the defining feature of β-Ti alloys is their capacity for achieving significantly elevated levels of yield stress compared to α+β Ti alloys. Another benefit of β alloys is their capacity for processing at reduced temperatures compared to α+β alloys. In fact, specific heavily stabilized β-Ti alloys can even demonstrate cold deformability. [31].

The fundamental processing pathway for obtaining β-annealed microstructures is depicted in Figure 2.15. Remarkably, the β-annealed microstructure is achieved through a straightforward sequence: recrystallization within the β phase region (Step III), followed by aging within the (α+β) phase region (Step IV), which induces the precipitation of fine α platelets. But in case of heavily stabilized β-Ti alloys, achieving a uniform distribution of α precipitates through single-stage aging process is sometimes quite challenging. This occurs because the formation of essential precursors (β' or ω) is too slow during the heating process to reach the aging temperature. As a result, the processing sequence includes this two-stage aging method. In the preliminary aging phase (Step IVa), a uniform distribution of exceptionally fine α platelets is formed. These fine platelets of α phase then undergo growth or coarsening to the desired degree during the subsequent conventional aging process. [31].

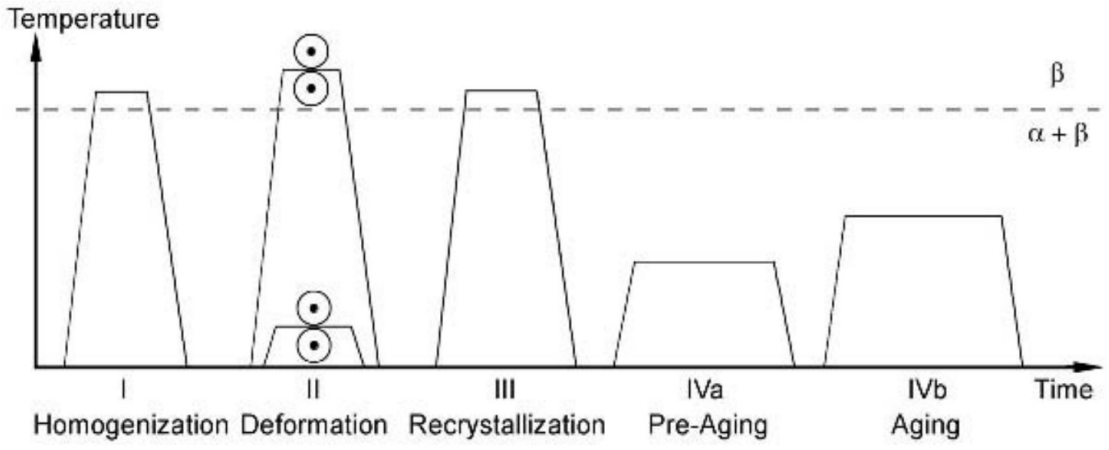

Fig 2.15: Schematic representation of the processing pathway for achieving β-annealed microstructures in heavily stabilized β-Ti alloys, including a pre-aging step [31].

Typically, metastable β-Ti alloys find application in structural uses, leveraging their blend of high specific strengths, robust fatigue resistance, excellent toughness, exceptional corrosion

resistance, low elastic modulus and formability. Additionally, they exhibit remarkable biocompatibility, rendering them suitable for use in medical implants. Within this alloy category, there exists a substantial concentration of beta-stabilizing elements, enabling the preservation of nearly 100% metastable β-phase at room temperature following rapid cooling from the single-phase region. These characteristics render metastable β-Ti alloys an appealing option for advanced engineering applications, notwithstanding their relatively high cost. An example is the metastable alloy Ti-3Al-8V-6Cr-4Mo-4Zr (wt. %), often referred to as Beta C, which is employed in aircraft springs and fasteners. Additionally, another metastable alloy, Ti-29Nb-13Ta-4.6Zr (wt. %), has been developed specifically for use in medical implants [45].

To evaluate the persistence of the β-phase in a Ti alloy with a specific composition, an established and valuable parameter is the Molybdenum Equivalency (MoE). This parameter provides a comprehensive evaluation of how the beta stabilizers, alpha stabilizers and neutral elements within the Titanium alloy influence the stability of the beta phase. MoE employs Molybdenum as a reference element and standardizes other components to their equivalent Molybdenum values. The equation is defined as follows [46]:

$$MoE = Mo + 0.67V + 0.44W + 0.28Nb + 0.22Ta + 2.9Fe + 1.6Cr - 1.0Al \quad (2.1)$$ [46]

Therefore, MoE serves as a convenient metric for ranking the beta phase stability of several commercially available Ti alloys. Table 2.1 presents the MoE values and major application of some commercially significant beta Ti alloys. Additionally, Fig 2.16 graphically represents the MoE values from Table 2.1, showcasing their ranking order [45].

Table 2.1: The MoE and beta transus temperatures of few commercially significant beta Ti alloys. The alloy compositions are presented in wt. % [45].

Alloy	Name	Application	Type	MoE	Beta Transus (°C)
Ti-13Nb-13Zr	-	Biomedical	Beta-rich	1.4	735
Ti-20Nb-10Zr-5Ta	TNZT	Biomedical	Near-Beta	5.0	-
Ti-5Al-5Mo-5V-3Cr	Ti-5553	Aircraft	Near-Beta	8.2	855–870
Ti-11.5Mo-6Zr-4.5Sn	TMA	Biomedical	Near-Beta	9.0	-
Ti-10V-2Fe-3Al	Ti-10-2-3	Aircraft	Near-Beta	9.5	790–805
Ti-35Nb-5Ta-7Zr	-	Biomedical	Near-Beta	9.7	-
Ti-29Nb-13Ta-4.6Zr	-	Biomedical	Metastable	10.2	-
Ti-15V-3Cr-3Al-3Sn	-	Aircraft	Metastable	10.9	750–770
Ti-15Mo-3Al-3Nb-0.2Si	Beta 21S	Aircraft	Metastable	12.8	795–810
Ti-15Mo	-	Model Binary	Metastable	15.0	-
Ti-3Al-8V-6Cr-4Mo-4Zr	Beta C	Aircraft/Oilfields	Metastable	16.0	715–740
Ti-12Mo-6Zr-2Fe	-	Biomedical	Metastable	16.8	-
Ti-13V-11Cr-3Al	B120 VCA	Aircraft	Metastable	23.0	650
Ti-30Mo	-	Model Binary	Stable	30.0	-
Ti-40Mo	-	Model Binary	Stable	40.0	-
Ti-35V-15Cr	Alloy C	Aircraft	Stable	47.5	unknown

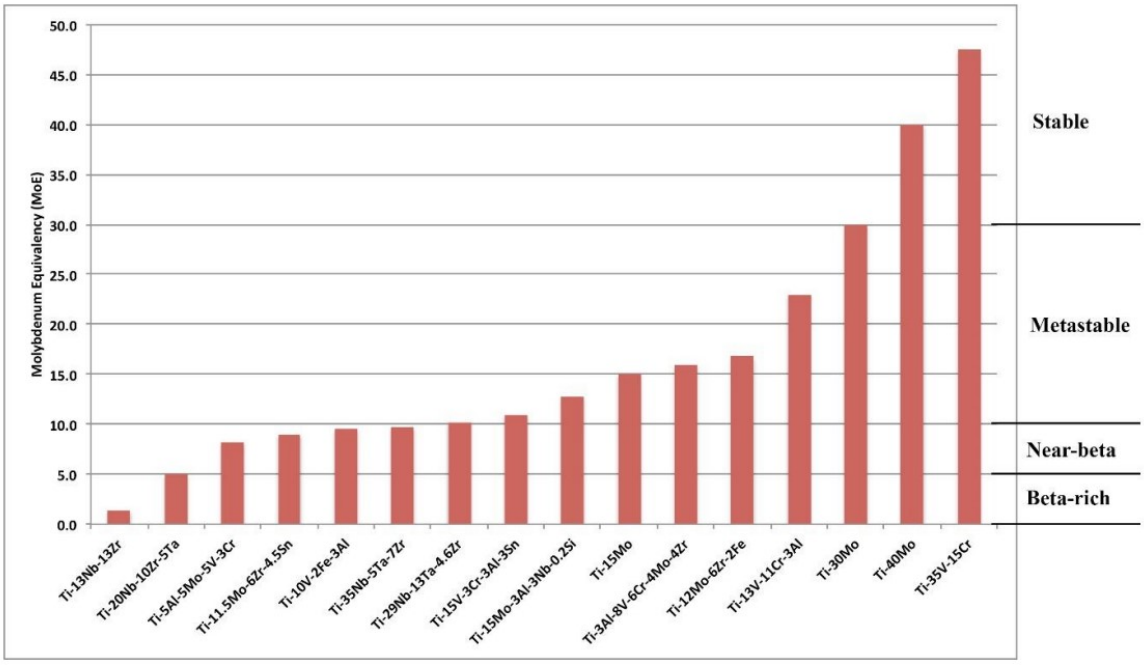

Fig 2.16: A graphical representation of MoE of model binary and commercially significant β Ti alloys as outlined in Table 2.1. Alloys with MoE ranges from 0 to 5 are categorized as beta-rich, those with 5 to 10 are considered as near-beta, alloys with 10 to 30 are classified as metastable, and alloys with MoE exceeding 30 are designated as stable [45].

2.6 Ti-15V-3Al-3Cr-3Sn (Ti-15-3) Alloy:

The Ti alloy Ti-15-3, categorized as a metastable β-Ti alloy was developed during the 1980s. Ti-15-3 is composed of Ti with 15 wt.% V, 3 wt.% Cr, 3 wt.% Al, and 3 wt.% Sn. It possesses

heat treatability, excellent hardenability, as well as proficiency in both hot and cold processing. This alloy finds widespread use across industries like aerospace, automotive, and even biomedical applications, owing to its advantageous attributes such as excellent cold-formability and high specific strength. The cold-formability of Ti-15-3 surpasses that of α-β and α-titanium alloys. Consequently, Ti-15-3 alloy undergoes heat treatment to promote precipitation of α phase or intermetallic compounds contributing to enhanced yield strength and fracture toughness [47].

2.7 Welding processes for Ti-alloys:

Welding is frequently used as a fabrication technique in the manufacturing of components for aircraft and military applications, and several fusion welding processes such as EBW, GTAW, gas metal arc welding (GMAW), LBW, plasma arc welding (PAW), are commonly used. The Ti alloys are much more susceptible to contamination by the gaseous elements such O, H, and N above 500˚C, which diminish the ductility of the weld and resistance to corrosion. Therefore, the main conditions to be fulfilled for welding of titanium alloys are protecting the weld zone from contamination by providing shielding gases. Conventionally, GTAW, EBW and LBW processes have been used to weld Ti alloys. In GTAW and LBW processes, the weld zone can be protected from atmospheric gases by localized shielding gases. Regarding the EBW process, the complete component is sealed under the vacuum environment, inherently providing better protection from the environment [9]. Hence, the present study is carried out on the welding of Ti-15-3 by EBW and GTAW processes.

2.7.1 Electron Beam Welding:

EBW utilizes the kinetic energy of electrons as a heat source for the fusion of metals during joining processes. These electrons are produced by heating a negatively charged filament (cathode) to a temperature range conducive to thermionic emission. As these electrons accelerate due to the electric field established between the negatively charged bias electrode, located just beneath the cathode, and the anode, they traverse through the aperture in the anode, resulting in the formation of an EB (as depicted in Figure 2.17). This EB can be concentrated onto the workpiece through the aid of electromagnetic focusing coils. Under vacuum conditions, the electron beam can be concentrated and directed to strike the metal surface at

velocities reaching up to 70% of the speed of light. Approximately 95% of the kinetic energy of these electrons gets converted into heat [48].

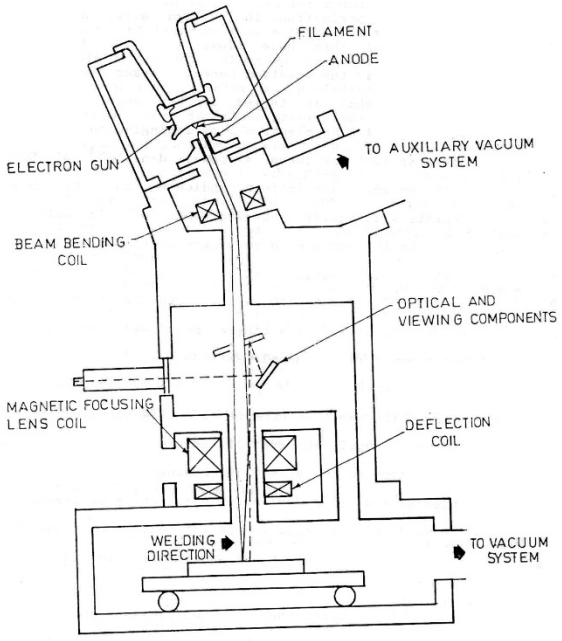

Fig 2.17: Schematic of EBW process [48].

The EB is capable of being focused to diameters ranging from 0.3 to 0.8 mm, yielding an ensuing power density that can reach levels as high as 1010 Wm^{-2}. Consequently, the combination of high power density and the inherently limited penetration of the electrons leads to nearly instantaneous, localized melting and vaporization of the material. The beam's heightened intensity effectively vaporizes any material, generating a vapor hole or keyhole that extends deeply into the workpiece. As the beam progresses along the joint, the molten metal from the leading section of the keyhole flows around its edges, subsequently solidifying at the rear to form the weld metal [49].

The basic components of an EBW machine encompass the power supply and control system, the EB gun, a focusing mechanism integrated onto a vacuum chamber, and an internal fixture or turning device designed for the alignment or movement of the weld joint in correlation with the electron beam. Electron beam processing can be conducted under vacuum or atmospheric conditions, employing stationary or mobile guns, and utilizing high (60 to 150 kV) or low (30 to 60 kV) beam voltages, among other variations. The extent of vacuum within which the welding occurs dictates the process mode and subsequently dictates the specific equipment needed

(a) EB welding under high vacuum conditions (10^{-4} torr or less)

(b) EB welding under medium vacuum conditions (25 to 10^{-4} torr)

(c) EB welding without the use of vacuum.

Reactive and refractory metals necessitate welding within a high vacuum environment to prevent atmospheric contamination. This requirement is particularly pertinent for joints involving materials like Ti or its alloys. Furthermore, the penetration capability diminishes as vacuum levels decrease. Typically, the utmost weld quality is attained when operating under high vacuum conditions, although the other two modes can be suitably employed in specific scenarios[48].

A paramount advantage of EBW lies in its exceptional penetration potential, attributed to its high power output. Consequently, EBW can produce clean and high-quality welds compared to other fusion welding processes. The high-energy power beam source in EBW can readily generate single-pass full penetration welds for thicker sections, which cannot be accomplished by conventional welding techniques. Further, a narrow weld can be produced by the EBW due to low heat input, which decreases the width of HAZ, thereby reducing the residual stresses and distortion of the workpiece. As a result, distortion and shrinkage are minimal. Additional merits encompass the capable to weld refractory and reactive metals in an environment free of contaminants, as well as the ability to join dissimilar metals [50].

2.7.2 Gas tungsten arc welding:

The GTAW process is a fusion welding technique that employs a non-consumable tungsten electrode for metal joining. This process relies on an electric arc sustained between the workpiece and the tungsten electrode, which conducts the electrical current. A shielding gas provides an inert atmosphere which will protect the workpiece and electrode from atmospheric contamination. The common shielding gases used are argon or helium and a mixture of both depends on the application and weld material thickness. As the ionization potential of argon is lower than that of helium it is mostly used in thin materials as due to less penetration of arc. The mixture of helium and argon (30% - 80% He) will give good penetration and speed. Generally, GTAW is capable of joining the materials with and without fillers. If welding is done without fillers are known to be autogenous welds. The additional advantage of the GTAW process can operate in all welding positions produces smooth and sound welds with less spatters. There have been other important parameters that can influence the welding arc are current, voltage, heat input, and weld speed [6]. Several GTAW variations have been reported to achieve enhanced penetration, lower heat input,, and reduced distortion. These include narrow gap welding, the use of flux-cored filler wire, submerged arc welding, keyhole mode

GTAW, and active flux TIG welding.. While some research on Keyhole mode GTAW and active flux TIG process of Titanium alloys have been observed good penetration in the weld pool [2]. For a visual representation of the GTAW process, refer to Fig 2.18.

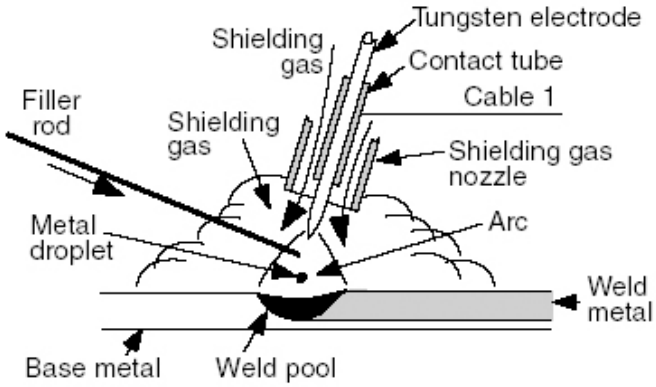

Fig 2.18 Schematic of GTAW process [51]

In the realm of GTAW, the electrical currents employed can either be alternating current (AC) or direct current (DC). These currents can be applied in a continuous manner or be pulsed intermittently. In the case of pulsed current GTAW, the welding current undergoes cycles of transitioning from high to low levels at specific frequencies. Pulsed current has been utilized to achieve grain refinement within the weld zone. This refinement has not been observed in continuous current welding, which has shown larger grains characterized by columnar grain structure [52].

2.7.3 Pulsed current technique in GTA welding:

The pulsed GTAW (P-GTAW) is a variation of conventional GTAW (C-GTAW). The pulsing involves the periodic modulation of welding current from a higher level (peak current) and a lower level (background current) at a regular frequency. At peak current, more heat is generated and used for melting and good penetration in metal, while in the background current is set for maintaining the stable arc and cooling will take place. As illustrated in Figure 2.19, P-GTAW entails the periodic modulation of welding current, oscillating between high and low levels at a consistent frequency. The high level is said to be peak current (I_p) whereas the low level is said to be background current (I_b). The period between the point at which the current begin to rise and the point at which the current starts to lower is known as Peak Time (T_p) while background current (T_b) is the time span at the low current level of pulse [53].

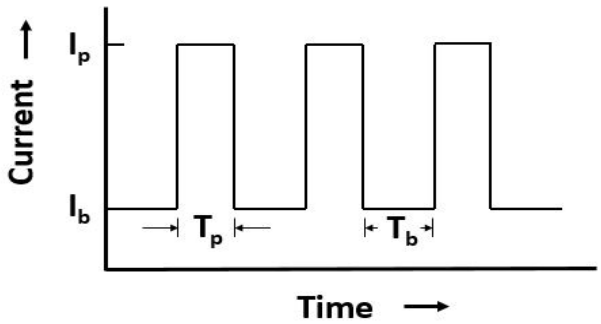

Fig 2.19: Schematic representation of current-time diagram of pulsed GTAW.

At peak, current good penetration of arc and bead counter and background current maintained for stable arc and cleaning. The other important process variable of pulsed GTAW is the frequency of cycle which is equal to the inverse of ($T_p + T_b$) [54]. In addition to pulse frequency, the parameters which can influence the heat input (J/mm) are pulse amplitude and waveform. Leithner et al. [53] has examined the higher pulse amplitude and pulse waveform with a large percentage of time at a high current level will give deeper penetration and greater depth to width ratio than in conventional GTAW process at same heat input. Beaker et al. [52] has investigated pulsed GTA welding parameters of two titanium alloys namely Ti-8Al-1Mo-1V and Ti-11.5Mo-6Zr-4.5Sn reported that the penetration and heat input can be strongly influenced by the fraction of time at peak current "θ_p" which is equal to $T_p/ (T_p+ T_b)$. The study deduced at the low value of the fraction of time at peak current results in complete penetration of weld sheets, improved bead contour and reduced heat input. Another useful combination involves spot spacing which is a function of travel speed and total pulsing time [55]. It was observed that high-frequency pulsing will lead to an increase in weld depth. Current pulsing in GTAW also has a greater influence on the electromagnetic force which will improve weld pool geometry [56].

2.8 Welding metallurgy of Ti alloys:

In any joining process, the metallurgy of joining plays a prominent role in understanding of the dynamic thermal conditions, microstructural changes, and diffusion mechanisms during melting and solidification of FZ and solid-state transformations in HAZ. These characteristics in turn effect the mechanical properties of the welds. Even fillers' composition, and torch travel speed can also vary the microstructure and mechanical characteristics of the weld. So, it is essential to have an idea about the weld microstructure of titanium alloys [57].

Commonly in fusion welding, the solidification will start at fusion boundary on existing grains of substrate metal and this type of growth is known as epitaxial grain growth. The post weld microstructure of welded joints mostly depends on the initial microstructure of BM and thermal cycle during the welding process [58]. Xiong et al. [59] has reported the microstructure of FZ in GTAW of near alpha titanium alloy Ti-6Al-3Nb-2Zr-1Mo. The weld microstructure was found to be composed of widmanstatten α+β, acicular α and massive α and. As in the welding of alpha titanium alloys, in near alpha alloys the low temperature α phase transform to the high-temperature β phase due to a rise in temperature. During post solidification cooling to low temperatures, the high-temperature β phases transform to acicular α phases due to fast cooling. It was shown that the grains in HAZ region are finer than that of FZ, but the region of HAZ which is near to FZ consists of courser acicular α and less fraction of primary α whereas the HAZ region near to base metal (away from FZ) showed higher fraction of primary α and fine acicular α. This variation in microstructure across HAZ and FZ is due to non-uniform thermal cycle at various points of the weldment. Babu et al. [60] reported that epitaxial growth of large prior β-grains from the substrate metal into weld FZ in GTAW of Ti-6Al-4V, an α+β Titanium alloy on solidification. It was found that on cooling, the β phase decompose to α phase by diffusional transformation or α′ phase via martensitic transformation (diffusion-less) or a mixture of both. Thereby FZ comprises of a mixture of α, α′ and retained β phases. It was also noted that M_s Temperature has a greater influence on the formation of α′. The content of β-stabilizers has greater influence on the M_s Temperature. Lower β-stabilizers shift the M_s Temperature above room temperature and results in the formation of α′. There has been grain coarsening in the HAZ region due to the extraction of heat from the fusion zone.

Similarly, Balachandar et al.[16] have examined the microstructure of the metastable β-Ti alloy Ti-15-3, which was welded using the GTAW process. Their findings reveal the formation of single-phase, coarse columnar β grains that initiate along the fusion line and extend towards the weld centreline. Due to the dissipation of heat from the solidifying FZ, there was grain coarsening near HAZ resulting in streaks of α-phase transformed from the transformed β-phase. In contrast, a fine grain structure was observed in far HAZ because of less heat transfer and thereby no sufficient time to grow. The dimensions and shape of the prior β grains depend on the weld energy input and weld pool geometry. There has been limited research on GTAW welding of beta titanium alloys done by various researchers. Baeslack III et al. [61] conducted an examination of the welded microstructure in several beta titanium alloys, including Beta-CTM (Ti-3Al-8V-6Cr-4Mo-4Zr), Beta-21S, and others. Their research findings indicate a

decrease in strength within the FZ and HAZ when compared to the BM. This reduction in strength can be attributed to the formation of coarse columnar β-grains throughout the FZ.

2.8.1 Beta grain size problem in Ti-15-3:

In the GTAW process depending on the thermal conditions and microstructural changes, the weld zone was divided into different zones as shown in Fig 2.20. The FZ experiences the temperatures above liquidus point and coarse columnar β grains form on solidification. A boundary line that separates the FZ with HAZ is known as a fusion line where the nucleation of β grains will grow towards the weld center. The maximum temperature in HAZ which was near to FZ is greater than beta transus but below liquids temperature. Whereas the HAZ region away from FZ experience the temperature below beta trances but greater than the temperature required for microstructural changes. These variation in weld microstructure across the weldment is attributed due to the transformation kinetics [62].

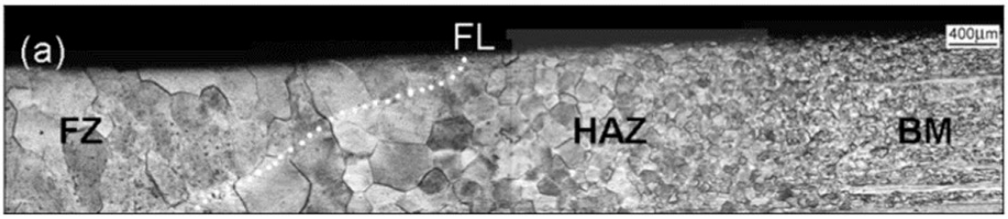

Fig 2.20: Micrograph of as-welded sample showing grain morphology from FZ to the BM of Ti-15-3 [16]

The β phase grainsize and morphology in the β Ti alloys weldments greatly influence the mechanical properties. In FZ the beta grains follow different solidification modes like planar, cellular, or dendritic growth depending on the degree of supercooling. It should be noted that higher the supercooling results in cellular or dendritic growth leads to finer grains in the fusion zone which improves the mechanical properties [63]. In some of the titanium welds, it was difficult to differentiate the FZ from the HAZ region due to similarity in courser beta grains. The studies found that the energy input can also influence the width of the grains in FZ. In fusion welding processes like GTAW, GMAW, etc. will develop higher input in the welds will leads to an increase in growth of grain in FZ [64].

From the studies of Mohandas et al. [65] identified a decline in mechanical properties, especially in ductility. This decrease can be attributed to the formation of coarser columnar β grains within the FZ. Furthermore, the presence of the alpha phase at lower temperatures was

observed to inhibit the growth of beta grains. Therefore, when employing the GTAW method, the use of pulsing techniques can be advantageous in reducing heat input, thus facilitating the maintenance of finer grains. The investigation of Poorganji et al. [66] on grain growth in a beta titanium alloy, specifically Ti-14Mo-3Nb-1.5Zr during arc melting, noted a refinement in grain size achieved by introducing a small quantity of yttria (Y_2O_3). This refinement occurred as Y2O3 particles effectively pinned themselves at grain boundaries.

2.8.2 Phase transformation on cooling:

In solidification of fusion zone in welds, the formation of phases depends on the cooling rate and solute elements. Even the solid-state transformation in the HAZ region will also depend on the cooling conditions. A useful method to study those transformations in welds is a continuous cooling transformation diagram (CCT) and a time-temperature transformation diagram (TTT). An experimental TTT diagram of beta titanium alloys has been published [5]. In the majority of metastable beta titanium alloys, the elevated levels of beta stabilizers effectively inhibit the martensitic transformation of the α phase because the M_s temperature falls below room temperature. Hence, when fastly cooled from temperatures above the beta transus temperature, the retention of a metastable β phase at room temperature can be associated with the GTAW process used for welding metastable β-Ti alloys. Moreover, a metastable ω phase is observed as finely dispersed particles within the β phase. However, there are two types of ω formation in metastable beta titanium alloys below ω solvus temperature. Athermal ω forms by diffusionless transformation on fast cooling, while isothermal ω transformation is because of the isothermal aging of the quenched metastable beta. The study found that the presence of ω phase will act as a precursor for fine precipitation of α laths distributed in β matrix [67]. According to the β-isomorphous phase diagram of titanium alloys, the athermal ω phase is formed at a lower concentration of the β-stabilizing elements whereas the isothermal ω phase was formed at a higher concentration of the β-stabilizers [68]. But in some of the metastable beta titanium alloys because of high solute content, β to ω transformation can be suppressed due to rapid decrease in ω transformation temperature [69].

Ng et al. [70] has observed the beta transformation of two metastable β-Ti alloys Ti-10V-4Ni indicates by A1 and Ti-10V-6Cu indicated by A2 were shown in Fig 2.21. From TTT curves it is evident that the difference in transformation time of α and ω phases in both metastable β-Ti alloys as due to compositional variations. On the aging of these alloys found the formation of isothermal ω in the temperature range of 350˚C - 500˚C while in quenching athermal ω formation seen at low temperatures.

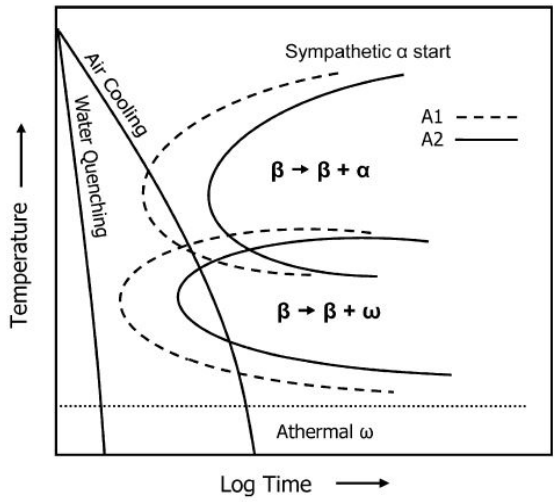

Fig 2.21: Schematic of TTT diagram of metastable beta Ti alloy Ti-10V-2Ni (A1) and Ti-10V-6Cu (A2) [70]

Angelier et al. [71] has investigated the phase transformation of Ti-5Al-2Sn-4Zr-4Mo-2Cr-1Fe (β CEZ) a near-β titanium alloy has calculated the fraction of phases on different cooling rates with the help of electrical resistivity measurement technique. As resistivity is proportional to a fraction which will indicate the fraction of transformed β in an alloy can be measured. The studies found that α precipitation occurs at grain boundary β and further develops into widmantstatten α. This widmantstatten α will grow in the intergranular region and form a basket weave microstructure. It was observed that generally at low cooling rates below 10˚C/s and temperature range of 525˚C - 840˚C will lead to precipitation of α phase. At high cooling rates above 10˚C, there is a formation of ω phase that can be examined through an electron microscope.

Thus the scheme of decomposition of the β phase into different phase morphologies depends on the rate of cooling and composition of the alloy are assist to understand the phase transformations in the welding of Ti alloys [72].

2.9 Influence of welding speed on microstructure:

As discussed earlier, the coarse columnar grains in FZ adversely affect the mechanical properties of these β-Ti welds. Hence, grain refinement in FZ from coarse columnar to equiaxed dendritic grains is necessary to improve the weld performance. The computed ratio G/R, where G corresponds to a temperature gradient and R is the growth rate during the solidification, is used to predict the transition from CET mode during weld solidification. It is well known that CET is favoured when R is higher and G is lower [73]. The common grain refinement techniques influencing the G/R ratio are welding parameters [74], beam oscillation technique [75], nucleating agents [76], arc pulsing [77], and other factors. Nevertheless, the welding speed stands as a pivotal welding parameter that exerts an impact on both the cooling rate (the product of G and R) and the heat input. At lower speeds, the cooling rate is low, and heat input is high; hence much time is available for coarsening of the grains. In contrast, at higher welding speeds, with lower heat input and higher cooling rate, a constitutional supercooling zone is developed ahead of the solid-liquid (S/L) interface due to a low G/R ratio resulting in the formation of finer grains [78].

For instance, Zhan et al. [79] investigated the effect of welding parameters, specifically welding speed and laser power, on the microstructural properties and mechanical characteristics of laser-welded Ti-6Al-2Zr-1Mo-1V (TA15) alloy. They reported that by increasing the welding speed, the welding heat input decreases and the grains grow fine and directional. Sattar et al. [74] used the Taguchi design experiment to identify appropriate welding parameters (welding speed, current, , and filler wire speed) for controlling the weld bead geometry of Ti-64 GTAW samples. Their findings showed that welding speed had the greatest impact on weld bead hardness (contributing 71.32%) and welding current (21.98%). Liu et al. [80] explored the effect of welding parameters (specifically welding speed and laser power) on the microstructural properties and mechanical characteristics of laser-welded Ti-64 alloy. The results revealed that Ti-64 similar joints had the highest strength but at expense of ductility among all the welding combinations tested with varying welding parameters.

2.10 Grain refinement mechanism of Ti alloys:

The mechanical properties in metastable β titanium alloys can be governed by the β grain size and precipitation of α phase in the beta matrix. Early investigations into the welding of β titanium alloys revealed that the reduced strength in the weld joint can be attributed to the development of coarse columnar β grains in the FZ [81]. Due to this generally metastable β-Ti alloys are subjected to PWHT to precipitate the fine dispersed phase of α in the β matrix to improve the mechanical behaviour. However PWHT will improve the strength and ductility

but could also results in grain coarsening of BM. Hence an alternative approach that can be used to keep away the heat treatment to reduce the production expenses and save time is by selection of suitable fillers that can prompt the nucleation and growth of α phase in β matrix and refinement of the β grains in FZ [82].

M.J. Bermingham et.al has been examined about the grain refinement mechanism in Titanium based alloys which are casted with Al and V. A slight reduction in the size of β-grains was noted as solute additions increased. This effect of solute on grain size can be quantified by the growth restriction factor (GRF), denoted as Q. [83]

$$Q = m(k\text{-}1)C_o \quad \text{---------- (2.2)} \quad [83]$$

Where m represents the liquidus line slope, k denotes the partition coefficient of solute ($k = C_s/C_l$; C_l and C_s correspond to the solute contents of the liquid and solid in equilibrium at the interface). C_o stands for the solute content of the alloy.

Based on the equation (2.2) above, it can be deduced that Q is associated with the initial rate of formation of the constitutional undercooled zone. Solutes with a higher GRF exhibit strong segregation ahead of the advancing interface, leading to the rapid accumulation of constitutional undercooling. As the constitutional undercooled zone develops more swiftly, it facilitates further nucleation ahead of the S/L interface, ultimately resulting in a reduction in grain size. As shown in Table 2.2 the elements which are having higher GRF are at bottom end and lower will be at the top most side [19].

Table 2.2: Calculated values of Q for various elements in Ti, which is equivalent to $m(k\text{-}1)C_o$ where the values indicated for 1wt% of solute [19].

Element	m_l	k	$m_l(k-1)^{**}$
Hf	−0.7	→1	→0
Al	−2.1	→1	→0
V	−4.7	→1	→0
Sn	−0.8	→1	→0
Zr	−2.4	0.86	0.3
Pb	−6.6	0.84	1.1
Cr	−8.1	0.81	1.5
Pd	−10.5	0.77	2.4
Pt	−8.4	0.70	2.5
Bi	−5.5	0.54	2.5
Nd	−3.9	0.19	3.2
La	−5.7	0.43	3.3
Fe	−18	0.79	3.8
Er	−5.0	0.19	4.1
Tb	−4.4	0.04	4.2
Ce	−5.4	0.14	4.6
Gd	−6.2	0.13	5.4
Mn	−13.1	0.55	5.9
Ge	−16.4	0.62	6.2
Cu*	−10.6	0.39	6.5
Sc	−11.2	0.40	6.7
Y	−8.8	0.09	7.93
Co	−23.7	0.63	8.8
O*	27.6	1.37	10.8
Ni*	−23.8	0.4	14.3
Si*	−32.5	0.35	21.7
P	−29.1	0.11	25.9
S	−47	→0	47
B	−66	→0	66
Be	−92	0.21	72

The mode of solidification in FZ of the weldments can be explained by the relation correlating the growth restriction factor (Q) with temperature gradient, growth rate and diffusion coefficient is given by[51]

$$\frac{G}{R} = \frac{mC_o(1-k)}{kD} \text{ ---------- (2.3) [51]}$$

Where G represents the temperature gradient, R stands for the growth rate,
m denotes the slope of liquidus line, and C_o represents the alloy composition.
k represents the solute partition coefficient, while D indicates the diffusion coefficient.
The equation (2.3) mentioned above can be employed to anticipate the growth pattern of a solidifying phase. This prediction relies on factors associated with solidification conditions (found on the left-hand side of the equation) and alloy properties (situated on the right-hand side). From the equation (2.3) as the term G/R is minimised which leads to a region of constitutional super cooling ahead of the solid liquid interface and there by increased the tendency of cellular or dendritic growth. The parameters m, k, D and C_o are the properties of alloy which can vary with solute additions. According to the equation (2) higher temperature gradient and lower growth rate favour the stable planar interface. As the constitutional super

cooling increases, the mode of solidification changes from planar to dendritic growth as shown in Fig 2.22. [51]

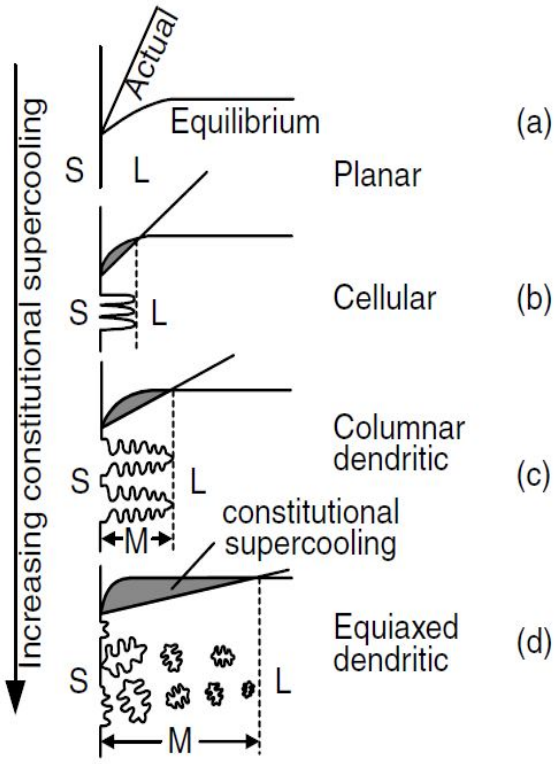

Fig 2.22: Influence of constitutional super cooling on the solidification modes of grains a) planar b) cellular c) columnar dendritic and d) equiaxed dendritic (In this Fig S, M and L denotes the solid, Mushy and liquid zones, resepctively) [51]

Easton and St. John introduced a model for predict grain size by considering the influence of both nuclei and solute on refinement of grain size. This model is represented as [84]

$$d = \frac{1}{\sqrt[3]{\rho.f}} + \frac{b'\Delta T_n}{Q} \quad \text{---------- (2.4)[84]}$$

Where d represents the grain size, ρ stands for density of nucleant particles,

f signifies the faction of these particles that become activated,

b' is a constant, and ΔT_n indicates the undercooling necessary to activate nucleation

The 1st term of Equation (2.4) refers to the availability of nuclei, and the 2nd term relates to the potency (effectiveness) of the nuclei and the development of the constitutionally undercooled zone. Assuming the same number of nucleate population in an alloy with varying values of Q, leads to variation in grain refinement that occurs within the experimental conditions. For simplicity, let us converts the above the equation as [84]

$$d = a + \frac{b}{Q}$$ ---------- (2.5) [84]

If the grain size data is plotted against the inverse of Q (Fig. 2.23), an alloy series containing the same nuclei population will fit a linear trend obeying the above equation (2.5).

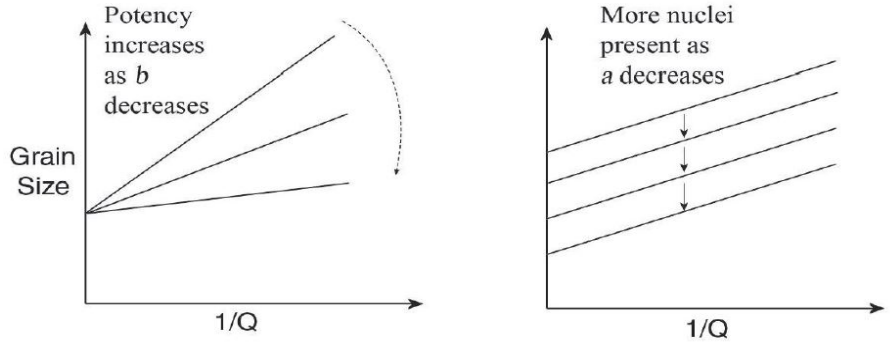

Fig. 2.23: Schematic plot of grain size against 1/Q showing effect of parameters a and b relates to overall grain size [85].

Considering the above two hypothetical graphs of grain size vs 1/Q. It was shown that the gradient (b) represents the potency of the nucleate particles and y-intercept (a) relates the activated nucleus density. As the introduction of more potent nuclei particles to the melt results in decrease of the gradient (b). However, when more of the same nuclei particles were added and become activated, the slope remains constant but y-intercept (a) decreases [85].

Based on past studies on grain refinement of different casting of different alloys systems including titanium alloys made researchers to focus on suitable grain refiners that will give better grain refinement of titanium welds. For example, Lutfi et al. [82] has been used boron modified CP-Titanium fillers in GTAW of meta stable beta titanium alloy Ti-15-3. As the suitable addition of boron results in significant improvement in grain refinement of β grains in FZ can alters the mechanical properties, particularly results in an increase in tensile strength and stiffness in weld joint of metastable β-Ti alloys. It was due to higher growth restriction factor of boron leads to decrease in prior β grain size. Arif et al. [81] has investigated the effect of C as a grain refiner in CP-Ti fillers in GTAW of metastable β-Ti alloy Ti-15-3. It was observed that with the addition of C leads to reduction in β grain size in FZ leads to improvement in tensile strength and hardness. The grain refinement due to limited solubility of carbon in titanium in solid phase by which it can nucleate ahead of S/L interface creates undercooling for further nucleation. The resultant C rich layer retards the β grain growth and promotes nucleation with in the melt results in a smaller grain size. As the introduction of CP-Ti as filler the weldment overall composition shifted to a lower β stabilising region due to

dilution of α-particles in filler with β-particles in base metal results in precipitation of α phase from β phase during cooling to room temperature.

2.11 Titanium-Nickle (Ti-Ni) system:

Fig 2.24 illustrates the binary phase diagram of Ti-Ni system. The maximum solubility of Ni in α-Ti phase is low and does not exceed 0.5 wt.% (0.4 at.%) at the temperature 765°C (1038 K), whereas the Ni content in β-Ti phase is approximately 12 wt.% (10 at.%) at 942 °C (1215 K). From Ti-rich region of the Ti-Ni phase diagram in Figure 2.20, Ti and Ni form three stable compounds, namely Ti_2Ni, TiNi, and $TiNi_3$ at 38 wt.%, 55 wt.% and 78.5 wt.% Ni, respectively [86].

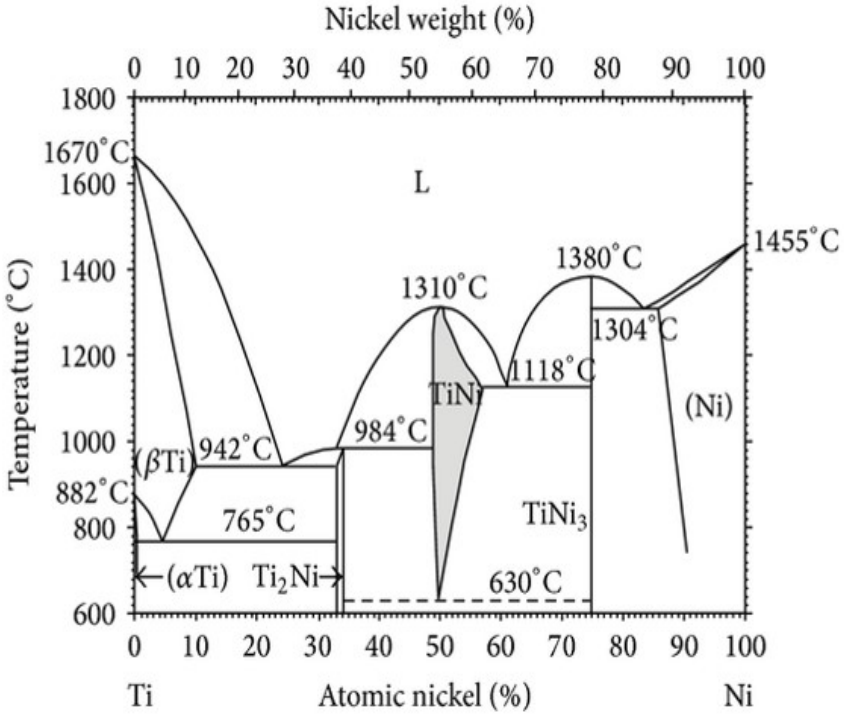

Fig 2.24: The Ti-Ni phase diagram illustrates the equilibrium phases that can be anticipated for various combinations of Ni concentration (wt.%) and temperature (°C).[87].

Within this diagram, these intermetallic phases, primarily exists at higher solute percent. The lever rule reveals that higher nickel concentrations correspond to increased proportions of this intermetallic phase. Based on the Ti-Ni binary diagram, a eutectic reaction occurs at temperature of 942 °C for a Ni concentration of 28.4 wt.% [86]. The eutectic reaction is given as:

$$L \rightarrow \beta + Ti_2Ni_{eutectic}$$

In similar way, the eutectoid reaction takes place at a temperature of 765°C for a Ni concentration of approx. 6 wt.% [86]. The eutectoid reaction is given as:

$$\beta \quad \rightarrow \quad \alpha \quad + \quad Ti_2Ni_{eutectoid}$$

But according to the lever rule, within the β + Ti_2Ni field, the quantity of Ti_2Ni is comparatively lesser when compared to the α + Ti_2Ni domain, for same concentration of Ni. Within the hypo eutectoid region (below eutectoid Ni concentration), the nucleation of α phase starts from β phase. Upon subsequent cooling, below the eutectoid temperature the process of precipitating the intermetallic phase Ti_2Ni commences. At a temperature slightly higher than 765°C, the precipitates of the Ti_2Ni proeutectoid phase emerge within a β matrix of eutectoid mixture. Slightly below 765°C, these precipitates are observed within the eutectoid matrix, forming a granular microstructure wherein α and Ti_2Ni phase [86]. The reactions pertinent to achieving equilibrium solidification at hypo eutectoid Ni concentrations are outlined as follows:

$$\alpha \quad + \quad \beta \quad \rightarrow \quad \alpha \quad + \quad Ti_2Ni \quad (765°C)$$

However, when the eutectoid reaction is inhibited, as occurs when cooling does not take place under equilibrium conditions, there is a likelihood of retaining the β-phase at room temperature, and this tendency becomes more noticeable with higher nickel (Ni) concentrations.

Earlier investigations into the standard dissimilar welding of titanium-nickel alloys have indicated that titanium alloys containing more than approximately 2% nickel tend to develop cracks during the solidification process. Formation of two brittle intermetallic compounds, Ti_2Ni and $TiNi_3$ leads to cracking. But, TiNi, exists in is a ductile compound. If formed, would not contribute to the brittleness of the weldment [88]. As a practical application, the addition of Ni to Ti alloys primarily occurs in the hypoeutectoid concentration range, typically at levels below 0.5 wt% [89].

2.12 Titanium-Silicon (Ti-Si) system:

The technological interest in the Ti-Si system is driven by the advantageous impact of incorporating Si, which enhances oxidation and creep resistance in Ti-Si alloys. Fig 2.25 shows the Ti-Si phase diagram. The maximum solubility of Si in α-Ti phase is low and does not exceed 0.45 wt.% at the temperature 860°C (1133 K), whereas the Si content in β-Ti phase is approximately 3 wt.% at 1330°C (1603 K). From Ti-rich region of the Ti-Si binary phase diagram in Fig 2.25, Ti and Ni forms five silicide phases (Ti_3Si, Ti_5Si_3, Ti_5Si_4, TiSi, and $TiSi_2$).

Within this diagram, these intermetallic phases, primarily exists at higher solute percent. The lever rule reveals that higher Si concentrations correspond to increased proportions of this intermetallic phase. Among these, the Ti_5Si_3 silicide intermetallic formed in the alloys used for high-temperature structural applications due to its commendable corrosion resistance and impressive wear resistance [90].

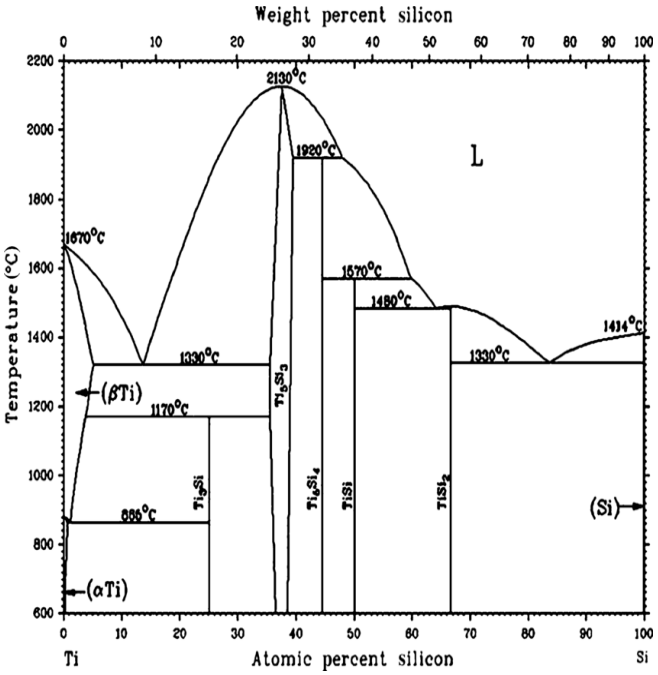

Fig. 2.25: The Ti-Si phase diagram illustrates the equilibrium phases that can be anticipated for various combinations of Si concentration (wt.%) and temperature (°C)[91].

Based on the Ti-Si binary diagram, a eutectic reaction occurs at temperature of 1330°C for a Si concentration of 8 wt% (approx) [90]. The eutectic reaction is given as:

$$L \rightarrow \beta + Ti_5Si_{5\,eutectic}$$

Also, the eutectoid reaction takes place at a temperature of 860°C is:

$$\beta \rightarrow \alpha + Ti_3Si_{\,eutectiod}$$

In the hypo eutectoid region (below eutectoid Si concentration), the α phase starts to nucleate in β phase. For further cooling, below the eutectoid temperature the process of precipitating the intermetallic phase Ti_3Si commences. At a temperature slightly higher than 860°C, the precipitates of the Ti_3Si proeutectoid phase emerge within a β matrix of eutectoid mixture. Slightly below 860°C, these precipitates are observed within the eutectoid matrix, forming a granular microstructure wherein α and Ti_3Si phase [90]. The reactions pertinent to achieving equilibrium solidification at hypo eutectoid Ni concentrations are outlined as follows:

$$\alpha + \beta \rightarrow \alpha + Ti_3Si \quad (860°C)$$

As a practical application, the addition of Si to Ti alloys primarily occurs in the hypoeutectoid concentration range, typically at levels below 0.5 wt% [92].

2.13 Effect of Ni and Si additions on grain size:

A refined grain size enhances numerous mechanical properties, including strength, ductility, and damage tolerance. Furthermore, it improves the response to subsequent mechanical working. Although different PWHT methods have been reported to enhance the strength and ductility of welds to some degree, it is important to note that heat treatment may also lead to coarsening of the grain structure in the BM. It is observed that the grain sizes of cast Ti alloys are relatively coarse due to rapid cooling from high temperatures. By identifying appropriate fillers, it is possible to facilitate the nucleation and growth of the α phase within the β matrix and alter the morphology of β grains. This, in turn, leads to enhancements in the mechanical performance of Ti welds [93]. For instance, Sui et al. [89] have investigated the effect of trace Ni as a grain refiner in Ti-6Al-4V (Ti-64) during laser-aided additive manufacturing (LAAM). It was observed that the addition of Ni leads to a reduction of prior β grain size in Ti-6Al-4V-0.9Ni LAAM built. This can be attributed to the Ni-rich layer at the solid-liquid (S/L) interface retards the growth of β grains. Similarly, Bermingham et al. [85] have studied the effect of various elements like B, Si, Cr, La, and Zr on grain refinement of Ti alloys during casting. They deduced that a limited solubility of the above solute elements in Ti alloys would lead to rejection into the melt ahead of the S/L interface during the solidification, which creates sufficient undercooling in the melt and may restrict the growth of β grains in FZ. Furthermore, according to Ibrahim et al. [92] incorporating 0.5% of Si into cast Ti-64 alloy resulted in an approximately 10% improvement in mechanical properties compared to the as-cast Ti-64 alloy without Si addition. This suggests the Si can be considered a grain refiner to the prior β grains by contributing and developing the undercooled zone ahead of the S/L interface. Deng et al. [23] also studied the influence of traces of Si and Sc addition on grain size refinement during the vacuum arc melting of Ti-64 alloy. They found that both Si and Sc play a prominent role in grain refinement as well as enhance the creep resistance of the alloy. This could be due to the formation of Ti silicide and Al_3Sc particles; the formation will act as a barrier for dislocation movement during creep. Mereddy et al. [94] have also studied effect of trace amount of Si into wire arc additively manufactured Ti components. They reported that increase in Si content

leads to the finer grain sizes (Fig 2.26); however, it does not entirely hinder the development of columnar grains within the microstructure.

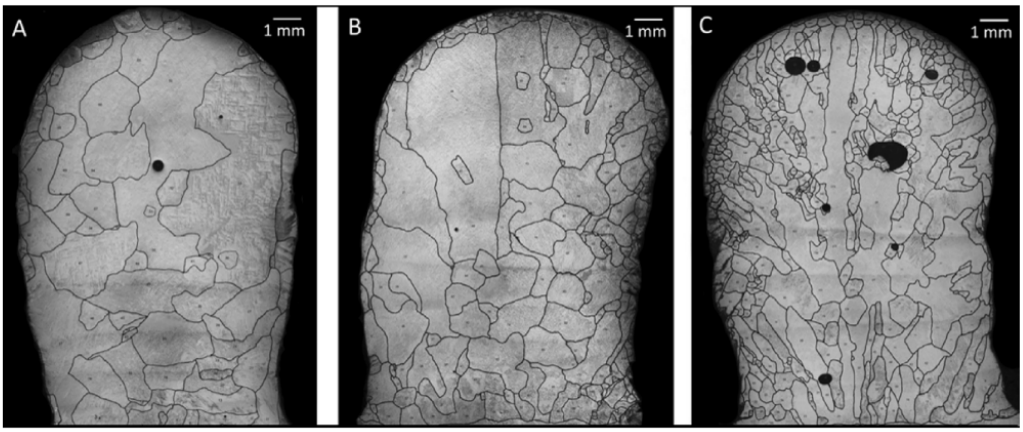

Fig 2.26: β grain structure of additive manufactured CP-Ti with a) 0.04 wt% Si, b) 0.19 wt% Si and c) 0.75 wt% Si. [94]

To date, research regarding grain refinement through the addition of Ni and Si has primarily been confined to cast titanium alloys. It's conceivable that incorporating Ni and Si-modified fillers into the joining of metastable β-Ti alloys could enhance the mechanical response of the FZ while maintaining the strength of BM. As far as our knowledge extends, there is a paucity of information concerning GTAW of titanium alloys utilizing fillers modified with Ni and Si. The utilization of innovative Ni and Si-modified Ti-15-3 fillers for welding Ti-15-3 metastable β-Ti alloys holds the potential to refine the coarse columnar β grains within the FZ and foster increased nucleation of the α-precipitates within β matrix during PWHT. The current study is focused on assessing the impact of Ni and Si-modified Ti-15-3 fillers on microstructure, phase formation, tensile properties and hardness of GTAW weldments in Ti-15-3 alloy.

2.14 Post-Weld Heat Treatment Effects:

Generally, most of the materials which are welded can be subjected to PWHT for minimising the internal stresses that are locked in weld structure during cooling. These internal stresses may lead to cracks that can be avoided by PWHT. Other major benefits that can be obtained by PWHT are improves ductility by reducing hardness in welds, it also stabilize and homogenising the weld zone microstructures and enhancing the mechanical properties [95]. For these reasons the metastable β-Ti alloys are subjected to post weld aging for improvement in strength and ductility of the weld zones. Commonly, metastable β-Ti alloys can be heat

treated above β transus temperature that retains β phase at room temperature which was ductile in nature. Later on sub-trances aging treatment in the range of α+β phase field leads to transformation of some of the β phase by precipitation of finely dispersed α phase which attributed to increase in strength. Greenfield et al. [96] has observed the variation of strength of the weld zone after post weld aging of Ti-8Mo-8V-2Fe-3Al a Meta stable beta titanium alloy at different aging temperatures and time. This variation in strength depends on the concentration and homogeneity of formation of α phase in β matrix.

In the investigation of Becker et al. [97] on GTA welded Meta stable beta titanium alloys Ti-15-3, Ti-8V-4Cr-2Mo-2Fe-3Al and Ti-8V-7Cr-3Al-4Sn-1Zr found a significant gain in strength of the welds after aging treatment. However each of these alloys show different aging response depending aging temperature and time. In as welded condition due to formation of metastable beta phase in fusion zone and near heat effected zone experience the very high ductility and lower in strength. The post weld aging treatment of these alloys results in optimum combination of strength and ductility. Kuroda et al. [98] has examined the GTA welded Ti-15-3 after the aging treatment has observed that the more volume fraction of alpha precipitation was occurs at higher solution treatment temperature irrespective of the aging temperature of the welds. It was shown that the solution treatment at 1073 K and followed by aging found the coarse alpha phase precipitation being more non-uniformly distributed with increasing aging time whereas the solution treatment at temperature 1573 K and found fine α phase precipitation but more densely distributed with increasing aging time. The variation in refinement and homogenization of alpha phase is due to increase in vacancy concentration associated with an increase in temperature of solution treatment during aging process. As these vacancies acts as nucleation sites for precipitation of alpha phase and hence the higher solution treatment temperature are considered to be dominant factor for enhancing the aging characteristics. Lin et al. [24] have studied the effect of high-temperature PWHT on EBW of Ti-1533. They found that PWHT at 538˚C exhibits a higher YS of 1178 MPa, UTS of 1257 MPa and % El of 10 when compared to as-welded condition (YS 870 MPa, UTS 878 MPa, % El 8).This is because of the formation of fine nano α precipitates in the FZ.

However, a number of studies have revealed that compared to single-step ageing of beta titanium alloys, duplex aging (two step) is known to enhance the mechanical characteristics [26, 29]. The initial aging temperature was indicated as first step aging which followed by another aging temperature that indicates the second step aging. The study reveals that the fine alpha phase at first step aging at 673K and coarse α phase under the second step aging at 773

K with changes in volume fraction of α phase precipitation in first and second step of aging of the welds. It has been noted that under single step aging, an aging time necessary to achieve the preferred hardness will be more than that of second step aging. Likewise one more approach to increase the alpha precipitation is cold rolling and followed by aging treatment. Due to which the concentration of dislocations, atomic vacancies will increase in the alloy that acts as nucleation sites for the precipitation of fine alpha phase. As in two step aging process here also there will be shorten of aging time. It was observed that under low aging temperature below say 573 K, ω phase will tends to precipitate. As ω phase will degrade the mechanical properties its formation should be minimised to large extent. So, it is better to maintain the higher aging temperature [29]. Furthermore Nihal et al. [26] demonstrated that two-step aging (523 K, 10 h + 723 K, 20 h) of the Ti-1533 alloy leads to the formation of fine of α precipitates uniformly distributed in β matrix as compared to single-step aging (823 K, 10 h). They showed the increase in hardness is due to duplex aging of the alloy. Santosh et al. [46] have also proved that duplex aging of Ti-1533 alloy resulted in better fatigue life because of a higher density of α precipitation.

2.15 Mechanical properties:

The mechanical characteristics of Ti alloys have garnered significant attention due to their utilization in biomedical, aerospace, and industrial applications. Especially α + β Ti alloys and metastable β-Ti alloys are two major group of Ti alloys show good mechanical properties like yield strength, tensile strength compared to that of α-Ti alloys. However α+β Ti alloys exhibit less tensile elongation compared to that of β-Ti alloys. Hence metastable titanium alloys have become most favourable alloy for many high strength structural applications. Generally mechanical properties of the material strongly influenced by the microstructural changes and testing environment. The microstructure influences the modes of deformation, such as slip or twinning, that are associated with the material's mechanical behavior. So, it is necessary to understand the effect of microstructure on mechanical characteristics of weldments provides a basis for fundamental way to produce the welds of superior mechanical properties [99].

The microstructure of titanium weldments, especially the phases present and their morphologies governs the mechanical properties of the welds. In β-Ti alloys, the significant microstructural constituents that influence the mechanical properties are prior β grain size, the morphology of phase present, volume fraction of α phase and α phase present at grain boundary. In welding the microstructure depends on rate of solidification and composition of

alloy. Therefore, it is essential to assess the impact of the weld microstructure on the mechanical properties of beta titanium alloys.

2.15.1 Hardness:

The hardness values in beta titanium alloys can be governed by the amount of precipitation of α phase in β matrix. The size, morphology and distribution of α significantly vary the hardness along the BM-HAZ-FZ. From the investigation of pasang et al. [17] on GTAW of Ti-5Al-5V-5Mo-5Cr, a metastable beta titanium alloy has shown a decrease in hardness of HAZ and FZ compared to that of BM. As the micrographs of HAZ region shows large equiaxed β grains and FZ decorated with large columnar β grain morphology results in decrease of hardness in both regions. Wang et al. [100] have shown the comparison of hardness values along the weld profile in GTA welded CP-Ti, Ti-6Al-4V an α + β Ti alloy and Ti-15V-3Al-3Cr-3Sn a metastable β-Ti alloy. It was reported that the hardness in FZ in CP-Ti and Ti-64 are higher than that of the Ti-15333. The raise hardness in FZ of CP-Ti and Ti-64 is due to formation of martensitic phase (α-prime) where has in Ti-15333 there is no such formation. From the studies of Balachander et al. [16] hardness values of pulsed GTAW of Ti-15333 has found that the higher hardness in pulsed mode compared to that of the continuous current mode of welding. This variation in hardness is due to difference in cooling rate and heat input in continuous mode and pulsing mode. Kuroda et al.[98] have reported that GTA welded Ti-15333 alloy showed the increase in hardness after post weld aging compared to that of the aswelded condition. It was studied that the increase in hardness with increase in solution treatment temperature and followed by aging. This is due to volume fraction of α increase as the solution treated at high temperature. In further studies of Kuroda et.al [29] has done two step aging treatment of the GTA welded Ti-15333 alloy deduced the increase in hardness of the samples aged at higher solution treatment but at less aging time to achieve required hardness. The hardness will increase due to precipitation of fine α in second step aging. Arif et al. [81] have reported the hardness in FZ of GTA welded Ti-15333 in can be improved by modifying the filler with suitable solutes like B and C. The higher growth restriction factor of the solute can be used to restrict the columnar grains growth in FZ resulting in grain refinement. The increase in hardness can also attributed to the formation of TiB and TiC precipitates at β grain boundary and also with in β grains.

2.15.2 Tensile properties:

The weld specimens can be tested on universal testing machine (UTM) from which obtained stress-strain curves used to determine the YS, UTS and percent %El. Wang et al. [100] has tested the GTA welded CP-Ti, Ti-64 andTi-15-3 alloys at different strain rates found with increasing the strain rate there is an increase in flow stress of the weldments. The CP-Ti showed the lowest strength with more elongation because of their low work hardening character whereas in Ti-64 shows highest YS and UTS due to formation of hardened martensitic phase in the FZ and HAZ. However, Ti-15-3 alloy exhibit moderate strength and ductility. Sabol et al.[101] conducted an investigation into the localized tensile strain distribution during EBW of Ti-5553. Their findings revealed that the weld FZ experiences a peak localized strain of approximately 6.31%. This observation corroborates the notion that the presence of large grains of retained β in the FZ renders it vulnerable to failure. Balachandar et al.[16] have reported the higher strength and moderate elongation for the pulsed GTA welded sample subjected to post weld aging in contrast the pulsed current GTA aswelded samples showed the moderate strength with optimum elongation. The higher strength in post weld aging is due to uniform precipitation of α in retained β phase whereas the moderate strength in pulsed GTAW as welded samples is due to grain refinement of the FZ due to higher cooling rate. The GTAW continuous current mode showed the lowest strength compared to that of the base metal which is due to grain coursing because of slow cooling rate. Anis et al. [82] have reported the tensile properties using a stress-strain curves of GTAW of Ti-15-3 with Boron (B) and Carbon (c) added fillers. The reported that the welds prepared using the B and C modified fillers found increase in UTS, YS and elongation compared to that of the autogenous welds. The higher strength is due to the insoluble TiB and TiC particles at β grain boundaries and also within the β grains which impedes the motion of dislocation. The lower strength in autogenous welds is due to formation of coarse β columnar grains in FZ and large equaixed grains in HAZ.

3. EXPERIMENTAL DETAILS

3.1 Experimental flow chart:

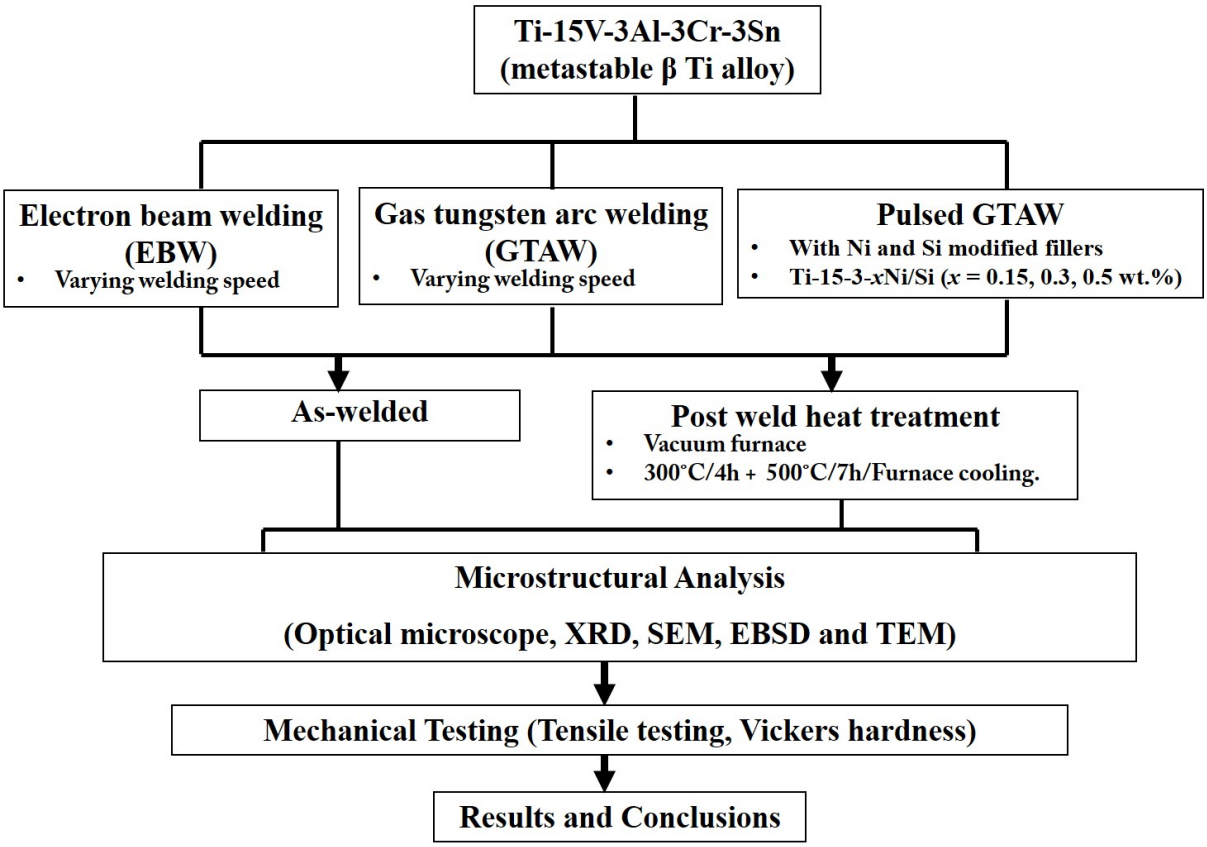

3.2 Materials and Equipment:

The materials and equipment utilized in the research experiment are detailed in Table 3.1 below.

Table 3.1: Materials and equipment used:

Title	Material/Equipment
Raw materials	Ti-15V-3Al-3Cr-3Sn (Ti-15-3) meta stable β alloy plates, Nickel (Ni), and Silicon (Si) powders (99.9% purity).
Chemicals	Ethanol, acetone, Hydrofluoric acid (HF), Nitric acid (HNO_3), Distilled water, colloidal diamond suspension.

Apparatus	Ceramic crucible, beakers, spatula, stainless-steel brush, hand gloves, analytical balance, screw gauge, vernier caliper, tongs, Vacuum furnace, Low speed saw diamond cutter (Chennai metco), and Desiccator.
Instruments	Gas tungsten arc welding (GTAW), Electron beam welding (EBW), Argon arc melting (VEC Solutions, Bangalore, India), optical microscope (QUASMO QMM 500), X-ray Diffractometer (PANalytical X'pert), Scanning electron microscope (TESCAN) equipped with energy dispersive spectroscopy (Oxford instruments), electron backscatter diffraction (FEG JEOL 7800F), High-resolution transmission electron microscope (Thermo Fisher Scientific Themis 300) , Vickers hardness tester (Shimadzu HMV-G20S, Japan), Universal testing machine (Jinan WDW-100S, China).

The chemical composition of the selected alloy, Ti-15-3, was analyzed. The Ti-15-3 base metal contained the following elemental composition: 14.19 wt.% Vanadium (V), 3.75 wt.% Aluminum (Al), 2.54 wt.% Chromium (Cr), 3.44 wt.% Tin (Sn), 0.18 wt% Oxygen (O), O.15% C, 0.05 wt.% Nitrogen (N) with the remaining weight percentage being Titanium (Ti).

3.3 Welding details:

Weld coupons, measuring 120 x 110 x 3 mm, were fabricated from the initially received sheets sized 500 x 500 x 3 mm. The preparation involved a consistent sequence of stainless-steel wire brushing, acid pickling in a diluted HF solution, and degreasing the surface with acetone to remove the surface oxide films. Welding was performed with beads arranged in a manner perpendicular to the rolling direction. Autogenous full-penetration bead-on-plate EB welds and GTA welds were made on the coupons.

3.3.1 Electron beam welding:

A low-voltage EBW machine (manufactured by Techmeta, France) operating at 100 kV, located at the Defence Research and Development Laboratory (DRDL) in Hyderabad, India (Fig 3.1) is used in this current study. This machine is equipped with an advanced beam deflection system capable of programming various beam oscillation patterns. The coupons were clamped with a specially designed fixture employed during welding, featuring adjustable gun-to-work adjustment flexibility which provides minimal restraint. To achieve optimal results, extensive preliminary welding trials were conducted using different combinations of welding parameters. The goal was to identify the ideal welding parameters that would result in sound welds with full penetration, while minimizing issues such as spattering, porosity, undercutting, and rough bead appearance, among others. Hence three different traverse speeds were explored to assess their influence on the microstructural and mechanical behaviour of welded joints. The optimized EBW parameters are detailed in Table 3.1.

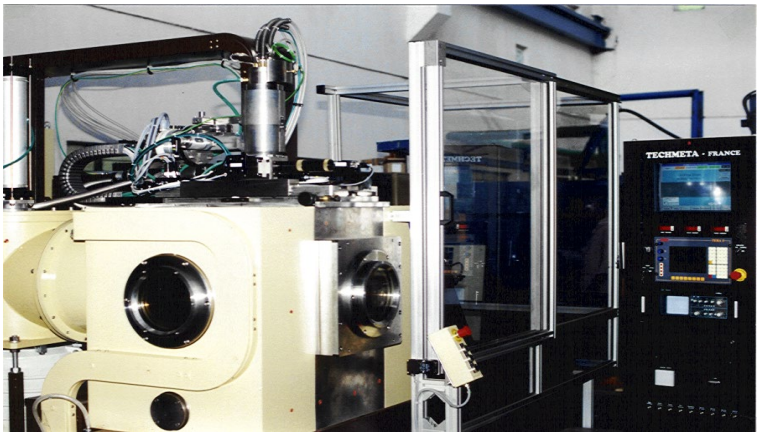

Fig 3.1: EBW machine used in the present investigation

Table 3.2: Welding parameters for EBW of Ti-15-3

Beam Voltage (kV)	**Beam Current (mA)**	**Focus**	**Welding speed (mm/min)**	**Heat input (kJ/mm)**
100	20	330	500	0.240
100	22	330	700	0.188
100	24	330	800	0.180

Other operating parameters: vacuum = 1.5×10^{-4} torr, frequency = 15 Hz, gun-to-work distance = 284 mm

3.3.2 Gas Tungsten arc welding:

For the GTA welding of Ti-15-3 sheets, ESAB equipment (Tig 4300i AC/DC) was employed (Fig 3.2). This power source offered the capability to generate pulsed current output, allowing for control over parameters such as peak current, base current, frequency, and time at peak and base current cycles. Initial trials of GTA welds were carried out using automatic DC-GTA welding. To minimize the presence of tungsten inclusions, the electrode's edge was ground to a hemispherical shape as DC was the chosen welding current. Furthermore, auxiliary backing and trailing argon (Ar) gas shields were employed alongside torch gas, utilizing custom-designed equipment for this purpose. The welding setup is illustrated in Fig 3.3. The actual welding process is assessed by conducting the welding at varying welding parameters such as welding voltage, current, and welding speed. This variation allowed for the selection of suitable welding parameters and inert gas flow rates that resulted in visually sound weld beads. The aim was to identify the ideal welding parameters that would result in sound welds with full penetration. Hence three different traverse speeds were explored to assess their influence on the microstructural and mechanical behaviour of welded joints. The optimized GTA welding parameters are detailed in Table 3.2.

Fig 3.2: Power source used in GTA welding

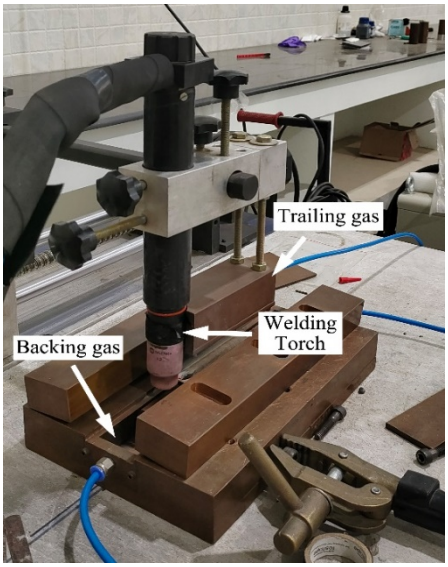

Fig 3.3: The welding setup used in GTA welding

Table 3.3: Welding parameters for GTA welding of Ti-15-3

Voltage (V)	**Current (A)**	**Welding speed (cm/min)**	**Heat input (kJ/mm)**
11.5	125	15	0.575
11.5	125	20	0.431
11.2	125	25	0.336

3.3.3 Filler preparation:

Further in this study, Ni and Si-modified Ti-15-3 fillers were prepared with the nominal composition Ti-15-3-x wt.% Ni and Ti-15-3-x wt.% Si (x = 0, 0.15, 0.3, and 0.5). For the fabrication of these fillers, an Ar arc melting furnace (Fig 3.4) equipped with a non-consumable tungsten (W) electrode (Fig 3.5a) placed on a water-cooled copper (Cu) hearth was employed. The melting occurred in an argon atmosphere at a pressure of approximately 0.3-0.4 atm. The starting materials used to prepare the Ni and Si-added Ti-15-3 fillers were Ti-15-3 pieces and Ni and Si metallic powders with 99.9% purity. The filler metals were melted, resulting in the formation of rods measuring approximately 60 mm in length (Fig 3.5b). These rods were then appropriately sectioned to obtain welding fillers for further use. The welding parameters for pulsed GTAW welds using Ni and Si-modified fillers are shown in Table 3.3.

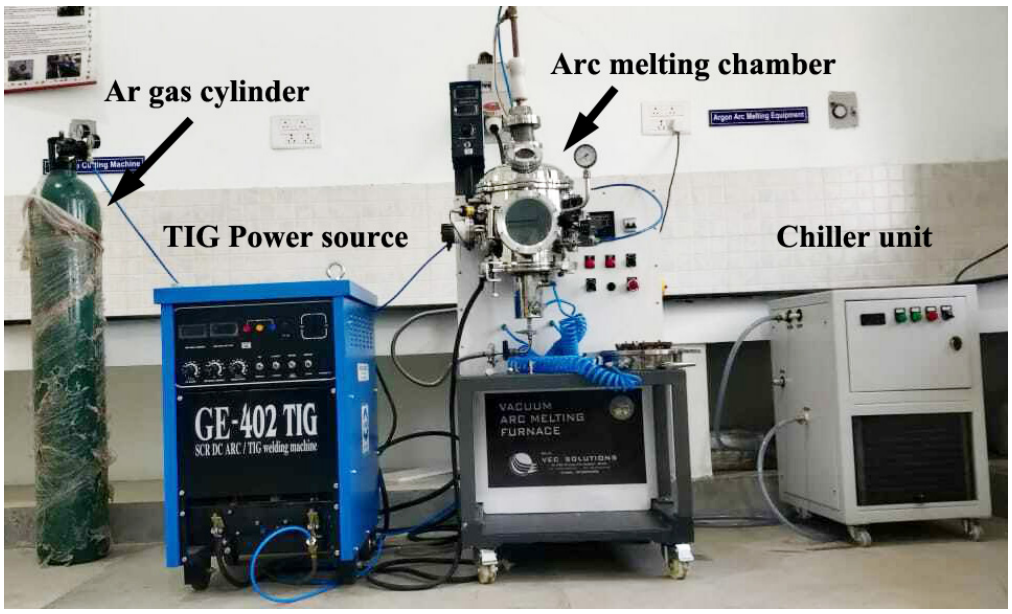

Fig 3.4: Argon arc melting set up.

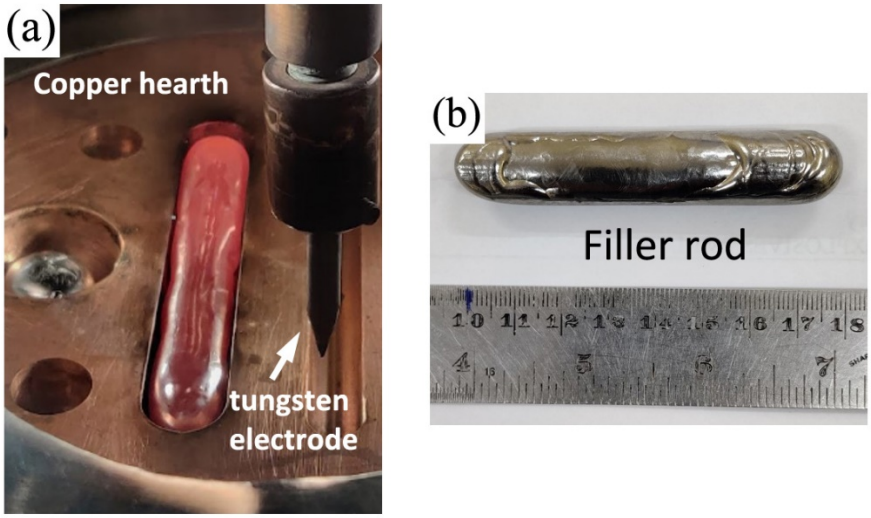

Fig. 3.5 (a) Filler rod preparation in melting chamber (b) dimensions of filler rod.

Table 3.4: Welding parameters for pulsed GTA welding of Ti-15-3 welds made using Ni and Si-modified fillers

Peak Current (A)	**240**
Background current (A)	50
Peak Time (s)	0.15
Background Time (s)	0.1
Frequency (Hz)	4
Average current (A)	164
Voltage (V)	10.5

Welding Speed (mm/min)	150
Arc gap (mm)	2
Thermal efficiency of GTAW	0.6
Heat input (KJ/mm)	0.688

3.4 Post-weld heat treatment:

After the completion of the welding, a few welded coupons underwent a two-step aging heat treatment process. The first step involved pre-aging at 300°C for 4 hours, followed by aging at 500°C for 7 hours in a vacuum atmosphere. Subsequently, the samples were cooled to room temperature in a furnace atmosphere. Finally, these specimens were prepared for metallography analysis and mechanical testing, allowing for comparison with the as-welded samples. The schematic of the heat treatment cycle is represented in Fig 3.6.

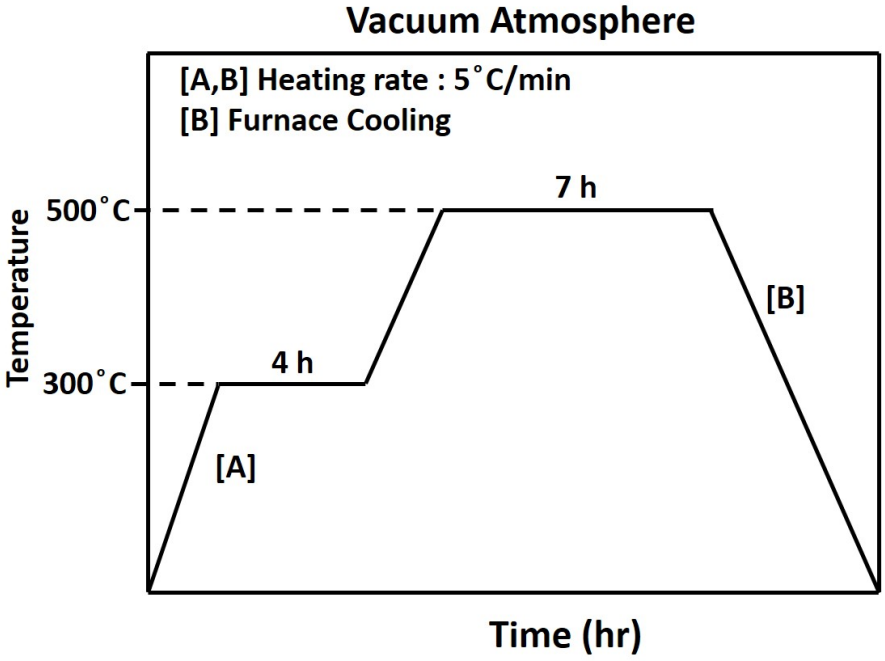

Fig 3.6: Schematic of the heat treatment cycle employed in the PWHT of the welded samples.

3.5 Metallography:

A few weld cross-section samples were extracted from the welded plates and hot-mounted using Bakelite powder. Standard metallography practice was carried out on the as-welded and PWHT samples consisting of rough polishing from 600 to 2000 SiC emery papers, followed

by fine polishing on cloth with colloidal diamond suspensions. Subsequently, etching was done on the samples with Kroll's reagent (3% HNO_3 and 2% HF in 95% distilled water) for microstructural studies.

3.5.1 Light microscopy:

The microstructural features of the welds were examined using an optical microscope (QUASMO QMM 500) as displayed in Fig 3.7, while macrostructural features were observed using a stereomicroscope (Leica Microsystems). The grain/phase size was measured based on the line-intercept method.

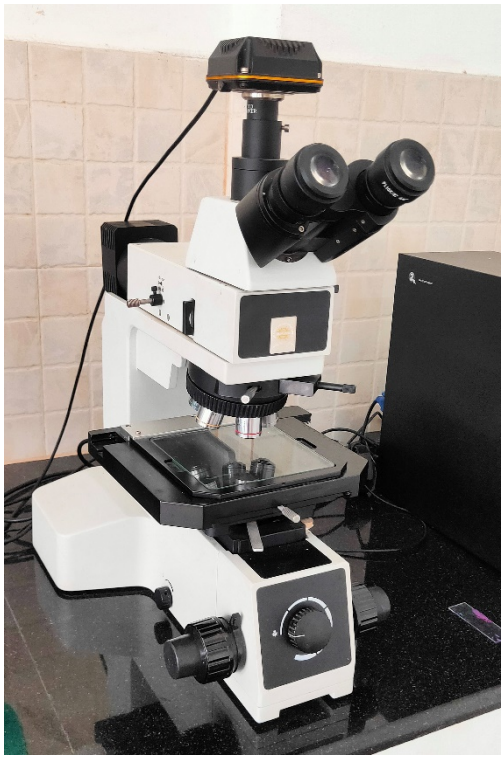

Fig 3.7: Optical microscope used for examination of microstructure

3.5.2 X-ray diffractometry (XRD):

The specimens designated for XRD analysis were selected from the welded portion of the sample and were suitable for the equipment's specimen holder (PANalytical X'pert powder). The XRD analysis was conducted to identify the phases present in the samples. A detector

captured the sample's structure using copper (Cu Kα) radiation source, with diffraction angles ranging from 20 to 90° in 2θ. The scanning rate employed was 2° per minute.

3.5.3 Scanning Electron Microscope (SEM):

The weld morphology, chemical composition, and fractured surfaces were examined using a TESCAN SEM equipped with EDS (Oxford instruments) as displayed in Fig 3.9. The EDS analysis identifies elements and respective compositions in the microstructural region. Also, EBSD is a well-established accessory for the SEM, which is used to provides detailed information about the crystallographic nature (preferred orientation of crystals), phase identification, phase distribution, local strain variation, etc., Hence, the EBSD studies were performed using a FEG JEOL 7800F EBSD detector using a step size of 10 nm and an accelerating voltage of 20 kV.

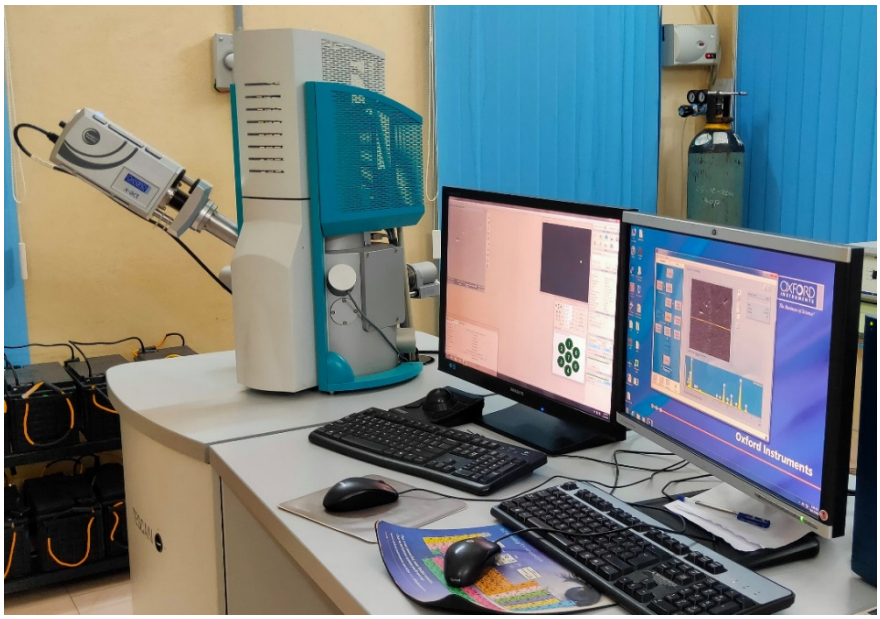

Fig 3.9: SEM used for examination of microstructure

3.5.4 Transmission Electron Microscope (TEM):

For TEM analysis of weld samples, thin slices with a thickness of ~125µm, were initially obtained from the specimens using a low-speed precision cutter. These slices were then further reduced to a thickness of 0.03 mm through mechanical polishing. Subsequently, discs measuring 3 mm in diameter were punched out from these thinned slices. These discs

underwent final thinning using a Fischione 1050 ion milling system, which operated at 2-5 kV with an ion beam angle of 7°. The resulting thin foils were subsequently examined using a Thermo Fisher Scientific Themis 300 TEM operating at 200 kV.

3.6 Mechanical Testing:

3.6.1 Hardness:

The Vickers micro-hardness measurements (Shimadzu HMV-G20S, Japan) were made across the weld regions at intervals of 0.5 mm using a load of 200 g for dwell time of 15 s in both as-welded and PWHT conditions by a diamond pyramid indenter (Fig 3.10). The hardness values were measured using the formula

$$\text{Hardness (HV)} = \frac{1.854\,P}{dl^2} \quad \text{------} \quad (3.1)$$

Where P is the applied load in kg and dl is the diagonal length of diamond pyramid indentation in mm.

Fig 3.10: Vickers micro hardness for testing of samples

3.6.2 Tensile testing:

Uniaxial transverse tensile test specimens were prepared using the electro-discharge wire-cut machine (EDM) to minimize strain involvement and material loss. These specimens were prepared and subsequently tested at room temperature. Transverse tensile test samples were machined from each of the welded samples. The dimensions of the transverse tensile test samples followed ASTM E-8 standards, while miniature-sized samples were employed for the all-weld specimens, as depicted in Fig 3.11. A set of two sub-sized specimens was made from each weld joint (welded coupon) with the FZ located at the centre of the gauge length for tensile testing. The tensile tests were carried out on a UTM (Jinan WDW-100S, China) at room temperature for the all the specimens with a cross-head speed of 0.5 mm/min using a 100 kN load cell.

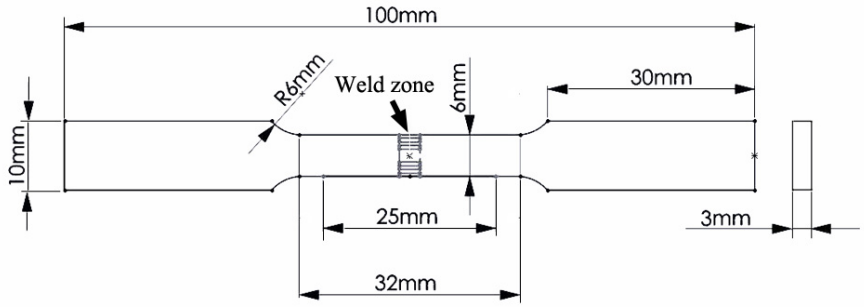

Fig 3.11: Schematic of tensile specimen separated from metal coupon

4. RESULTS AND DISCUSSION-I

Effect of welding speed on microstructural and mechanical properties of EB Ti-15-3 welds

4.1 Base material:

The optical microstructure of the Ti-15-3 BM is shown in Fig 4.1a. It can be observed that the microstructure consists of equiaxed β grains. Fig 4.1b is a scanning electron micrograph of the parent metal also showing the equiaxed β grains. The average grain size and Vickers hardness value of base metal are 74 ± 10 μm and 270 ± 4 HV, respectively.

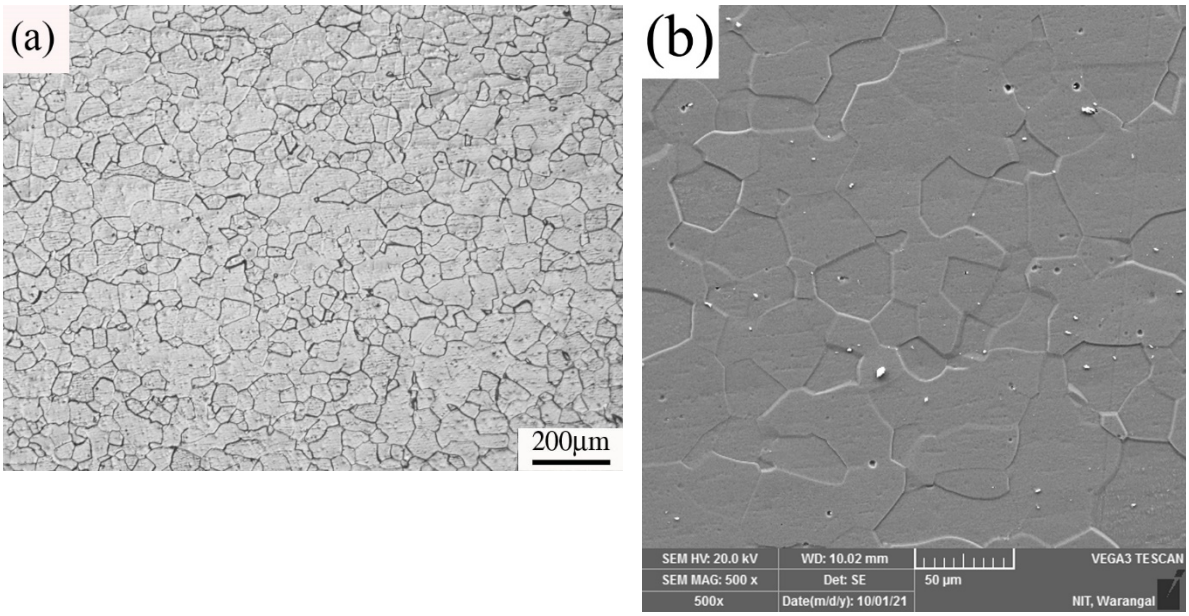

Fig 4.1: (a) Optical microstructure of Ti-15-3 BM (b) SEM of the base metal

4.2 Macrostructure of welds in the as-welded condition

The macrographs in the transverse cross-section of weldments at three welding speeds (500, 700, and 800 mm/min) are shown in Fig 4.2. It clearly reveals the variation in weld bead geometry with respect to three welding speeds. It can also be observed that the complete penetration butt joints were achieved by the EBW process for all welding speeds. The heat inputs used for the EBW welds in this study are 240, 188, and 180 J/mm, with a corresponding welding speeds of 500, 700, and 800 mm/min, respectively. The average bead width from top to bottom of the weld cross-section for different welding speeds, viz., 500, 700, and 800 mm/min, are ~3, ~2.5, and ~2.2 mm, respectively. Clearly, there is a decrease in bead width

as the welding speed increases. This is because of decrease in the heat input and an increase in the cooling rate. All the welds exhibited columnar grain morphologies in FZ, coarse equiaxed grains in HAZ and fine equiaxed grains in BM. This variation in microstructure across the weld can be linked to the thermal cycles experienced during welding. The FZ of the welds at higher weld speed (800 mm/min) consists of columnar grains adjacent to the fusion line and equiaxed, fine grains in the weld root (Fig 4.2c). In contrast, the welds at lower welding speeds (500 mm/min and 700 mm/min) exhibit columnar growth throughout the FZ. These columnar grains grow epitaxially in the mode of direction perpendicular to the fusion boundary. As the thermal gradients are larger near the fusion boundary, the unmelted base metal grains near the fusion boundary act as a substrate for nucleation for epitaxial growth.

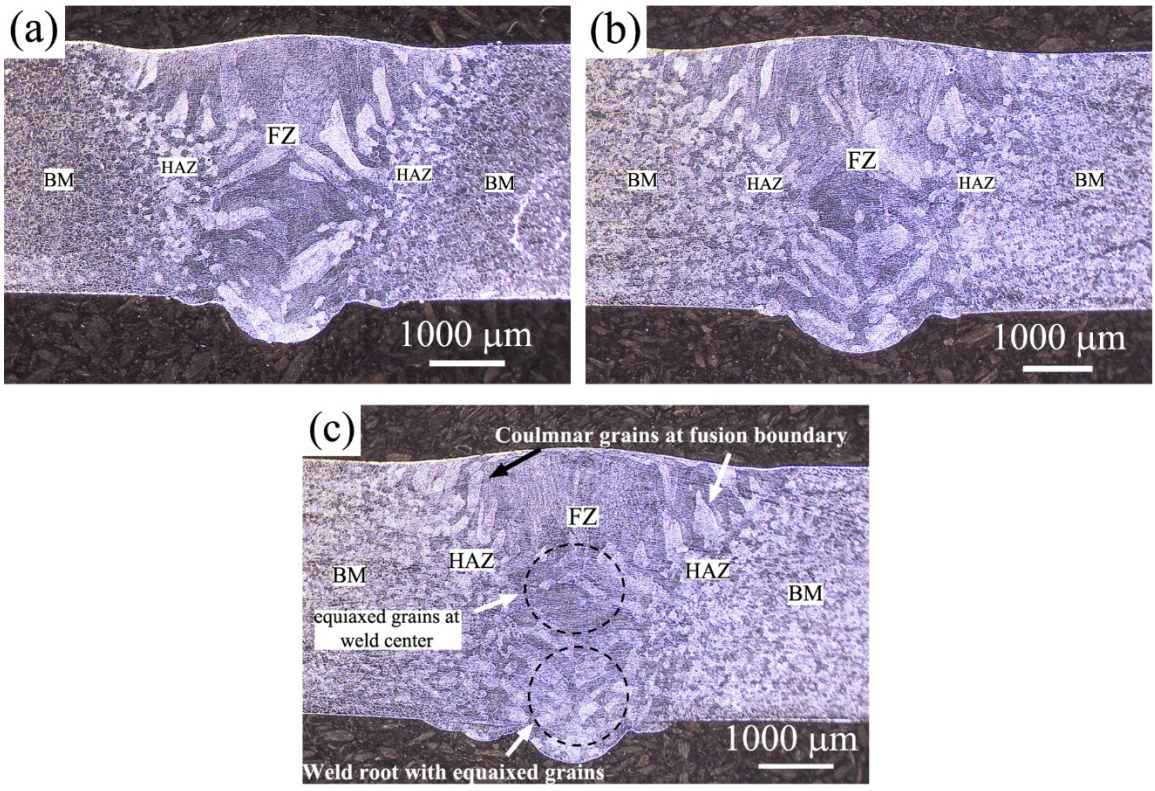

Fig 4.2: Macrostructure of the cross-section of as-welded EB welds at (a) 500 mm/min, (b) 700 mm/min and (c) 800 mm/min welding speeds.

As explained earlier, the FZ macrostructure in Ti-15-3 weld at 800 mm/min welding speed consists of two parts: columnar grains at the upper portion of the FZ while the lower side of the FZ and weld root showed equiaxed grains. This phenomenon can be explained by the growth rate (R) and temperature gradient (G) which significantly vary across the FZ of the weld. Generally, weld metal solidification occurs in a columnar mode where grains grow epitaxially from the fusion boundary towards the centre due to a sharp G at the fusion boundary.

It should be noted that the upper portion of the FZ is the hottest in the weld pool and thermal gradients are maximum.

In contrast, at the lower portion of the FZ and weld root, the G becomes lower and R will be higher, resulting in a constitutional supercooling zone ahead of the S/L interface, which gives rise to the formation of equiaxed grains at the lower FZ and root [57]. Further, higher welding speed (800 mm/min) results in lower peak temperatures in the root of weldment compared to the top region. This results in faster cooling and lowers thermal gradients in the root resulting in equiaxed grains. In other words, welds with higher welding speed lead to faster cooling rates resulting in low heat input and greater constitutional supercooling; hence more nuclei will survive, resulting in fine equiaxed grains in the lower FZ and weld root. Thus in 800 mm/min welding speed, the FZ exhibits the formation of coarse columnar grains at the upper portion of the FZ and fine equiaxed β grains at the lower FZ and root.

4.3 Microstructure of welds in as-welded condition

Optical micrographs of as-welded electron beam welds at different welding speeds (a) 500 mm/min, (b) 700 mm/min and (c) 800 mm/min are presented in Fig 4.3. In all the conditions, solidification takes place epitaxially in the form of coarser β grains from the fusion line towards the centre of the weld. It is observed that the width of columnar β grain decreases with an increase in the welding speed. By using relatively lower heat inputs in case of higher welding speed (800 mm/min), the width of prior β grains decreased, which could be due to faster cooling rates. As the heat input decreases, the cooling rates become higher, leading to a high degree of undercooling, resulting in more nuclei surviving in the weld centre. In other words, as R is higher at the weld centre, due to higher constitutional supercooling gives rise to equiaxed grains in the weld centre and root at higher welding speed (800 mm/min). In contrast, lower growth rates because of the slower cooling rates at lower welding speeds (500 mm/min, 700 mm/min) result in columnar growth throughout the FZ. It is to be noted that the aspect ratio (length/width ratio) of columnar grains in FZ is highest for welds made at 800 mm/min and lowest at 500 mm/min welding speed. The grain size measurement in the welds prepared using welding speeds of 500, 700 and 800 mm/min showed average grain diameters of ~196, 177 and 152μm, respectively.

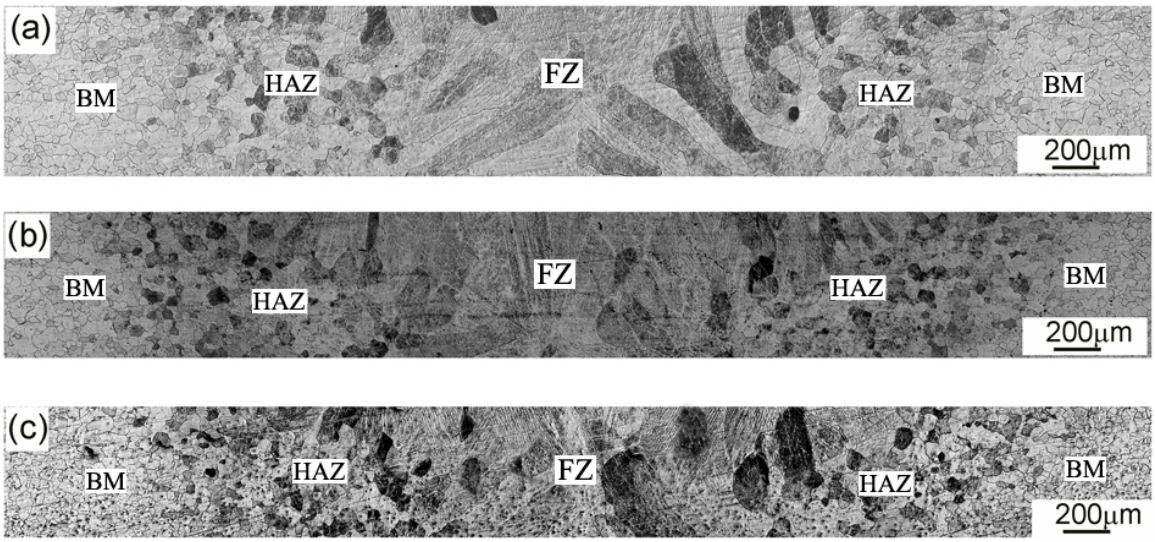

Fig 4.3: Optical micrographs of as-welded EB welds at different welding speeds (a) 500 mm/min, (b) 700 mm/min and (c) 800 mm/min.

SEM of as-welded EB welds showing β-grain boundaries in FZ at a welding speed of 700 mm/min, is shown in Fig 4.4. Higher magnification of welds shows grain boundaries and no traces of transformation product are observed at grain boundaries.

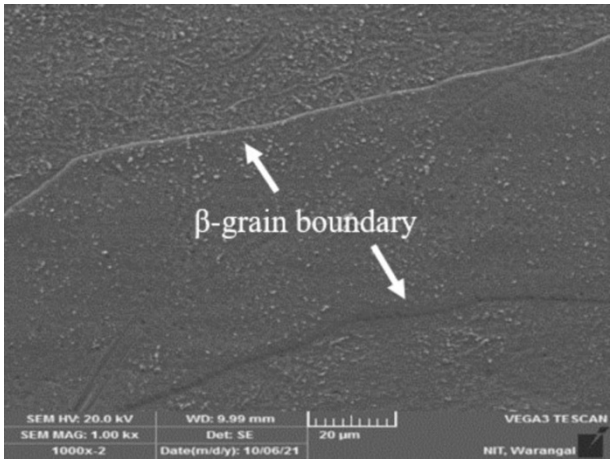

Fig 4.4: SEM of as-welded EB welds showing β-grain boundaries in FZ at a welding speed of 700 mm/min.

Fig 4.5a shows the EBSD inverse pole figure (IPF) map for the electron beam welded Ti-15-3 sample in the as-welded condition at a welding speed of 500 mm/min. The grains in the FZ are columnar and are randomly oriented, having a mean grain size of 196 ± 5μm, as shown in Fig 4.5b. The columnar grain shape is attributed to the high cooling rate it experiences during the welding.

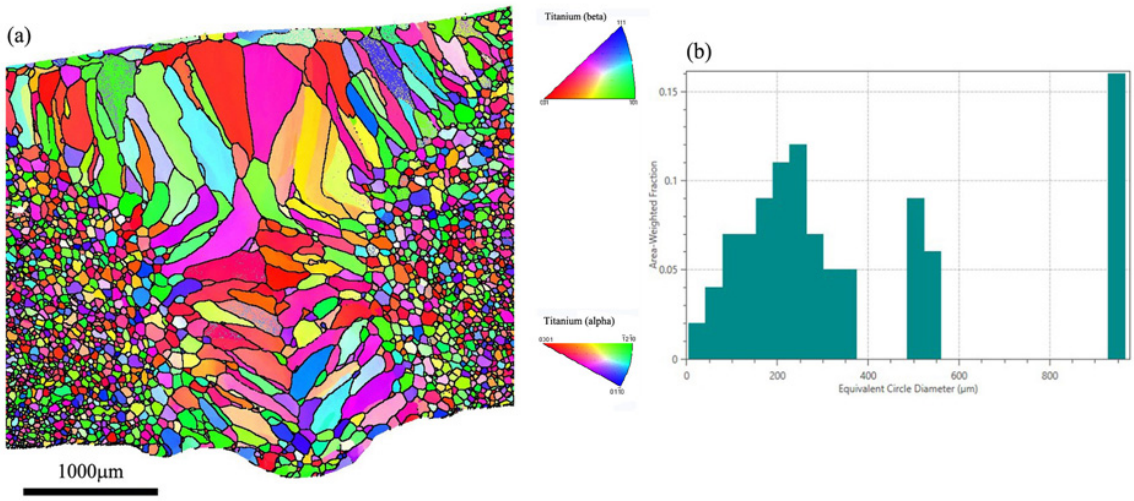

Fig 4.5: (a) EBSD image of electron beam welded Ti-15-3 in as-welded condition at a welding speed of 500 mm/min and (b) corresponding grain-size distribution in the FZ.

Fig 4.6(a,b) shows the fusion zone TEM image of Ti-15-3 EB welds prepared with varying welding speeds (a) 500 mm/min and (b) 800 mm/min, respectively. The FZ diffraction pattern in Figure 7(c) confirms the β phase. The faster weld cooling rates during EBW and the high amount of β stabilising elements in the base metal have resulted in the β phase at room temperature in the as-welded condition. Lin et al. [24] have also found similar observations in most areas of FZ in EB weldments.

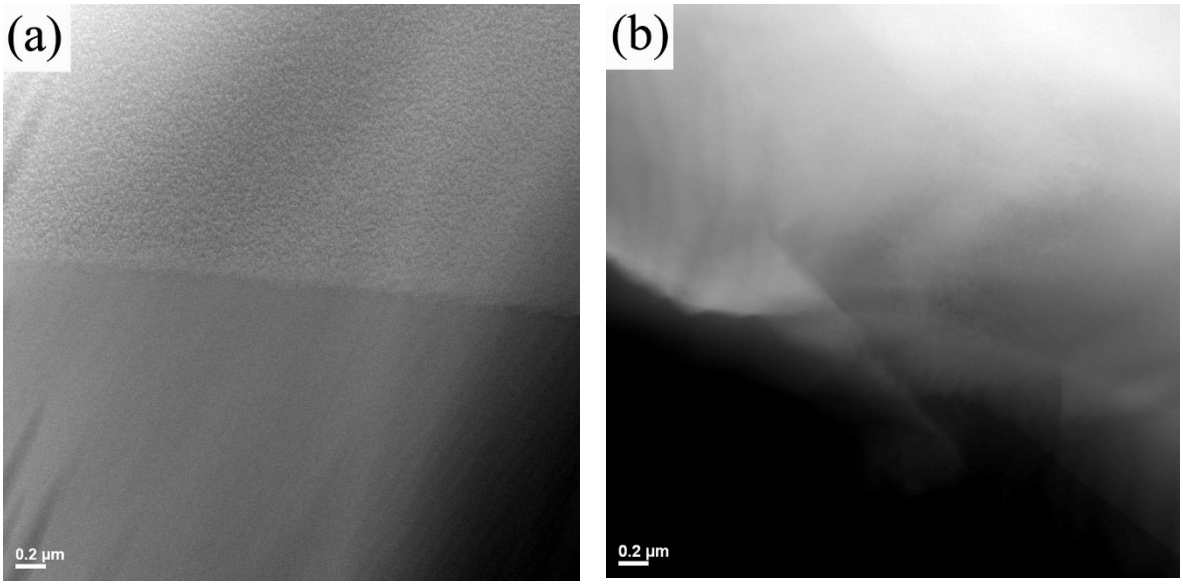

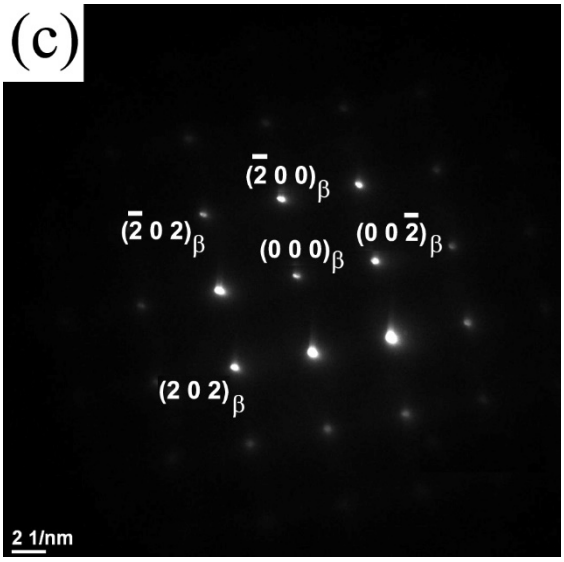

Fig 4.6: FZ TEM image of Ti-15-3 EB welds prepared in the as-welded condition with different welding speeds (a) 500 mm/min, (b) 800 mm/min and (c) diffraction pattern corresponds to 800 mm/min welding speed.

Fig 4.7 shows the optical micrograph of the Ti-15-3 EB weld cross section comparing BM, HAZ and FZ microstructures with a welding speed of 500 mm/min. The HAZ next to the fusion line shows grain growth due to high temperatures at the S/L interface. As the kinetics of grain growth depend strongly on the temperature, the HAZ region experienced significant grain growth because of the peak temperatures experienced during the welding [62]. The average grain size of HAZ is larger (139 ± 15 μm) than BM grain size (78 ± 20 μm). The HAZ region near to the fusion line consists of partially melted equiaxed grains during the melting stage of the welding. The partially melted grains from the HAZ epitaxially grow during the solidification. Lower activation energy needed for heterogeneous nucleation promotes growth in an epitaxial manner. As a result, the crystallographic orientation and structure of grains in the HAZ region at the weld interface continue to grow into a molten weld pool. Along the fusion line, G are steepest due to which grains grow in a columnar fashion perpendicular direction of heat flow from the fusion line and towards the centre of weld zone [102].

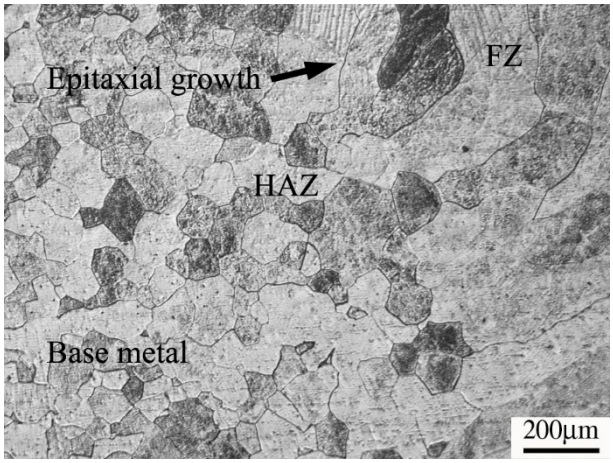

Fig 4.7: Optical microstructure of Ti-15-3 EB weld cross section comparing base metal, HAZ and FZ microstructures with a welding speed of 500 mm/min.

4.4 Microstructure of welds in PWHT condition

The optical microstructure of Ti-15-3 EB welds subjected to PWHT conditions at different welding speeds 500 and 800 mm/min is shown in Fig 4.8(a,b), respectively. The PWHT consists of low-temperature (300°C) soaking for a short time (4 h) followed by high-temperature (500°C) soaking for a longer time (7 h). The response of the welds after aging consists of partial darkening of the surface, making it difficult to observe the microstructure under the light microscope. It was observed that nearly similar microstructural features are present in the FZ of PWHT samples regardless of their welding speeds. The microstructure showed columnar β grains with a dispersion of α phase. However, optical micrographs could not clearly outline the dimensions and morphologies of the α phase because of the nano size of the precipitates [24].

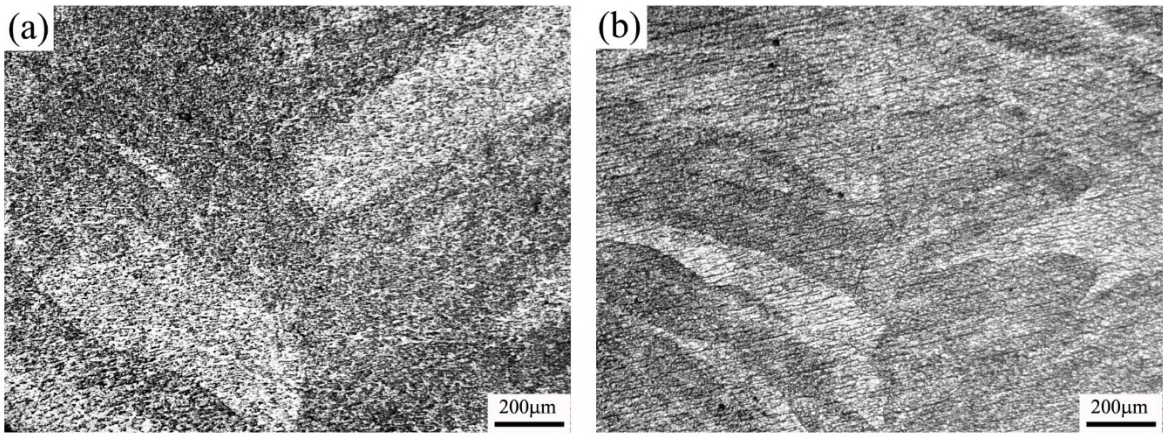

Fig 4.8: Optical micrograph of Ti-15V-3Al-3Cr-3Sn EB welds subjected to PWHT condition at different welding speeds (a) 500 mm/min and (b) 800 mm/min.

Furthermore, the microstructure in Fig 4.9 shows traces of grain boundary α in the HAZ region of the PWHT sample at 500 mm/min welding speed. When subjected to PWHT, the HAZ experiences heating within the α+β region for an adequate duration, resulting in the precipitation of α along the boundaries of the β grains. Similar findings were documented by Balachandar et al.[16].

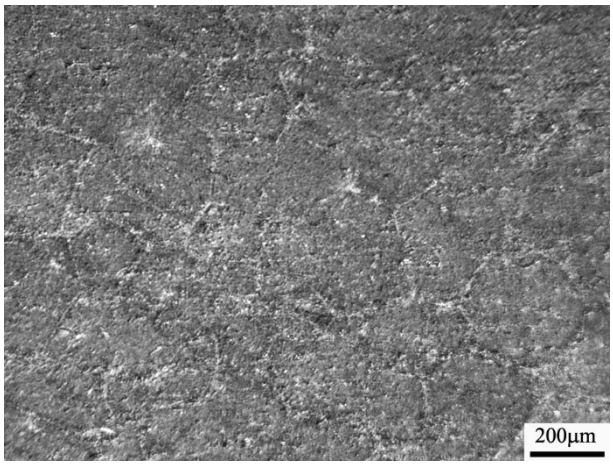

Fig 4.9: HAZ optical micrograph of Ti-15-3 EB welds in the PWHT condition showing the formation of grain boundary α at welding speed 500 mm/min.

When the samples are subjected to low temperatures (1st step) during the PWHT of the welds, the intermediate metastable phase ω phase precipitates in the β matrix, which depends on the value of Molybdenum equivalent (MoE) for a respective beta titanium alloy. The concept of MoE and stability of the β-phase in β-titanium alloys are as follows [46]:

MoE = Mo + 0.67V + 0.28Nb + 0.44W + 1.6Cr + 2.9Fe + 0.22Ta – 1.0Al ------- (4.1)[46]

The elements in the above equation represent respective weight percentages. Generally, the MoE of commercial β-titanium alloys will range between 8 and 24. Depending on this value of MoE, the beta titanium alloys will be distinguished into solute-lean and solute-rich alloys. The alloys with MoE ≤ 12 will come under solute-lean alloys, and greater than Moeq > 12 are referred to as solute-rich alloys. It is to be noted that during low-temperature aging (200˚C - 400˚C), there is a possibility for the formation of intermediate phase's ω or β'. The formation of ω can be seen in the solute-lean Ti-alloys, whereas β' is seen in the solute-rich alloys. In the current study, the MoE for the present alloy, Ti-15V-3Al-3Cr-3Sn is below 12. Hence, in Ti-

15333 the expected intermediate phase is ω [46]. The PWHT after welding promotes two transformation reactions:

i. At the initial step of aging at 300˚C for 4h, β will transform to β + ω. The morphology of ω is in the form of cuboids or ellipsoids, which depends on the alloy composition.

ii. Further, in the second step of aging at 500˚C for 7 h the ω particles act as a precursor for nucleation of fine precipitates of α uniformly distributed in metastable β matrix [46].

The XRD pattern of FZ for EB welds in the PWHT and as-welded conditions at various welding speeds (500, 700, and 800 mm/min) are plotted in Fig 4.10. The peaks in welds in the as-welded condition show a complete β-Ti phase. The PWHT sample exhibited both α and β phases in all the welding speeds, thereby demonstrating the precipitation of the fine α phase after the duplex aging (300 °C for 4 h + 500 °C for 7 h). For the same aging time and temperature, a further increase in the welding speed (800 mm/min) caused a slight increase in the precipitation of α Ti phase in the FZ. It is to be noted that the lower prior β-grain size due to constitutional supercooling at higher welding speeds, promotes more nucleating sites for the formation of α-phase during aging [22].

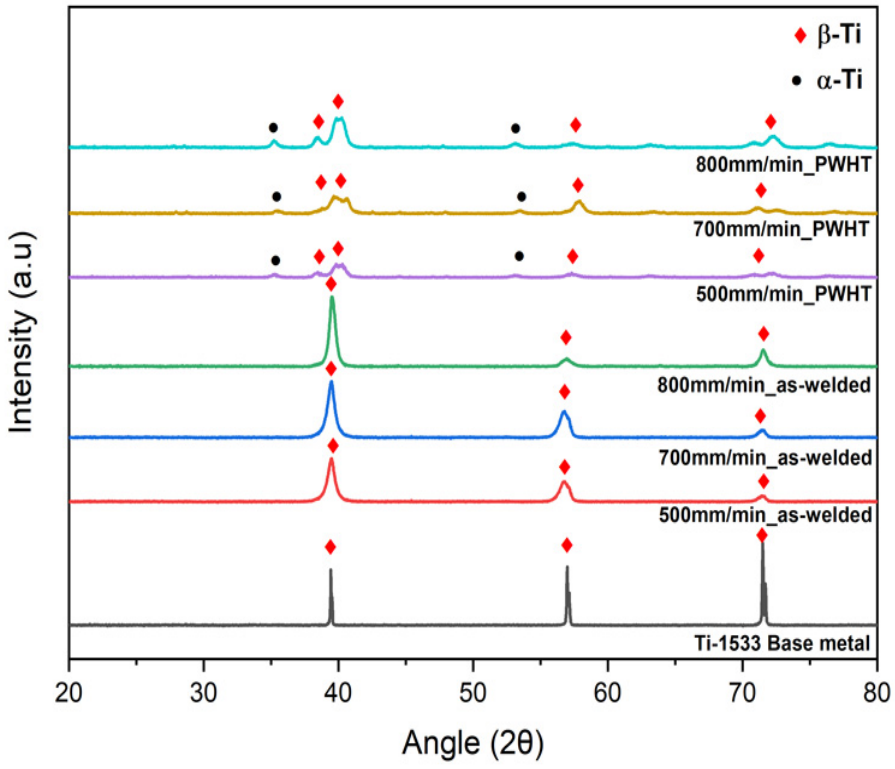

Fig 4.10: Indexed XRD patterns depicting the presence of α-Ti and β-Ti phases in both PWHT and as-welded conditions.

Fig 4.11 shows the TEM image of the Ti-15-3 FZ EB welds prepared with (a) 500 mm/min and (b) 800 mm/min welding speeds. It reveals the uniform distribution of fine α precipitates in the β matrix in both cases, which is evidenced by the XRD analysis (Fig 4.10). It is shown that morphologies of these precipitates are elliptical, thin, long and grown parallel to each other. The average size of α precipitates formed at 500 mm/min (20 ± 5 nm) welding speed is larger than that of 800 mm/min (15 ± 5 nm). Finer precipitates observed after the PWHT of the EB welds prepared with 800 mm/min speed could be attributed to the fine grain structure of the weldment in the as-welded condition. The results are consistent with the observations made by Santhosh et al.[103].

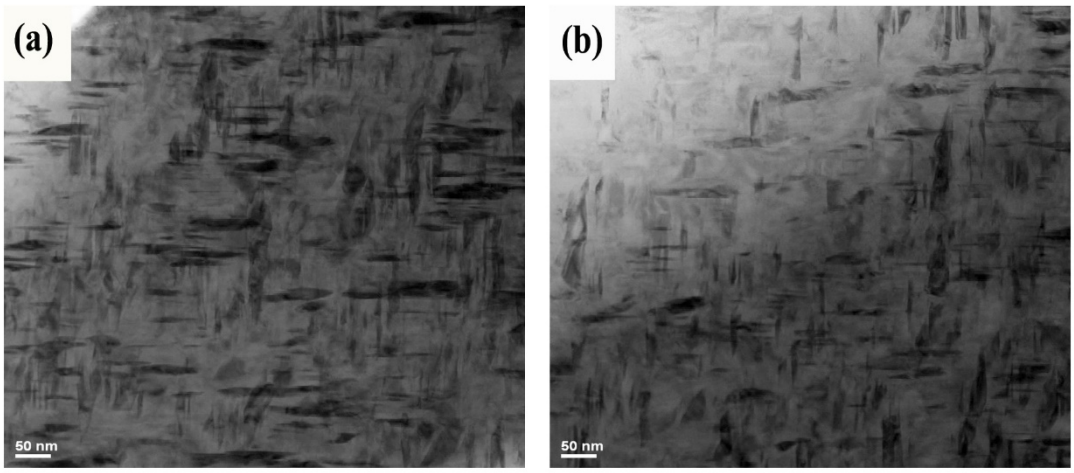

Fig 4.11: FZ TEM image of Ti-15-3 EB welds in the PWHT condition showing α precipitates (black) at welding speeds (a) 500 mm/min and (b) 800 mm/min.

4.5 Mechanical properties

4.5.1 Hardness

Fig 4.12 shows the hardness profile across the weldments in as-welded and PWHT conditions at different welding speeds (500, 700 and 800 mm/min). The hardness of FZ exhibited the lowest hardness (235–245 HV) compared to that of the base metal (~270 HV) in as-welded samples at all welding speeds. This could be due to the presence of coarse columnar β grains in the weld metal. Similar findings were shown by Wang et al.[100]. The welds prepared with 800 mm/min welding speed (low heat input) showed the highest hardness in FZ as compared to that of the 500 and 700 mm/min welding speeds. This increase in the hardness is due to the formation of equiaxed grains at the lower FZ and root and reduction in the β grain sizes, which

in turn are due to higher cooling rates. On the other hand, the lower hardness in the HAZ region compared to that of BM is due to grain coarsening in as-welded conditions of all the welding speeds. As the weld speed increases, the width of HAZ decreases which, in turn, is because of the decrease in the heat input.

The same trend in the hardness plot is seen in the welds subjected to PWHT in all the welding conditions (Fig 4.12). The hardness of weldments in the PWHT condition is higher than that of the weldments in the as-welded condition. The increase in hardness of PWHT samples is due to the precipitation of α particles uniformly distributed across the FZ. Owing to the presence of finer α precipitates in weld metal made at 800 mm/min welding speed subjected to PWHT, they showed higher hardness when compared to that of the other conditions. The increase in hardness of the weld metal after PWHT is reliable with the observations made by Kuroda et al.[29]. It is assumed that the residual stresses on the weldments can be reduced after PWHT samples as that of the as-welded condition. However, the associated decrease in the hardness with a decrease in the residual stresses will be negligible as compared to the increase in hardness due to precipitate strengthening.

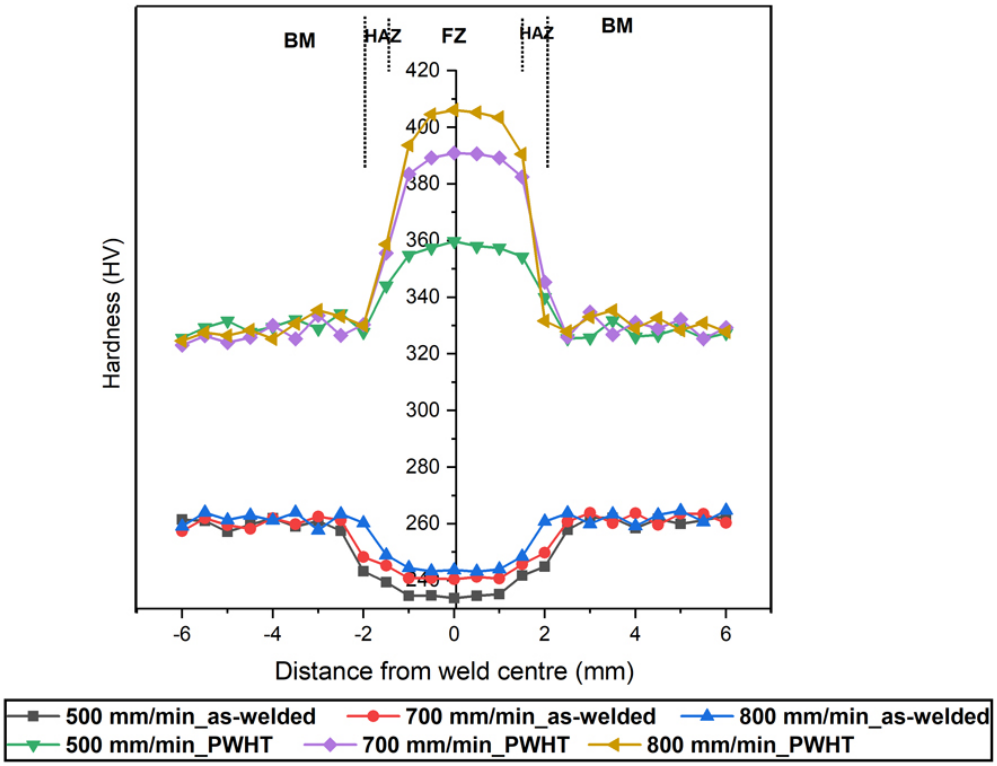

Fig 4.12: Hardness profiles across the EBW Ti-15-3 welds in as-welded and PWHT conditions.

4.5.2 Tensile properties

As the width (2.2–3 mm) of the weld is small in the present welding process, it is difficult to fabricate the longitudinal all-weld samples. Hence, tensile specimens were prepared in the transverse direction of the weld cross-section. It is ensured that the gauge length of the fabricated tensile specimen contains weld zone, HAZ and BM. As the BM exhibits a higher hardness compared to that of the weld metal, the deformation will be more in the weld zone, and failure will occur in the weld zone. The observed elongation based on the gauge length of the specimen indicates the overall ductility but will not represent the weld portion alone. It is to be noted that most of the analysis reported the weld metal ductility in the transverse cross-section of the sample. Fig 4.13 shows the typical stress–strain curves for Ti-15-3 base metal and electron beam welded joints prepared with different welding speeds (500, 700 and 800 mm/min) of as-welded and PWHT conditions. The results of the tensile testing of the as-welded and PWHT samples are listed in Table 4.1. The weldments prepared with 500 mm/min welding speed (high heat input) exhibit the lowest strength and elongation values (YS: 661 ± 4 MPa, UTS: 676 ± 5 MPa, %El: 11 ± 0.5) compared with 700 mm/min (YS: 709 ± 4 MPa, UTS: 724 ± 6 MPa, %El: 12 ± 0.4) and 800 mm/min welding speeds (YS: 735 ± 6 MPa, UTS: 752 ± 5 MPa, %El: 13 ± 0.5) in the as-welded condition, and this may be attributed to coarser columnar beta grains present in the FZ. In contrast, the higher strength exhibited in 800 mm/min welding speed is due to fine equiaxed β grains formation at the weld center and root and a decrease in β columnar grain size in FZ. However, all the welding speeds in the as-welded condition exhibit lower strength and ductility than base metal (YS: 776 ± 5 MPa, UTS: 793 ± 5 MPa, %El: 17 ± 0.6). The BM's high strength can be attributed to its microstructure characterized by fine equiaxed grains. These findings align with those presented in the research on GTAW of Ti-15-3 welds conducted by Balachandar et al.[16].

The tensile and yield strength of the weldments after the PWHT are higher than those in as-welded conditions. The precipitation of α phase in β matrix can be the contributory factor for the increase in strength due to PWHT. The two-step aging will result the formation of ω phase in the first step of aging at 300 °C, and the formed ω phase acts as a nucleating site for the formation of α precipitates. The weldments prepared with 800 mm/min welding speed exhibit higher strength (YS: 1335 ± 5 MPa, UTS: 1356 ± 6 MPa, %El: 7 ± 0.5) compared to that of 500 mm/min (YS: 1205 ± 5 MPa, UTS: 1216 ± 4 MPa, %El: 5 ± 0.3) and 700 mm/min (YS: 1282 ± 4 MPa, UTS: 1293 ± 5 MPa, %El: 6 ± 0.5) in PWHT condition. This is attributed to a decrease in the average size of α precipitates in β matrix at higher welding speeds as compared to the lower welding speeds.

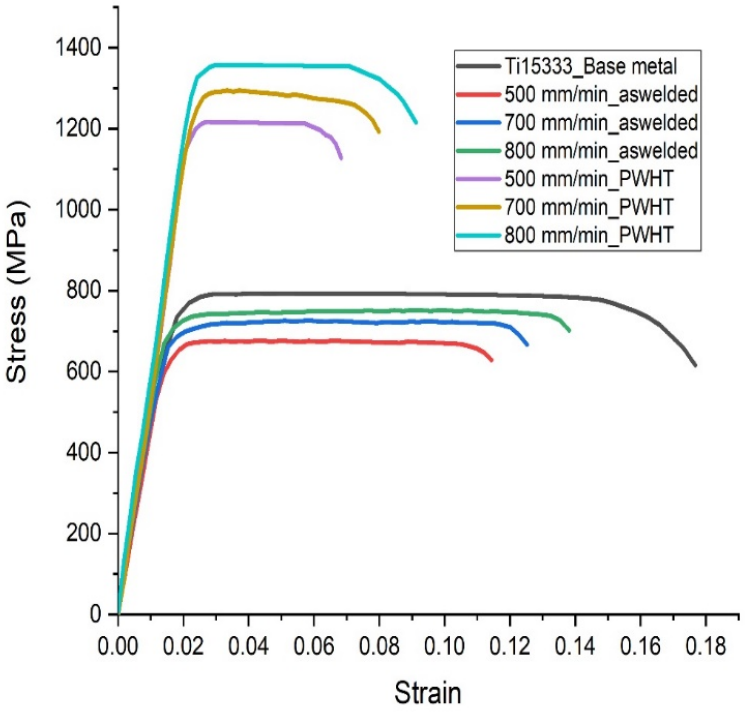

Fig 4.13: Strain-strain curves for the prepared EB Ti-15-3 joints in as-welded and PWHT conditions compared with the base metal.

Table 4.1: Variation in tensile properties of as-welded and PWHT EBW Ti-15-3 samples in comparison with BM at different welding speeds (500 mm/min, 700 mm/min and 800 mm/min)

Condition	**Yield Strength (YS), MPa**	**Ultimate Tensile Strength (UTS), MPa**	**Elongation (El %)**
Base metal	776 ± 5	793 ± 5	17 ± 0.6
500 mm/min (as-welded)	661 ± 4	676 ± 5	11 ± 0.5
700 mm/min (as-welded)	709 ± 4	724 ± 6	12 ± 0.4
800 mm/min (as-welded)	735 ± 6	752 ± 5	13 ± 0.5
500 mm/min (PWHT)	1205 ± 5	1216 ± 4	5 ± 0.3
700 mm/min (PWHT)	1282 ± 4	1293 ± 5	6 ± 0.5
800 mm/min (PWHT)	1335 ± 5	1356 ± 6	7 ± 0.5

The cooling rates and heat input play a significant role in deciding the fracture location in tensile samples. Fig 4.14(a–d) shows the fractured tensile specimens in as-welded samples and PWHT conditions. All as-welded specimens, irrespective of welding speeds, failed in FZ. As an example, Fig 4.14(a, b) displayed the failure location of tensile specimens in the as-welded samples at 500 mm/min and 800 mm/min welding speeds. In both conditions, the samples failed in the FZ, as indicated by arrows. However, the PWHT fractured tensile specimens at the same welding speeds (500 mm/min and 800 mm/min) failed in the BM, as marked in Fig 4.14(c, d). This is because of higher tensile strength and hardness in FZ of weldments after PWHT as compared with BM. Fig 4.15 shows the fractured surfaces of the EBW Ti-15-3 joint at 800 mm/min welding speed in the as-welded condition, revealing the regions of larger dimples with some river marks (Fig 4.15a), while the PWHT condition exhibits a fine dimple (Fig 4.15b). During aging, the β-α transformation occurs, and the dwell period (7 h) is utilized for the α phase precipitation. The resulting two-phase zones are composed of a transformed, hard hexagonal fine α-phase along the prior-β grain boundaries and within the β grains. This transformed α reinforces the soft β grains in FZ of all PWHT samples. During tensile tests, the transformed α and β matrix interfaces are more prone to fracture. As a result, possible necking instability and fracture occur near the end of the HAZ adjacent to relatively soft parent material in PWHT samples [16].

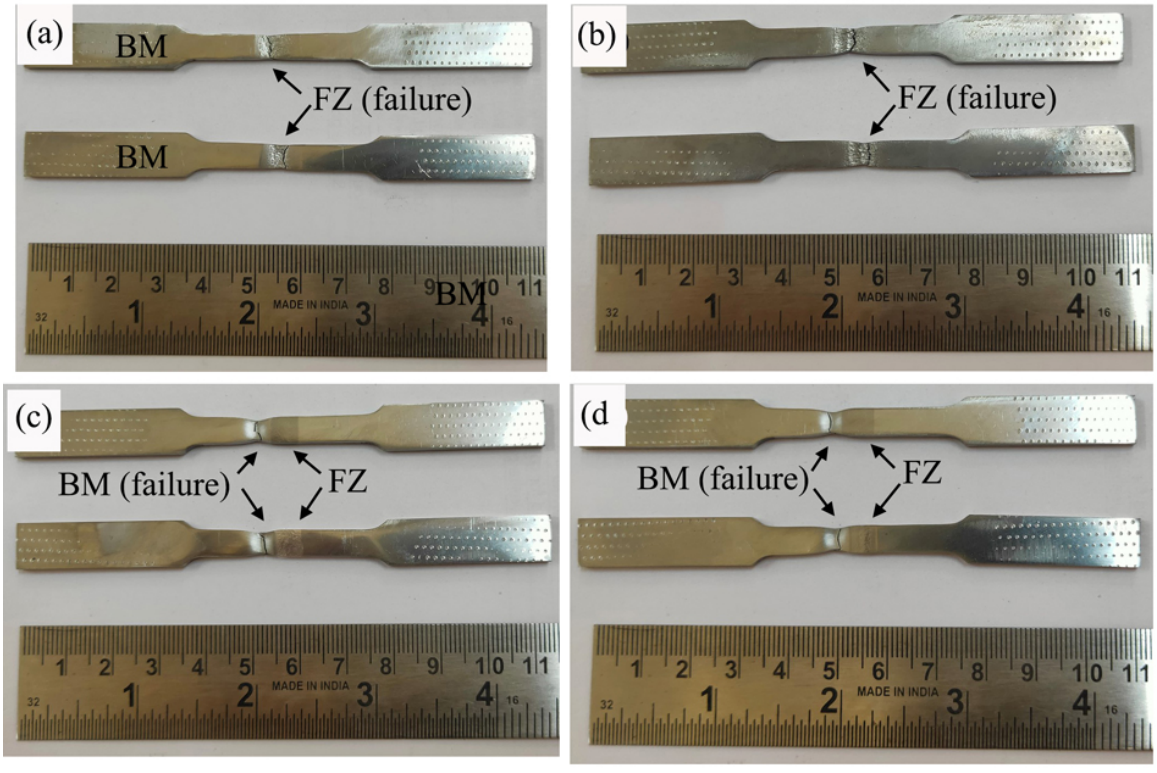

Fig 4.14: The Failure location of EBW Ti-15-3 welds at 500 mm/min and 800 mm/min welding speed in the (a, b) as-welded and (c, d) PWHT conditions.

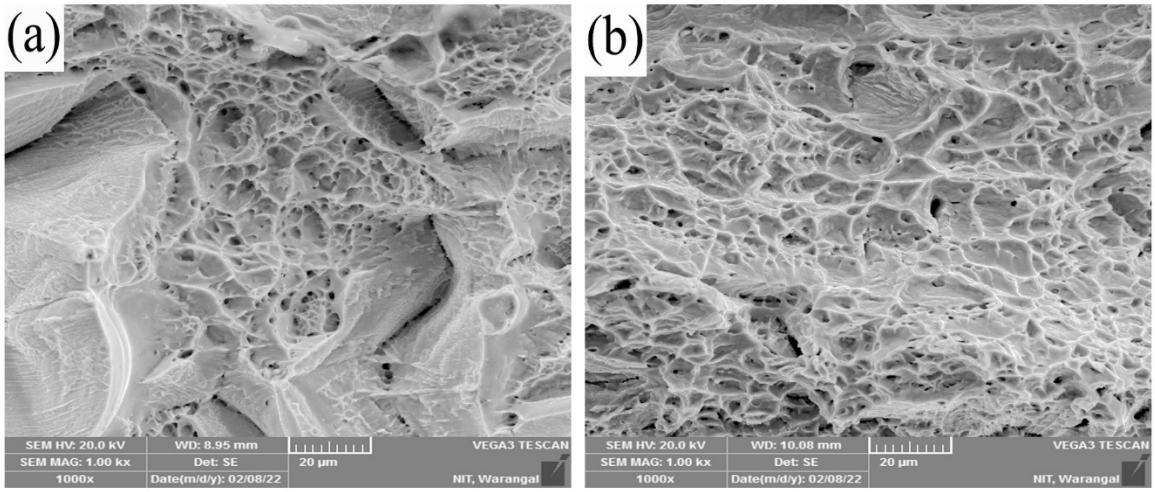

Fig 4.15: Fracture surfaces of the EBW Ti-15-3 joints at 800 mm/min welding speed in the (a) as-welded and (b) PWHT conditions.

5. RESULTS AND DISCUSSION-II

Effect of welding speed and post-weld heat treatment on microstructural characterization and mechanical properties of gas tungsten arc welded Ti-15-3 joints

5.1 Macrostructure of welds in the as-welded condition:

Macrostructures for Ti-15-3 welds using three different welding speeds (15 cm/min, 20 cm/min, and 25 cm/min) are compared in Fig 5.1. The welds were characterized by complete penetration, and butt joints were achieved by the GTAW process. The calculated values of average bead width in each welding speed at 15 cm/min, 20 cm/min, and 25 cm/min corresponds to ~9.8 mm, 7.7 mm, and 6.5 mm, respectively. It seems that the decrease in average bead width with an increase in welding speed. This is attributed to a reduction in the heat input as welding speed increases which results in fast cooling rates. In addition, the welds at higher welding speeds (20 cm/min and 25 cm/min) appear to have a relatively deep penetration compared with the low welding speed (15 cm/min). This may be caused by lower heat sinks at higher welding speeds compared to low welding speeds. The top portion in FZ of all the welds exhibits large columnar grains, and the bottom portion of the same welds reveals the equiaxed grains. This is due to lower G at the top, resulting in grains growing in columnar mode, while at the bottom part, the G is high, leading to a higher cooling rate, resulting in equiaxed grains. It is also observed that all the welds showed coarse equiaxed grains in HAZ and fine equiaxed grains in BM. This variation in microstructure across the weld can be linked to the thermal cycles experienced during welding. In FZ, the welds at higher weld speed displayed a smaller grain size of columnar grains while lower welding speed exhibited an increase in the size of columnar grains. However, the equiaxed grains at the bottom of each weld also show a similar trend. These columnar grains grow epitaxially in the direction perpendicular to the fusion boundary, as the thermal gradients are more prominent near the fusion boundary, the unmelted BM grains near the fusion boundary act as a substrate for nucleation for the epitaxial growth. Generally, weld metal solidification occurs in a columnar mode where grains grow epitaxially from the fusion line towards the center due to a sharp G at the fusion boundary. In contrast, as the bottom portion of the weld zone approaches, the G becomes lower, and the R will be higher, resulting in a constitutional supercooling zone ahead

of the S/L interface, which gives rise to the formation of equiaxed grains at the welded bottom. Therefore each welding speed results in lower peak temperatures in the bottom portion of the weldment compared to the top region. This results in faster cooling rates and lowers G in the bottom part of the weld zone resulting in CET. In other words, welds with higher welding speed lead to faster cooling rates resulting in low heat input and greater constitutional supercooling; hence more nuclei will survive, resulting in a higher amount of fine equaixed grains in the bottom part of the weld.

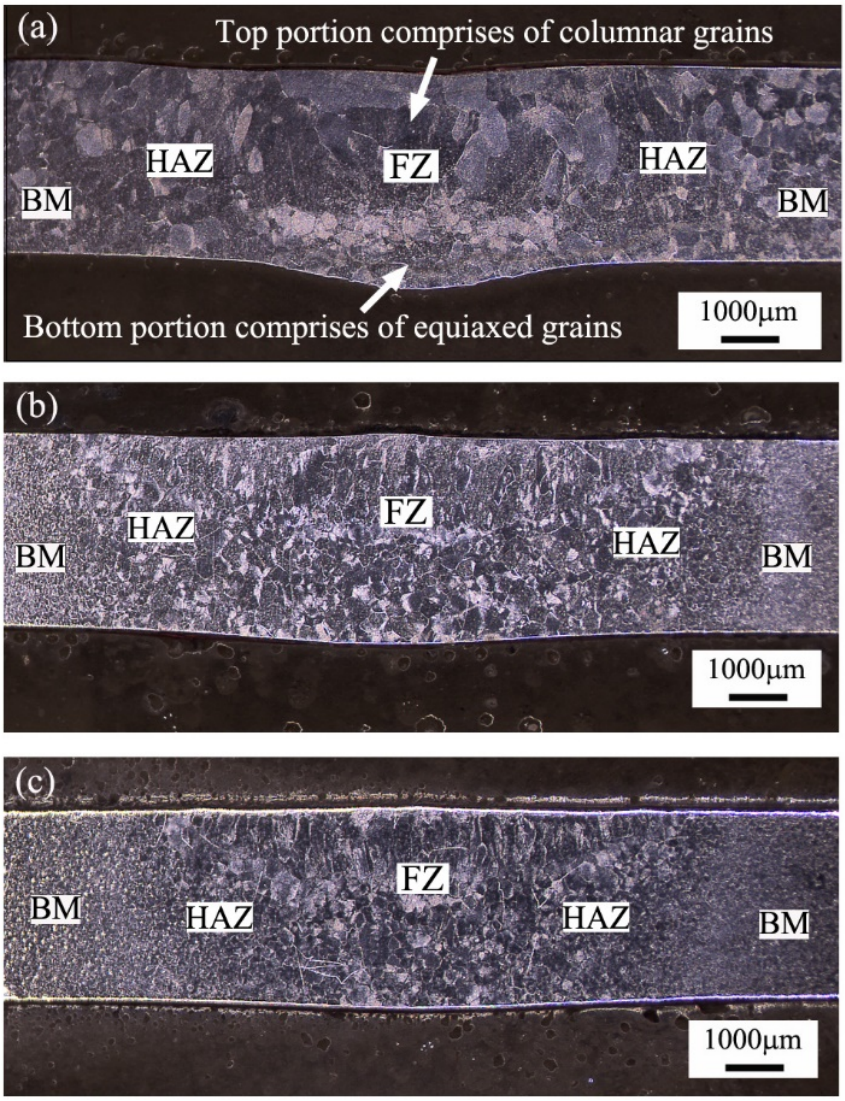

Fig 5.1: Macrostructure of the cross-section of GTA welds prepared in as-welded condition with different welding speeds (a) 15 cm/min (b) 20 cm/min and (c) 25 cm/min.

5.2 Microstructure of welds in the as-welded condition:

Fig 5.2 shows the optical microstructures of as-welded Ti-15-3 welds at different welding speeds. In all the conditions, solidification takes place in epitaxial manner in the form of coarse β grains from the fusion line towards the center of the weld. It is observed that the width of columnar β grain decreases as the welding speed increases. It is well known that cooling rates are inversely proportional to weld heat input. Therefore at lower cooling rates, the solidification rate and growth rate of grains tend to be low. So, at lower welding speeds, as the cooling rates are slow, the mode of solidification changes from equiaxed to columnar. In other words, relatively lower heat inputs in case of higher welding speed decrease the width of columnar grains could be due to faster cooling rates. It is to be noted that the aspect ratio (length/width ratio) of columnar grains in FZ is highest for welds made at 25 cm/min and lowest at 15 cm/min welding speed. The grain size measurement in the welds prepared using welding speeds of 15 cm/min, 20 mm/min and 25 mm/min showed average grain diameters of ~398 μm, 278 μm, and 209 μm, respectively, and grain aspect ratio ranges from 3 to 7.

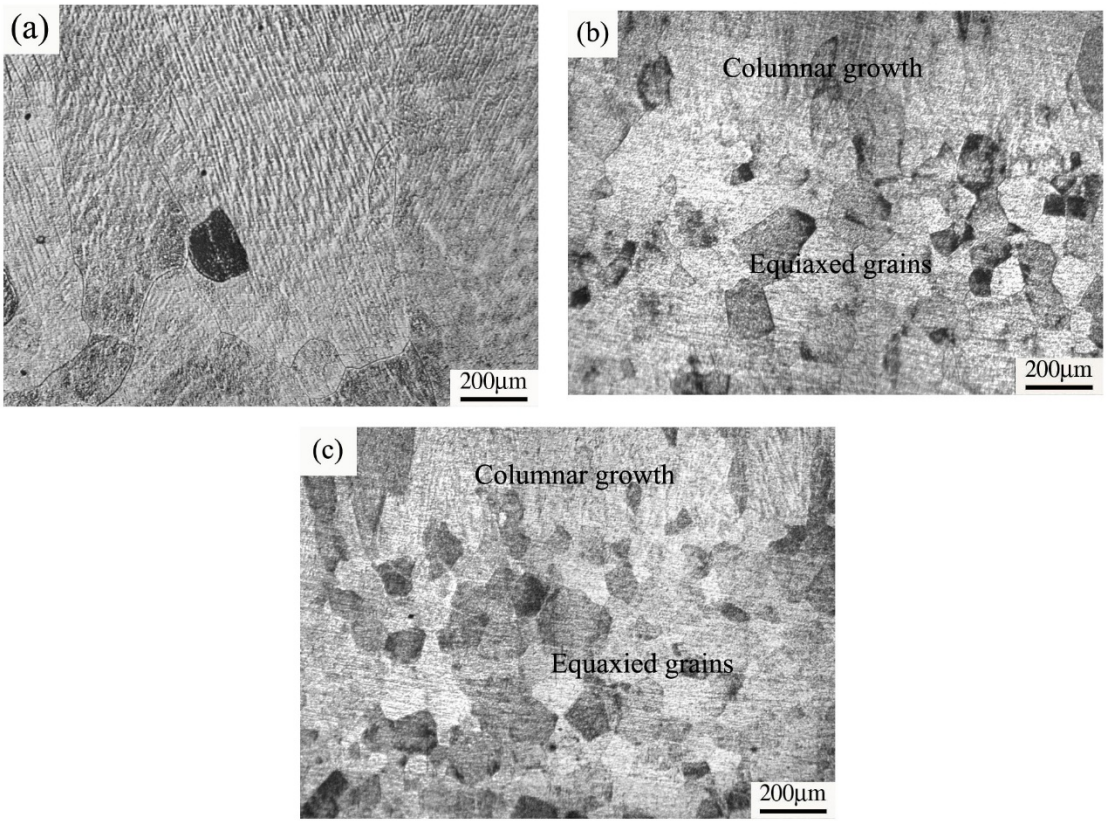

Fig 5.2: Optical micrographs of as-welded GTA welds at different welding speeds (a) 15 cm/min (b) 20 cm/min and (c) 25 cm/min

Fig 5.3(a, b) shows the FZ TEM image of Ti-15-3 GTA welds made with different welding speeds (a) 15 mm/min and (b) 25 mm/min, respectively. The micrographs show the large extent

of the beta phase in the FZ in both conditions. The faster weld cooling rates in FZ during welding and the high amount of β stabilizing elements in the BM have resulted in the β phase at room temperature in the as-welded condition. Lutfi et al. [82] have also found similar observations in most areas of FZ in GTA weldments.

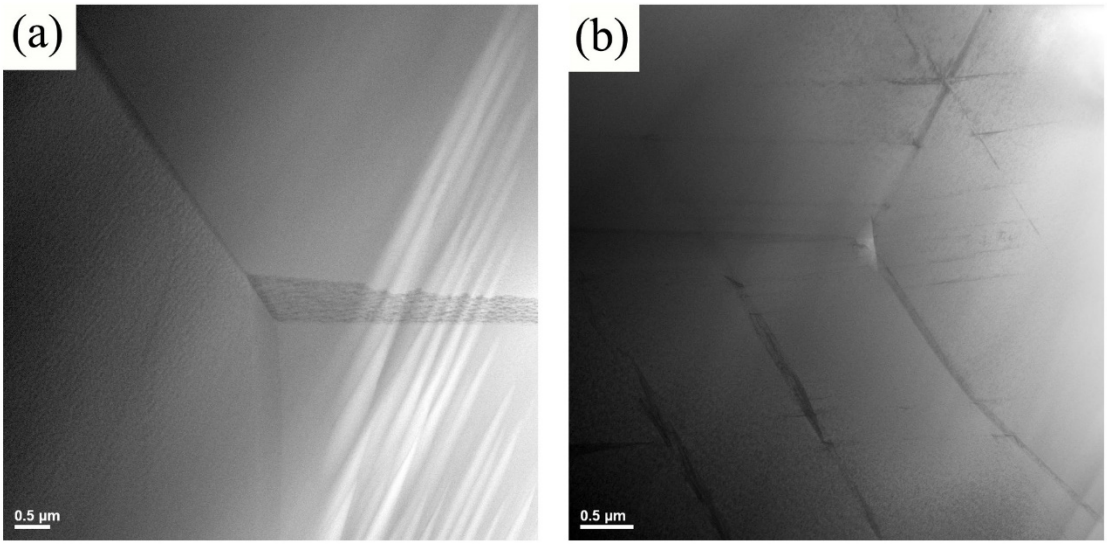

Fig 5.3: Fusion zone TEM image of Ti-15-3 GTA welds prepared in PWHT condition with different welding speeds: (a) 15 cm/min and (b) 25 cm/min.

5.3 Microstructure of welds in PWHT aging condition:

In this study, the Ti-15-3 welds are subjected to a two-step aging heat treatment process. Fig 5.4 (a, b) shows the optical microstructure of Ti-15-3 GTA welds subjected to PWHT conditions at different welding speeds 15 cm/min and 25 cm/min, respectively. The PWHT promotes the α precipitation in β matrix in all the regions of the welds. However the response of the welds after aging consists of partial darkening of the surface, making it challenging to observe the microstructure under the light microscope. However, optical micrographs could not clearly outline the dimensions and morphologies of the α phase because of the nano size of the precipitates. It is observed that nearly similar microstructural features are present in the FZ of PWHT samples regardless of their welding speeds. Similar conclusions were reported by Balachandar et al.[16].

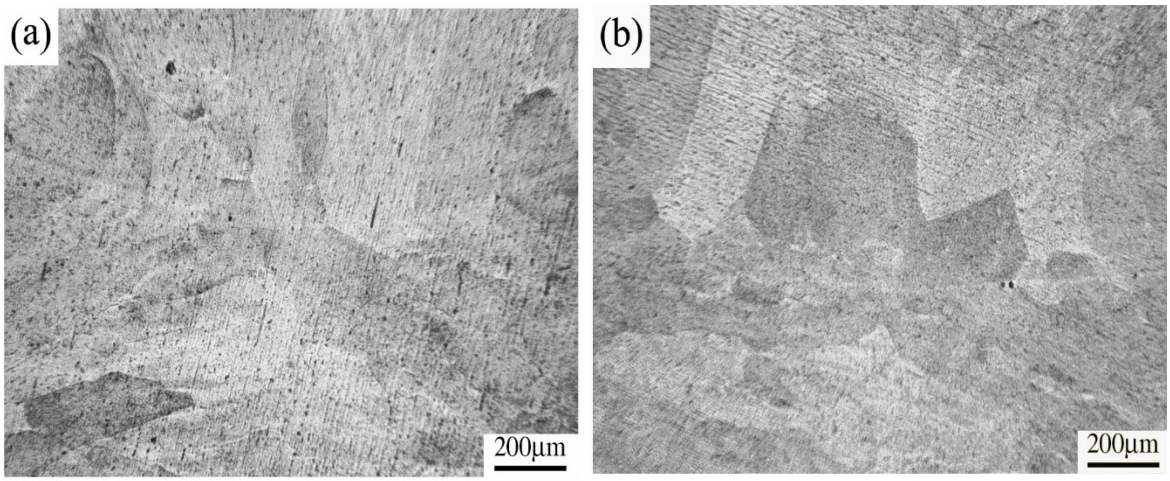

Fig 5.4: Optical micrograph of Ti-1533 GTA welds subjected to PWHT condition at different welding speeds: (a) 15 cm/min and (b) 25 cm/min.

Fig 5.5 shows the XRD pattern of FZ for GTA welds in as-welded and PWHT conditions at various welding speeds (15 cm/min, 20 cm/min, and 25 cm/min). Peaks in as-welded welds show a complete β-Ti phase. The PWHT sample showed both phases at all welding speeds, demonstrating phase precipitation after duplex aging (300 C for 4 h + 500 C for 7 h). A slight increase in the welding speed (25 cm/min) caused a slight increase in the precipitation of the Ti phase in the FZ for the same aging time and temperature. The reduction in β-grain size caused by constitutional supercooling at higher welding speeds promotes the formation of more nucleating sites for the formation of α-phase during aging.

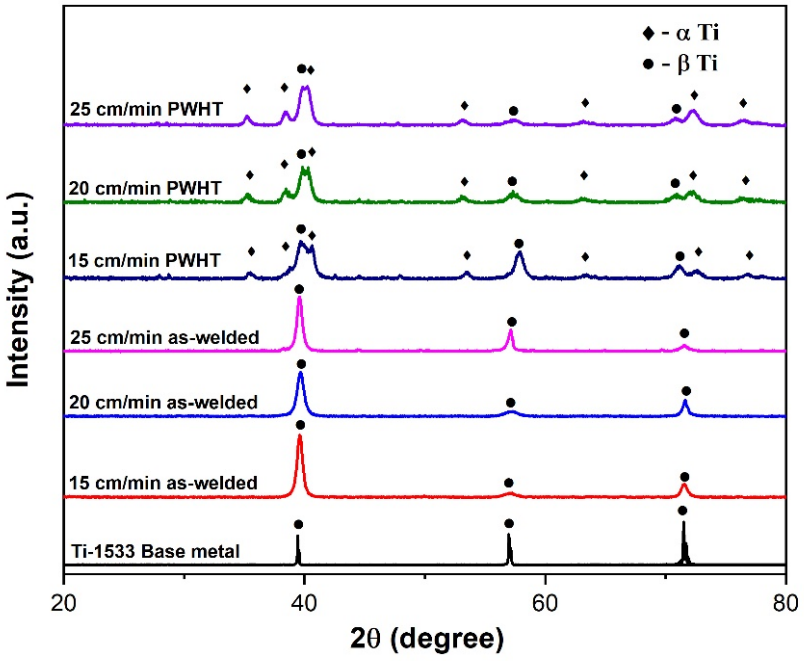

Fig 5.5: Indexed XRD patterns depicting the presence of α-Ti and β-Ti phases in both PWHT and as-welded conditions.

Fig 5.6 shows the TEM images of the Ti-15-3 FZ GTA welds prepared with (a) 15 cm/min and (b) 25 cm/min welding speeds. It reveals the uniform distribution of α precipitates in the β matrix in both cases, which is evidenced by the XRD analysis (Fig 5.5). It is shown that morphologies of these precipitates are elliptical and thin dispersred in the β matrix. The average size of α precipitates formed at 25 cm/min (38 ± 5 nm) welding speed is larger than that of 15 cm/min (16 ± 5 nm). The lower welding speed (15 mm/min) after aging resulted in the formation of a lower density of α precipitates in the β grains due to the less availability of metastable β phase. In contrast, the higher welding speed (25 mm/min) resulted in the formation of a higher density of α precipitates due to more volume fraction of metastable β phase due to higher cooling rates. The results are consistent with the observations made by Santhosh et al.[46].

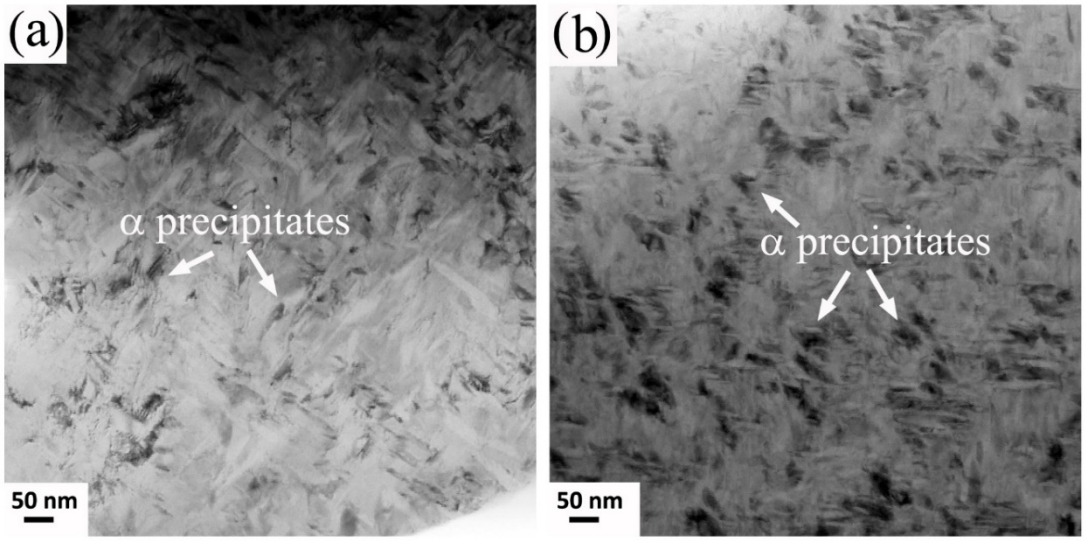

Fig 5.6: TEM image of Ti-15-3 PWHT GTA welds in FZ showing α precipitates at welding speeds (a) 15 cm/min and (b) 25 cm/min

5.4 Mechanical properties

5.4.1 Hardness

Transverse hardness measurements of the welds in as-welded and PWHT conditions at three welding speeds are shown in Fig 5.7. Hardness profiles of GTAW welds showed a decrease in the hardness from BM through the HAZ to the FZ in as-welded samples at all welding speeds.

The average hardness of FZ of as-welded joints decreased with decreasing the welding speed. The welds prepared using 15 cm/min welding speed exhibited the lowest hardness in FZ (225 ± 2 HV) compared to that of the BM (~270 HV) in the as-welded condition. This could be attributed to the presence of coarse columnar β grains and large equiaxed grains in the weld zone. Similar observations were shown by Wang et al.[104]. The welds prepared with 25 cm/min welding speed (low heat input) showed the highest hardness in FZ as compared to that of the other welding speeds. This increase in the hardness is due to the formation of more equiaxed grains at the bottom part and a reduction in the β grain size in FZ. On the other hand, the lower hardness in the HAZ region compared to that of BM is due to coarse equiaxed grains in as-welded conditions of all the welding speeds. As the weld speed increases, the width of HAZ decreases which in turn decreases the heat input. A same trend in the hardness plot is seen in the welds subjected to PWHT in all the welding conditions (Fig 5.7). The hardness of weldments in the PWHT condition is found to be greater than that of weldments in the as-welded condition. The precipitation of α particles uniformly distributed across the FZ causes the increase in hardness of PWHT samples. Because of the presence of finer α precipitates in weld metal made at 25 mm/min welding speed, it had a higher hardness than the other conditions. It was suggested that the faster cooling rates during weld solidification would result in a larger concentration of excess vacancies in the FZ [105]. At faster cooling rates (i.e; higher welding speeds), a decrease in the grain size of the FZ was observed which would also decrease the intensity of the solute segregation. Hence, finer and uniformly distributed precipitation can be expected in the FZ of the welds prepared with higher welding speeds (25 cm/min) because of the lower segregation and higher diffusion rate during the PWHT. TEM micrographs in Fig 5.6 also shows finer alpha precipitates in the welds prepared with 25 cm/min. The increase in weld metal hardness after PWHT is consistent with the findings of Kuroda et al.[29] The residual stresses on the weldments are assumed to be reduced after PWHT samples as compared to the as-welded condition. The BM showed the equaixed grains in the as-welded condition which resulted in higher hardness than FZ which is composed of coarse columnar prior β grains. During the PWHT, the formation of the strengthening precipitates results in the increase in the hardness for both BM and FZ compared to the as-welded condition. However, GTA welding causes the weld fusion zone to experience severe thermal cycles which would result in the development of the residual stresses and dislocations network. The presence of residual stresses, vacancies and lattice defects might aid in finer and uniform precipitation of alpha particles in the FZ compared to the BM during the PWHT [75]. However, the associated

decrease in the hardness with a reduction of the residual stresses will be negligible compared to the increase in hardness due to precipitate strengthening.

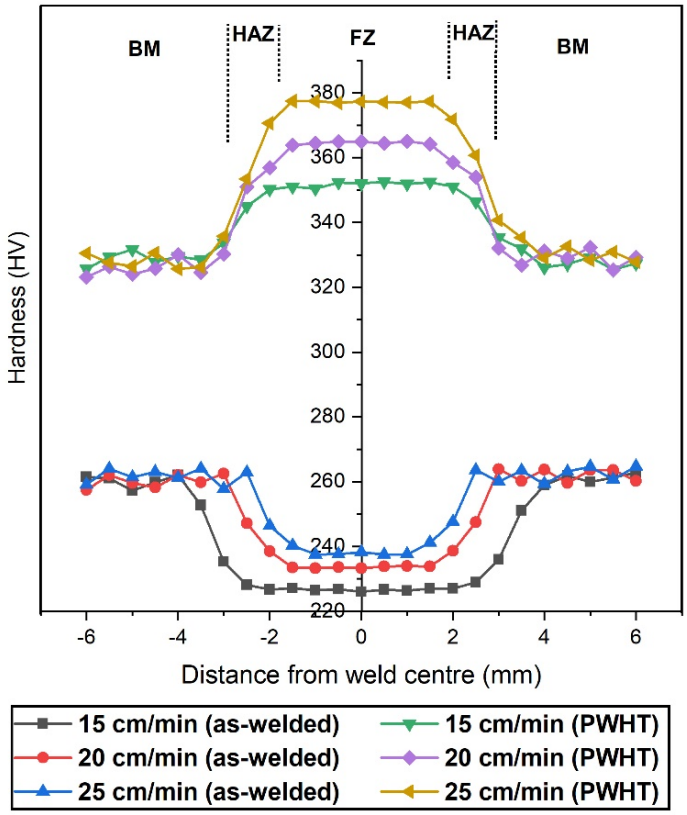

Fig. 5.7: Hardness profiles across the GTAW Ti-15-3 weld in as-welded and PWHT condition

5.4.2 Tensile properties

Results of tensile tests of GTA welded joints prepared with different welding speeds (15 cm/min, 20 cm/min, and 25 cm/min) in as-welded and PWHT conditions are compared in Table 5.1. The tensile properties of the base material (BM) have been included in the table for comparative analysis. The BM displayed greater strength and ductility in contrast to the as-welded GTA welds, a result attributed to the presence of fine grains. It may be seen from the graph shown in Fig 5.8 that the GTA weldments prepared with 25 cm/min welding speed displayed higher strength and ductility compared with other welds in the as-welded condition, and this may be attributed to a reduction in columnar beta grain size and formation of more number of equiaxed grains in the FZ. However, the welds at lower welding speeds showed lower strength and ductility due to coarse equiaxed β grains formation and increased β columnar grain size in FZ. However, all the welding speeds in the as-welded condition exhibit lower strength and ductility than cold-worked BM. These results are reliable with those

reported in GTAW of Ti-15-3 welds by Balachandar et al.[16] The tensile and yield strength of the weldments after the PWHT is higher than those in as-welded conditions, as evidenced by the graph shown in Fig 5.8. The precipitation of the α phase throughout the β matrix could be the factor for the increase in the strength of PWHT samples. The two-step aging results in the formation of ω phase in the first step of aging at 300˚C, and the formed ω phase acts as a nucleating site for the formation of α precipitates. The weldments prepared with 25 cm/min welding speed exhibit higher strength and elongation in relation to that of 20 cm/min and 15 cm/min in PWHT condition. This is attributed to a high density of α precipitates in β matrix at higher welding speeds as compared to the lower welding speeds.

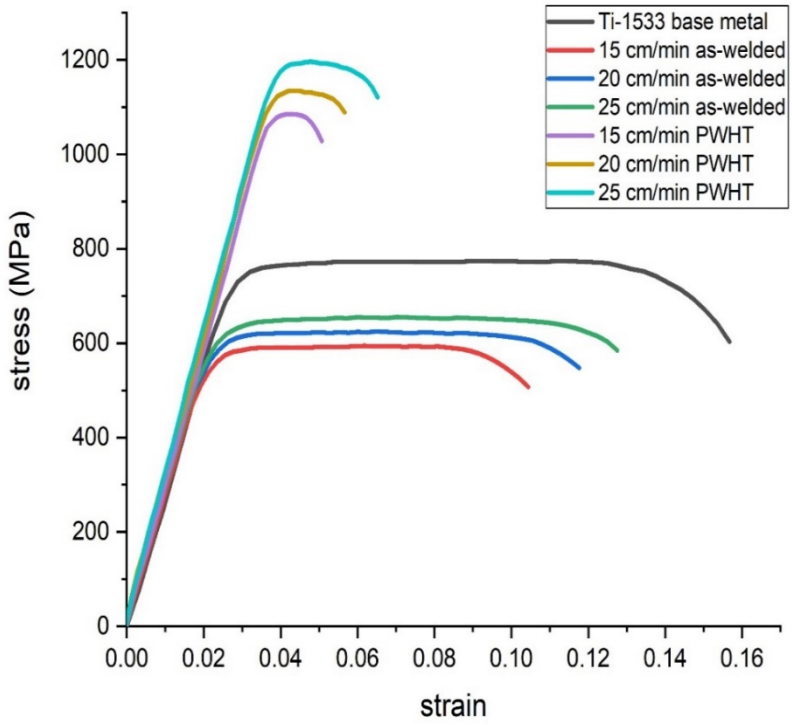

Fig 5.8: Strain-strain curves for the prepared GTAW Ti-15-3 joints in as-welded and PWHT conditions compared with the BM.

Table 5.1: Variation in tensile properties of as-welded and PWHT GTA welded Ti-15-3 samples in comparison with BM at different welding speeds (15 cm/min, 20 cm/min, and 25 cm/min)

Condition	**Yield Strength (YS), MPa**	**Ultimate Tensile Strength (UTS), MPa**	**Elongation (El %)**
Ti-15-3 Base metal	757 ± 4	774 ± 5	15 ± 0.5
15 cm/min as-welded	581 ± 4	593 ± 5	10 ± 0.5
20 cm/min as-welded	609 ± 4	624 ± 4	11 ± 0.4

25 cm/min as-welded	632 ± 6	654 ± 5	12 ± 0.5
15 cm/min PWHT	1064 ± 7	1085 ± 4	5 ± 0.4
20 cm/min PWHT	1125 ± 7	1134 ± 8	5 ± 0.5
25 cm/min PWHT	1181 ± 4	1196 ± 8	6 ± 0.5

In welded samples, cooling rates, and heat input play an essential role in determining fracture location. Fig 5.9(a-d) depicts fractured tensile specimens in as-welded and PWHT conditions. In FZ, all as-welded specimens failed, regardless of welding speed. For instance, Fig 5.9(a, b) shows the failure location of tensile specimens in as-welded samples at 15 cm/min and 25 cm/min welding speeds. The samples failed in the FZ in both conditions, as indicated by the arrows. However, the PWHT fractured tensile specimens failed in the BM at the same welding speeds, as shown in Fig 5.9(c, d). This is due to the higher tensile strength and hardness in the FZ of weldments after PWHT compared to BM. The fractured surfaces of GTAW Ti-15-3 as-welded joint at 25 cm/min welding speed showed larger dimples with some river marks as shown in Fig 5.10a, while the PWHT condition shows fine dimples, as displayed in Fig 5.10b. Similar features have been observed in as-received BM fracture as shown in Fig 5.10c. During the aging of Ti-15-3, the formation of a hard hexagonal α-phase reinforces the soft β phase in FZ, resulting in increased hardness and strength of FZ. As a result, possible necking instability and fracture occur at the end of the HAZ near the relatively soft parent material in the PWHT samples of Ti-15-3 welds. These results are consistent with the studies made by Becker et al.[97].

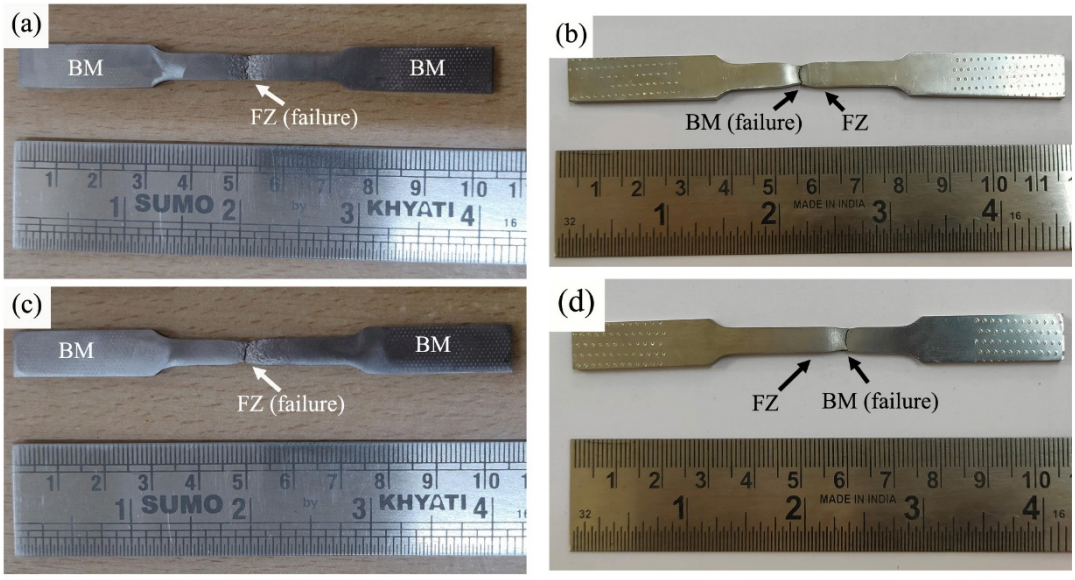

Fig 5.9: Failure location of GTAW Ti-15-3 welds at 15 and 25 cm/min welding speed in (a) and (b) as-welded and (c) and (d) PWHT condition.

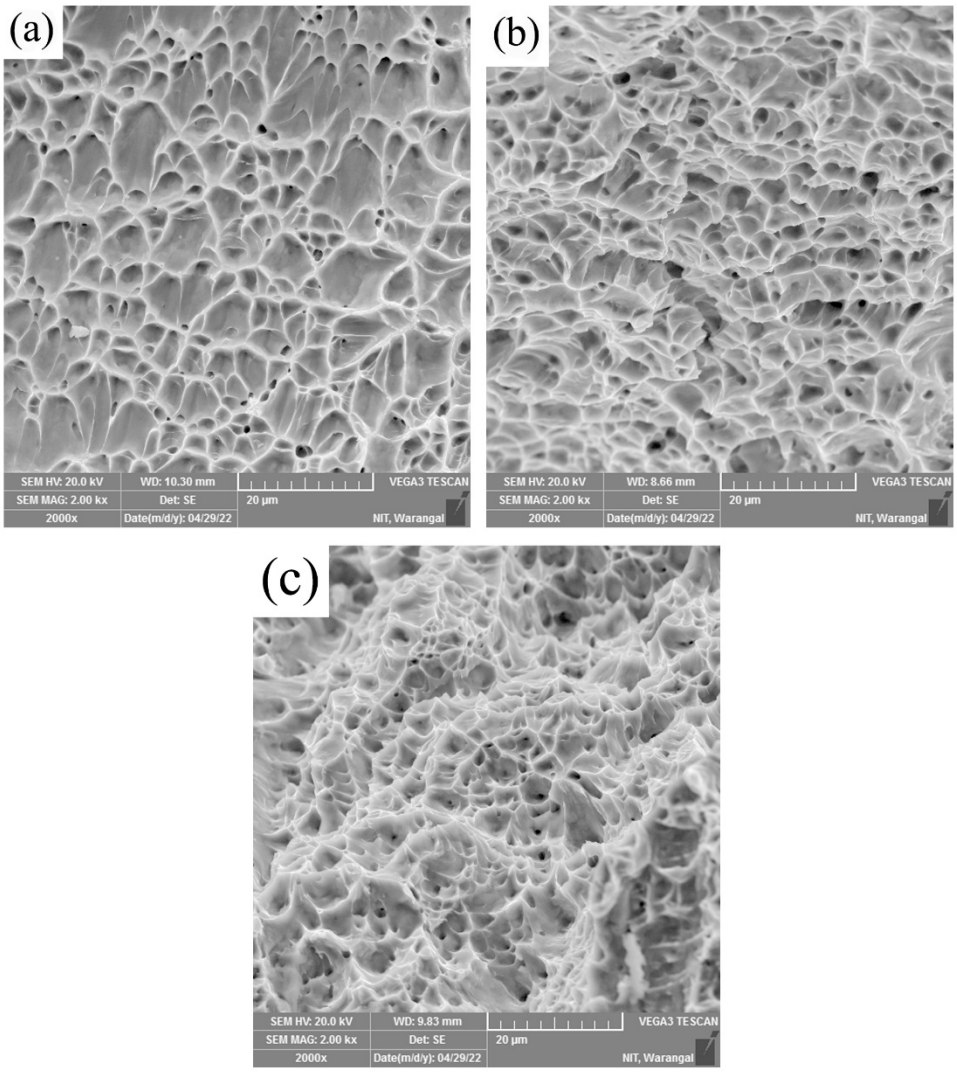

Fig 5.10: Fracture surfaces of the GTAW Ti-15-3 joints at 25 cm/min welding speed in (a) as-welded condition, (b) PWHT condition, and (c) as-received BM.

6. RESULTS AND DISCUSSION-III

Achieving grain refinement in gas tungsten arc welded Ti-15-3 joints by Ni and Si-modified fillers

6.1 Weld macrostructure in as-welded condition:

Fig 6.1a shows the macrostructure of the weld cross-section for Ti-15-3 autogenous weld. It can be observed that the weld had complete penetration and was free from defects. The weld cross-section can be distinguishable into FZ, HAZ, and BM. The solidification begins epitaxially from the HAZ grains next to the fusion boundary and tends to grow towards the weld center in a columnar structure. This columnar growth of the grains in the weld is due to the steep thermal gradients at the fusion boundary. Also, HAZ revealed a significant grain coarsening as compared to the BM. This coarsening of grains in HAZ is due to the slow heat dissipation from FZ during the welding [92]. Further, the macrostructure of Ti-15-3 welds made using Ni-modified Ti-15-3 fillers (Ti-15-3-0.15 Ni, Ti-15-3-0.3 Ni, and Ti-15-3-0.5 Ni) are compared in Fig 6.1(b, c and d) respectively. The macrostructure of the weld made using Ti-15-3-0.15 Ni filler (Fig 6.1b) showed FZ morphology similar to that of the autogenous Ti-15-3 weldment. However, with an increase in wt% of Ni from 0.15 to 0.3, the columnar grains are gradually transformed into equiaxed grains (Fig 6.1c), with a co-existence of columnar and equiaxed grains. Conversely, a further increase in wt % of Ni from 0.3 to 0.5 (Fig 6.1d) resulted in a higher amount of equiaxed grains in the FZ. In contrast, the macrostructure of Ti-15-3 welds made using Si-modified Ti-15-3 fillers (Ti-15-3-0.15 Si, Ti-15-3-0.3 Si, and Ti-15-3-0.5 Si) are compared in Fig 6.1(e, f and g) respectively. An increase in the fraction of the equiaxed grains in the FZ is observed in the weld FZ with the increase in the Si content of the fillers. Notably, the average bead width for all the weldments falls within the range of 8-9 mm.

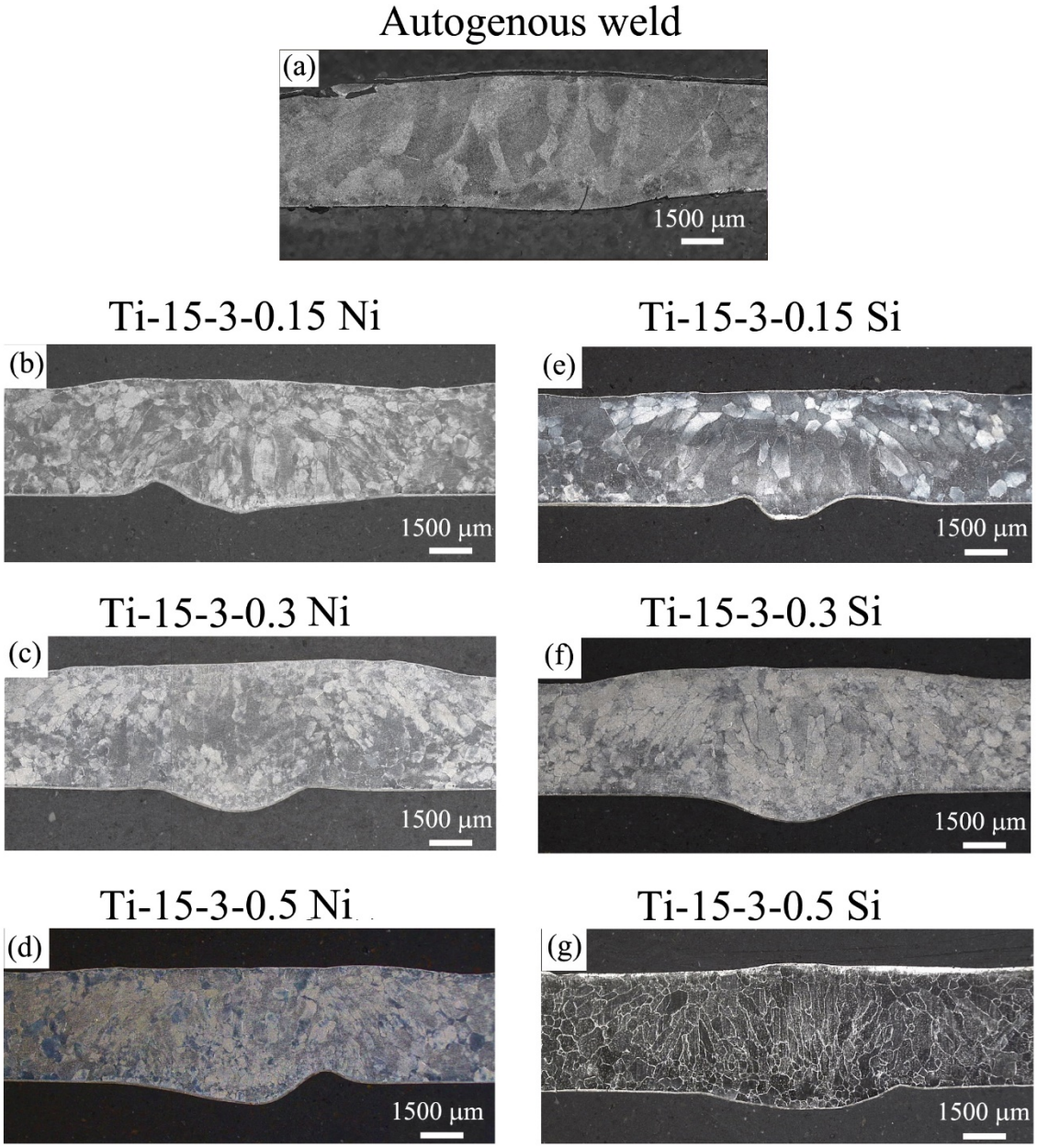

Fig 6.1: FZ macrostructure of the as-welded GTAW (a) autogenous weld, welds prepared using Ni-modified fillers (b) Ti-15-3-0.15 Ni (c) Ti-15-3-0.3 Ni (d) Ti-15-3-0.5 Ni and welds prepared using Si-modified fillers (e) Ti-15-3-0.15 Si (f) Ti-15-3-0.3 Si (g) Ti-15-3-0.5 Si.

6.2 Weld microstructure in as-welded condition:

The FZ optical micrographs of the Ti-15-3 autogenous weld (Fig 6.2a) showed a coarse grain structure. The FZ microstructure of Ti-15-3 welds made using Ni-modified Ti-15-3 fillers (Ti-15-3-0.15 Ni, Ti-15-3-0.3 Ni and Ti-15-3-0.5 Ni) are compared in Fig 6.2(b, c and d) respectively. The average grain sizes within the FZ of each condition of welds were measured as presented in Table 6.1. The autogenous weld exhibits an average grain size of 325 ± 13µm.

On the other hand, the weldments prepared using Ti-15-3-0.15 Ni, Ti-15-3-0.3 Ni, and Ti-15-3-0.5 Ni fillers showed grain sizes of 255 ± 12 μm, 194 ± 16 μm, and 118 ± 13 μm, respectively. A remarkable grain refinement has been observed in the welds prepared with Ni-modified fillers compared to autogenous welds. Similar grain refinement was reported with the addition of trace Ni addition in additive manufacturing of Ti-6Al-4V alloy [89]. Further, the FZ microstructures of the weldments prepared with Ti-15-3-0.15 Si, Ti-15-3-0.3 Si and Ti-15-3-0.5 Si fillers are shown in Fig. 6.2(e, f and g) respectively. The average FZ grain sizes of the weldments prepared with Ti-15-3-0.15 Si, Ti-15-3-0.3 Si, and Ti-15-3-0.5 Si fillers are 264 ± 11, 182 ± 15, and 126 ± 6 um, respectively. Similar to the Ni-modified fillers, adding Si in fillers also resulted in grain refinement within the FZ compared to the autogenous weld. Similar to Ni, Si also acts as a grain refiner; with increased Si content, leads to the narrowing of numerous columnar grains as a result of the rejection of silicon-rich solutes. This phenomenon retards grain growth in that direction and encourages additional nucleation at the starting points of the columnar structure.

Table 6.1: FZ grain size of welded samples.

Weld	**Average grain size (μm)**
Autogenous	325 ± 13
Ti-15-3-0.15 Ni filler	255 ± 12
Ti-15-3-0.3 Ni filler	194 ± 16
Ti-15-3-0.5 Ni filler	118 ± 13
Ti-15-3-0.15 Si filler	264 ± 11
Ti-15-3-0.3 Si filler	182 ± 15
Ti-15-3-0.5 Si filler	126 ± 6

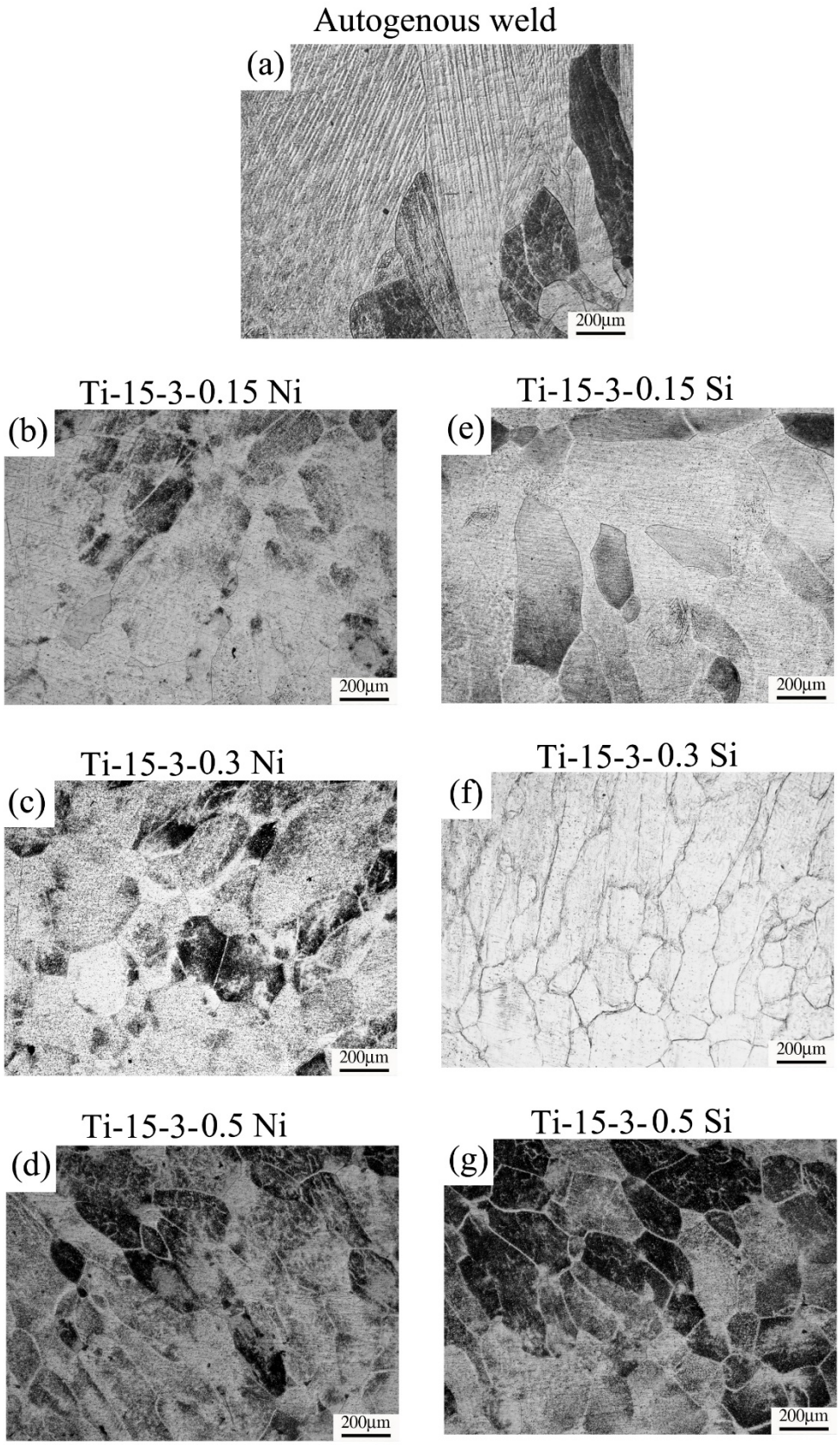

Fig 6.2: FZ microstructure of the as-welded GTAW (a) autogenous weld, welds prepared using Ni-modified fillers (b) Ti-15-3-0.15 Ni (c) Ti-15-3-0.3 Ni (d) Ti-15-3-0.5 Ni and welds prepared using Si-modified fillers (e) Ti-15-3-0.15 Si (f) Ti-15-3-0.3 Si (g) Ti-15-3-0.5 Si.

From the microstructural analysis, it is clear that the addition of Ni and Si in Ti-15-3 fillers helps in the refinement of grains in the FZ of the welds. Furthermore, it is evident that the inclusion of Ni and Si in the fillers has not only transformed the grain morphology from columnar to equiaxed grains but has also significantly augmented the proportion of equiaxed grains within the FZ. The effect of Ni and Si additions on mean grain sizes of welds made with Ti-15-3-xNi and Ti-15-3-xSi fillers (x = 0.15, 0.3, and 0.5) are compared with autogenous welds are shown in Fig 6.3.

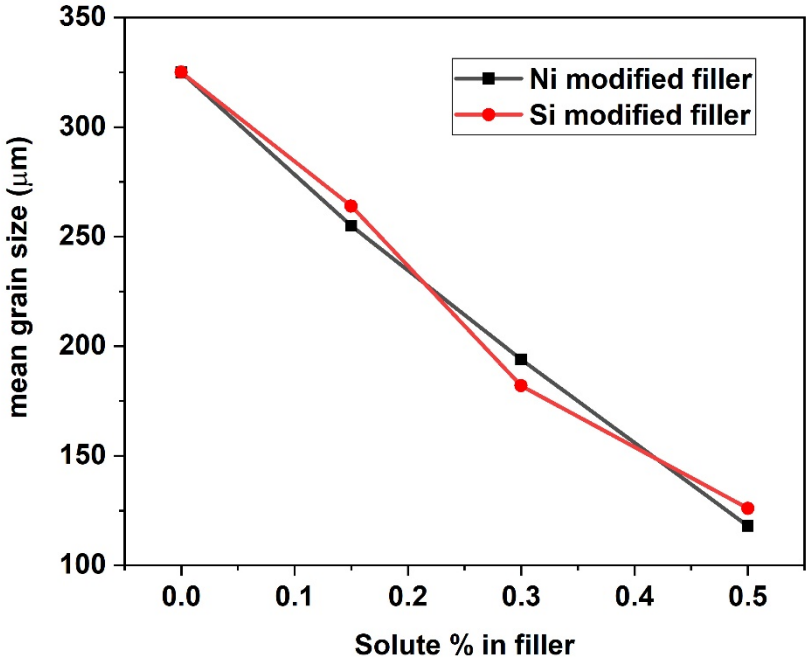

Fig 6.3: Variation of weld metal mean grain size with Ni/Si content in the Ti-15-3 filler.

Fig 6.4(a-c) shows EBSD inverse pole figure (IPF) map for the Ti-15-3 weld in autogenous condition and Ti-15-3 welds made with Ti-15-3-0.5 Ni and Ti-15-3-0.5 Si, respectively. As shown in Fig 6.4a, the FZ grains in the autogenous welds are randomly oriented columnar grains with a small portion of equiaxed grains. The addition of Ni and Si to the fillers has also yielded a random crystallographic orientation in the FZ (Fig 6.4b and c). However, the addition of Ni and Si resulted in more equiaxed grains in the FZ compared to the autogenous weldment. The EBSD analysis of Ti-15-3 autogenous weld, Ti-15-3 welds made using Ti-15-3-0.5 Ni and Ti-15-3-0.5 Si has shown the mean FZ grain size values of 335 ± 12 μm, 122 ± 13 μm, and 135 ± 6 μm, respectively. The grain size results of EBSD analysis are in good agreement with the average FZ grain sizes measured using optical micrographs.

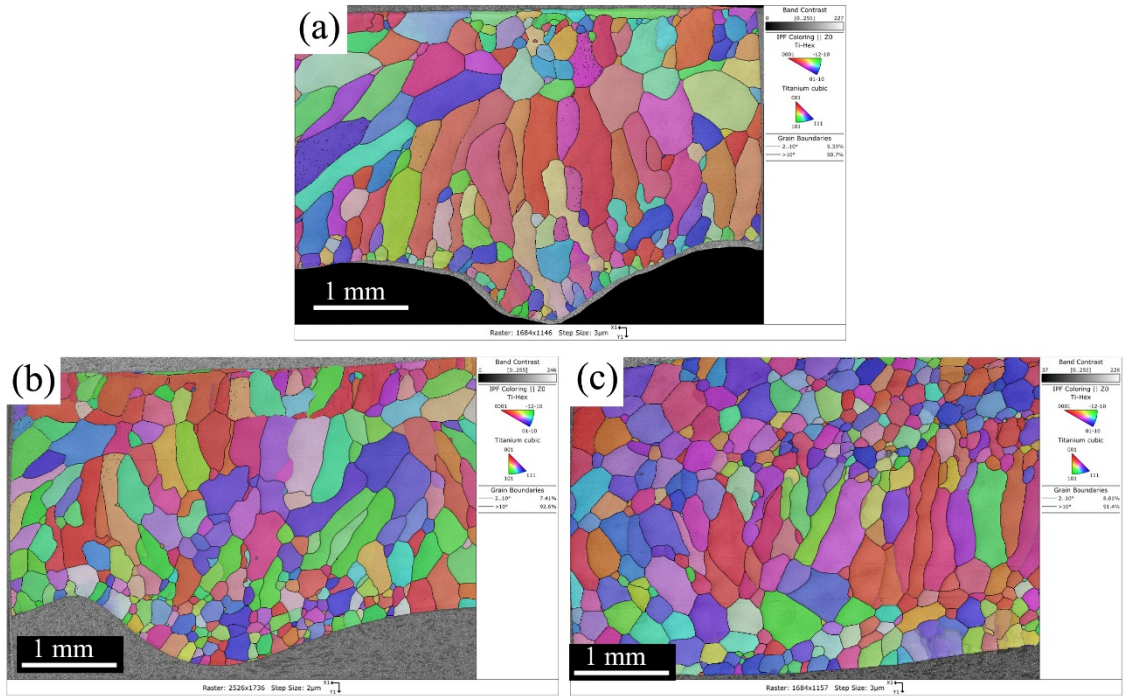

Fig 6.4: (a) EBSD FZ image of GTA welded Ti-15-3 (a) autogenous weld (b) using Ti-15-3-0.5 Ni filler and (c) using Ti-15-3-0.5 Si filler.

The SEM images in the FZ of the autogenous Ti-15-3 welds and welds made using Ti-15-3-0.5 Ni filler and Ti-15-3-0.5 Si filler are shown in Fig. 6.5(a-c), respectively. The SEM micrographs displayed β-grain boundaries, irrespective of the weld condition. On the other hand, the examination of SEM images of welds prepared with Ni and Si-modified Ti-15-3 fillers did not reveal any morphological features resembling any particles. This observation can be attributed to the limited amount of α phase/Ti-Ni and Ti-Si particles formed during the cooling process [54]. To gain further insights into the FZ, a TEM analysis of the welds was conducted.

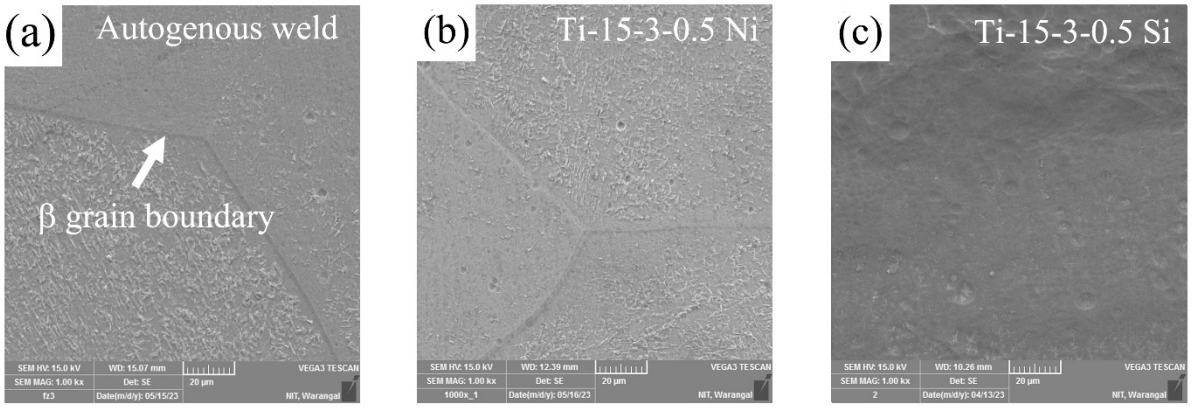

Fig 6.5: Scanning electron micrograph of GTA welded Ti-15-3 (a) autogenous weld (b) using Ti-15-3-0.5 Ni filler and (c) using Ti-15-3-0.5 Si filler.

Optical micrograph of weld cross-section showing FZ, HAZ, and BM for welds prepared using Ti-15-3-0.5 Ni and Ti-15-3-0.5 Si fillers are shown in Fig 6.6a and b, respectively. HAZ grain coarsening was observed compared to the base metals for the welds prepared using Ti-15-3-0.5 Ni and Ti-15-3-0.5 Si fillers. The average grain sizes of HAZ in weld made using Ti-15-3-0.5 Ni filler and Ti-15-3-0.5 Si are 105 ± 5 μm and 112 ± 7 μm, respectively. Given that the kinetics of grain growth is strongly influenced by temperature, the HAZ experiences grain coarsening due to the elevated temperatures reached during the welding process. Consequently, grain growth within the HAZ region near the fusion boundary is more pronounced compared to the HAZ regions situated farther from the FZ, namely, towards the base metal. The HAZ area near the fusion boundary comprises equiaxed grains that have undergone partial melting during the welding's melting phase. These partially melted grains then undergo coarsening and an epitaxial growth process toward the center of the FZ during the solidification [106].

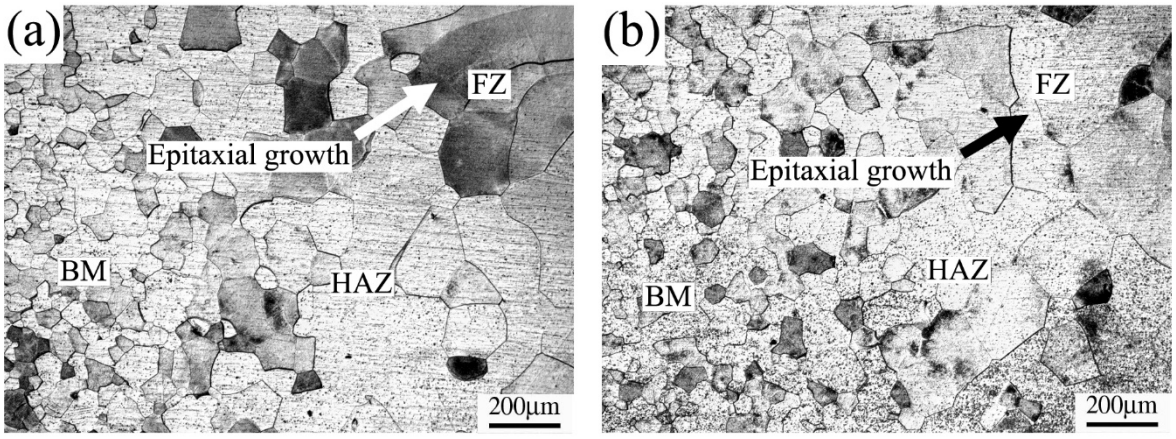

Fig 6.6: Microstructure of weld cross-section showing FZ, HAZ, and BM for welds prepared using (a) Ti-15-3-0.5 Ni and (b) Ti-15-3-0.5 Si fillers

Fig 6.7a and b depicts the TEM images in the FZ of the weldments made with Ti-15-3-0.5 Ni filler and Ti-15-3-0.5 Si fillers, while the corresponding energy dispersive X-ray spectrums (EDS) showed in Fig 6.7c and d, respectively. The TEM image in the FZ of the weldment prepared with Ti-15-3-0.5 Ni filler (Fig 6.7a) reveals the presence of tiny particles in the matrix. The EDS analysis revealed the presence of Ni along with the other alloying elements of Ti-15-3 (Fig 6.7c). While, the weldment prepared with Ti-15-3-0.5 Si filler (Fig 6.7b) also exhibited small particles similar to that in the weldments prepared with Ni-modified filler. The EDS spectrum taken on the particles indicated the presence of Si (Fig 6.7d). These Si-rich particles are also segregated similarly to Ni-rich particles.

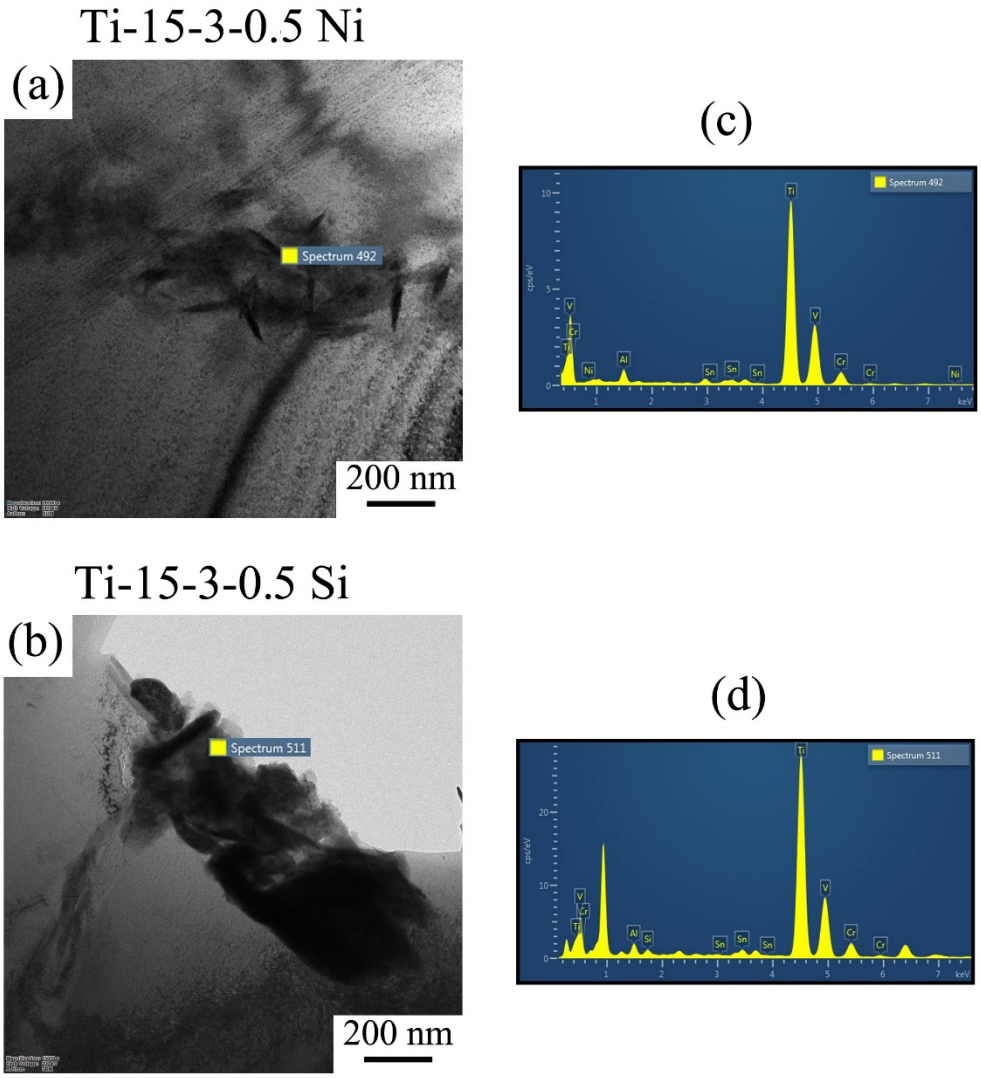

Fig 6.7: FZ TEM of the welds prepared using (a) Ti-15-3-0.5 Ni and (b) Ti-15-3-0.5 Si fillers and corresponding (c, d) EDS spectrum of respective fillers.

6.3 Grain refinement mechanism in fusion zone:

Grain refinement during the solidification is beneficial in developing homogeneous microstructure and improved in-service performance for cast and welded components. The presence of nuclei, solutes, and thermal and constitutional undercooling during the solidification play a major role in the development of the solidification microstructure [73]. The presence of nuclei serves as a substrate for grain growth, while solute segregation at the S/L interface provides the constitutional undercooling necessary for the improved nucleation rate. The solute segregation's contribution to the constitutionally undercooled zone development rate ahead of the solidification front can be quantified using the growth restriction

factor (GRF), denoted as Q [83]. The growth restriction factor can be computed using a binary phase diagram with the Equation 6.1.

$$Q = m(k\text{-}1)\, C_0 \quad \text{----------} \quad 6.1\ [83]$$

Where m represents the liquidus line slope, k denotes the partition coefficient of solute ($k = C_s/C_l$; C_l and C_s correspond to the solute contents of the liquid and solid in equilibrium at the interface). C_0 stands for the solute content of the alloy. Solute elements with higher GRF values exhibit pronounced segregation ahead of the advancing interface, leading to a rapid accumulation of constitutional undercooling. The faster the development of the constitutional undercooled zone, the more conducive it becomes for subsequent nucleation ahead of the advancing S/L interface, ultimately resulting in smaller grain sizes. Table 6.2 shows the m(k-1) values for few solute elements in Ti [20]. The calculated Q values of Ni and Si at different concentrations in Ti are presented in Table 6.3.

Table 6.2: Calculated values of Q for various elements in titanium, equivalent to m*(k-1).*

Element	m	k	m(k-1)	Reference
Al	-2.1	~1	0	[22]
V	-4.7	~1	0	[22]
Sn	-0.8	~1	0	[22]
Cr	-8.1	0.81	1.5	[22]
Ni	-23.8	0.4	14.3	[19]
Si	-32.5	0.35	21.7	[19]

To calculate Q, multiply m(k − 1) by C_0 in wt. %.

Table 6.3: Average Ni and Si content in the weld zone and calculated GRF values.

Filler	Average solute (Ni/Si) content in the weld zone C_o (wt%)	Calculated Q value ($mC_o(k\text{-}1)$)
Ti-15-3-0.15 Ni	0.02	0.286
Ti-15-3-0.3 Ni	0.04	0.572
Ti-15-3-0.5 Ni	0.06	0.858
Ti-15-3-0.15 Si	0.02	0.434
Ti-15-3-0.3 Si	0.04	0.868
Ti-15-3-0.5 Si	0.06	1.302

These values provide the basis for understanding the grain refinement within the FZ of Ti-15-3 welds crafted using Ti-15-3-x wt.% Ni and Ti-15-3-x wt.% Si (x = 0.15, 0.3, and 0.5) fillers, elucidated through the growth restriction mechanism. It is noted that calculated GRF values for welds made Ti-15-3-x wt.% Ni (x = 0.15, 0.3, and 0.5) fillers are 0.286, 0.572 and 0.858, respectively. Whereas for welds made Ti-15-3-x wt.% Si (x = 0.15, 0.3, and 0.5) fillers are 0.434, 0.868, and 1.302, respectively. Among the welds prepared, the smallest grain size is observed in the welds made using Ti-15-3-0.5 Ni and Ti-15-3-0.5 Si fillers. This effect arises from the elevated solute concentrations of Ni and Si within the weld zone, resulting in higher GRF values (0.858 for 0.5 wt% Ni; 1.302 for 0.5 wt% Si). This robust segregation ahead of the advancing S/L interface leads to an accumulation of constitutional undercooling. The expedited development of the constitutional undercooled zone, in turn, facilitates enhanced nucleation ahead of the advancing S/L interface, consequently yielding a reduced grain size. Therefore, the welds prepared with Ti-15-3-0.5 Ni and Ti-15-3-0.5 Si fillers have exhibited more equiaxed grains in the FZ.

Easton and St. John proposed a model used to predict the grain size by considering the influence of both solute and nuclei on refinement of grains, which is given by [20].

$$d = \frac{1}{\sqrt[3]{\rho.f}} + \frac{b'\Delta T_n}{Q} \quad \text{---------- 6.2[20]}$$

Here, d signifies the grain size, ρ represents nucleant particle density, f denotes the faction of activated nucleant particles, b' stands as a constant, and ΔT_n signifies the undercooling necessary to activate nucleation. The 1st term in Equation 6.2 pertains to the availability of nuclei, while the 2nd term relates to the effectiveness of the nuclei in conjunction with the development of the constitutionally supercooled zone. Assuming an equal count of nucleates in an alloy across varying Q values leads to fluctuations in grain refinement under experimental conditions [20].

In the present study, the collected data of Ni and Si additions have been utilized to plot grain size (d) against 1/Q (Fig 6.8). The addition of Ni and Si solutes in Ti-15-3 fillers is justified by their relatively large GRF values, as shown in Table 6.3. The observation that 'd vs 1/Q' plot for both Ni and Si additions data sets show linear fit (Fig 6.8), suggesting a good agreement with the model described by Equation 6.2. For both Ni and Si additions to the fillers, the increased solute content led to a decrease in grain size. However, there is a significant disparity in the rate of grain size reduction between the welds employing Ni and Si-modified Ti-15-3 fillers. This discrepancy implies that the potency of the nuclei, represented by ΔTn, varies among the alloy systems. Specifically, Si-modified filler data exhibits a steeper gradient than

Ni-modified filler data (Fig. 6.8), indicating that the potency of the nuclei is higher when Ni is added to the filler compared to the Si additions.

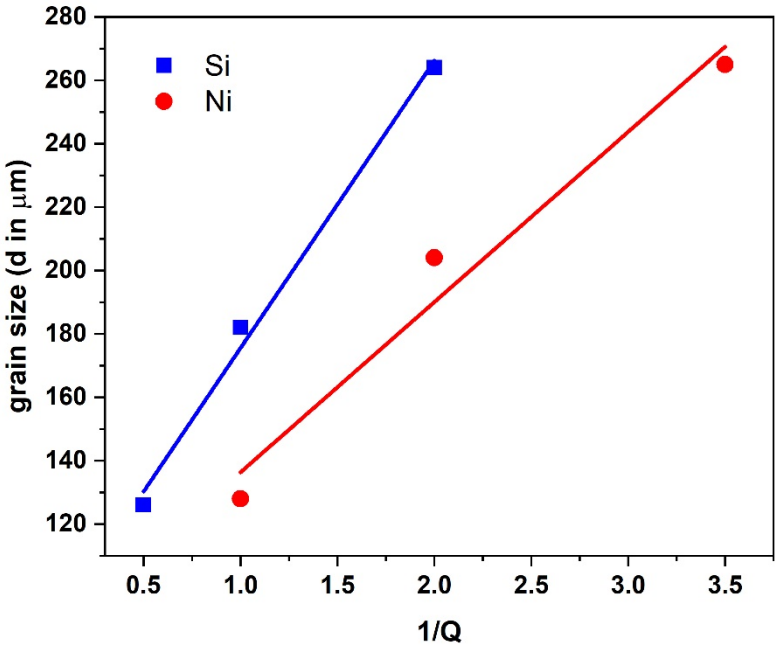

Fig 6.8: Grain size (d) against 1/Q calculated using experimental data (k and C_o) for Ni and Si additions.

As depicted in Fig 6.9, Ni and Si addition to the Ti-15-3 fillers can enhance the ability to generate a constitutionally supercooled zone in the Ti-15-3 weld zone. Fig. 6.9 is the schematic diagram depicting the solidification of autogenous welds and welds made with Ni or Si-modified fillers. The blue and red lines represent the melting temperature (T_m) of the alloy and the thermal gradient (T_a) of the weld zone. For Ti-15-3 autogenous weld where there is no segregation of solute in the advancing S/L interface, it exhibits the limited ability to generate CSZ, resulting in no supercooling necessary for nucleation ($T_m < T_a$). Consequently, the initial grains continuously grow in an epitaxial fashion, leading to the formation of coarser columnar grains in the FZ of the autogenous weld. However, in the welds made with the incorporation of Ni and Si to the Ti-15-3 fillers, the capacity for CSZ generation is enhanced, causing the T_m to exceed the T_a, thereby creating a high degree of undercooling in the FZ. The region below the curve represents the CSZ of the weld prepared using the Ti-15-3-0.5 Ni filler and Ti-15-3-0.5 Si filler, respectively. Consequently, the formation of new grains occurs, which impedes the initial grains that grow in an epitaxial fashion. This phenomenon ultimately leads to the refinement of the final grain size within the FZ.

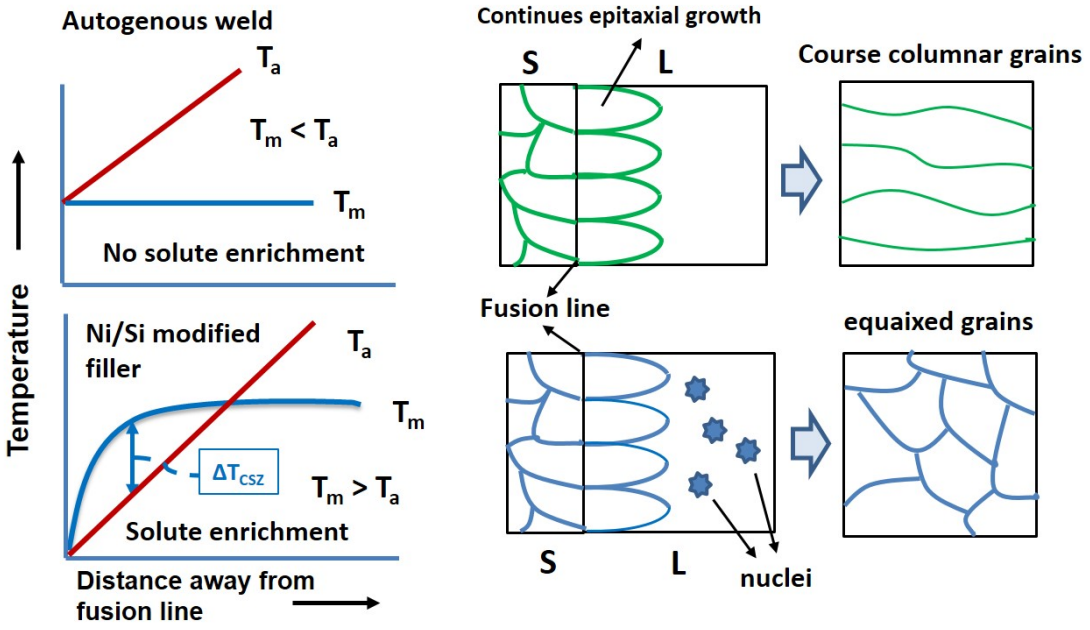

Fig 6.9: Schematic diagram showing the effect of solute enrichment in liquid on solidification mode in the FZ.

6.4 Weld microstructure in PWHT condition:

The TEM image of Ti-15-3 FZ GTA welds made with Ti-15-3-0.5 Ni and Ti-15-3-0.5 Si filler in PWHT condition are shown in Fig 6.10a and b, respectively. The TEM images reveal that the precipitates exhibit elliptical morphologies and are uniformly distributed throughout the β matrix. The average size of α precipitates formed in both conditions measured approximately 35 ± 5 nm. The formation of α precipitates after PWHT can be ascribed to the presence of metastable β in the as-welded condition. Furthermore, the addition of Ni and Si to the fillers resulted in a decrease in grain size, thereby increasing the grain boundary area. These findings are consistent with the results made by Balachandar et al [16].

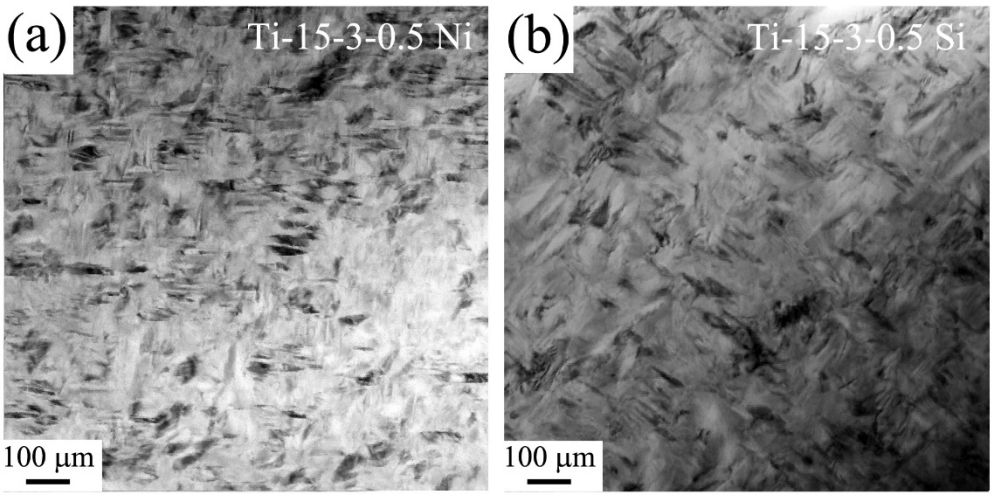

Fig 6.10: FZ TEM of welds made using (a) Ti-15-3-0.5 Ni filler and (b) Ti-15-3-0.5 Si filler in PWHT condition.

Fig 6.11 a and b display the XRD analysis in the FZ of Ti-15-3 welds in the autogenous condition and base metal compared with welds made with Ti-15-3-0.5 Ni and Ti-15-3-0.5 Si filler. The XRD pattern of welds prepared with Ti-15-3-0.5 Ni and Ti-15-3-0.5 Si in as-welded conditions revealed only body-centered cubic (bcc) β-Ti phase as similar to peaks observed in autogenous welds. In contrast, the PWHT weld samples prepared using modified fillers exhibited a combination of the hcp α-Ti phase along with the bcc β phase. The XRD patterns did not show any other phase rich in either Ni or Si in both PWHT and as-welded conditions.

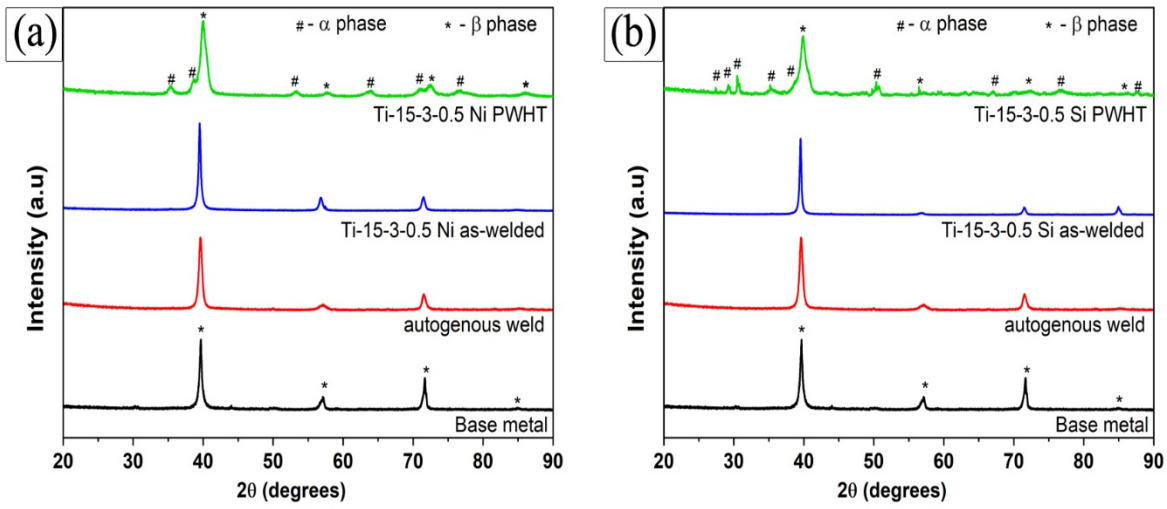

Fig 6.11: Indexed XRD patterns showing phases of welds made using (a) Ni-modified fillers and (b) Si-modified fillers in the as-welded and PWHT conditions.

6.5 Mechanical Properties

6.5.1 Hardness

Fig 6.12a and b display the hardness profile across the Ti-15-3 autogenous weld compared with welds made with Ti-15-3-x wt.%Ni (x = 0.15, 0.3, 0.5) and Ti-15-3-x wt.% Si (x = 0.15, 0.3, 0.5) filler, respectively. The Ti-15-3 autogenous weld showed the lowest hardness (235 ± 3 HV) in FZ among all the welds, and the hardness increases as the distance increases from the weld center. In contrast, the as-welded welds made of Ni-modified fillers showed higher FZ hardness than autogenous welds. This lower hardness in autogenous welds is attributed to FZ's coarser columnar β grains. Among all the as-welded welds made of Ni-modified fillers, the welds made using Ti-15-3-0.5 Ni exhibited the highest hardness (262 ± 3 HV) in FZ compared

to other weldments made of Ti-15-3-0.3 Ni (250 ± 3 HV) and Ti-15-3-0.15 Ni (240 ± 3 HV). This could be due to the greater extent of grain refinement in the FZ of the weld made of Ti-15-3-0.5 Ni filler, which impedes the dislocation movement along the grain boundaries, consequently leading to increased hardness [18]. In addition, the low hardness value in the HAZ region, compared to the BM, can be ascribed to the coarsening of grains in the BM near the fusion boundary. Conversely, the higher hardness in the BM, compared to the HAZ region, is a result of its cold-worked microstructure and finer grains. This means that the higher hardness observed in the HAZ region, in comparison to the FZ, is due to the smaller grain size in the HAZ region compared to the grains present in the FZ in all as-welded welds. Furthermore, the welds subjected to PWHT exhibit a similar trend in the hardness profile as that of as-welded welds made with Ni-modified fillers, as depicted in Fig. 16a. Among all the PWHT welds made of Ni-modified fillers, the welds made using Ti-15-3-0.5 Ni exhibited the highest hardness (402 ± 3 HV) in the FZ compared to other weldments made of Ti-15-3-0.3 Ni and Ti-15-3-0.15 Ni fillers. This increase in hardness can be attributed to the uniform distribution of fine α particles precipitated throughout the FZ in the welds made of Ti-15-3-0.5 Ni filler compared to other PWHT weldments made of Ni-modified fillers [105].

On the other hand, the welds made with Si-modified fillers showed a similar trend in hardness of as-welded and PWHT welds like that of welds made of Ni-modified fillers (Fig 6.12b). The higher hardness in the FZ of the as-welded condition has been observed in welds made using Ti-15-3-0.5 Si filler (260 ± 3 HV) compared to other weldments. But after being subjected to the PWHT, all the welds showed a higher hardness in the FZ compared to as-welded samples. Among all the PWHT welds made of Si-modified fillers, the welds made using Ti-15-3-0.5 Si showed the highest hardness (408 ± 3 HV) in the FZ compared to welds made with Ti-15-3-0.3 Si and Ti-15-3-0.15 Si filler. This may be attributed to finer α precipitates in welds made of Ti-15-3-0.5 Si filler than that of other weldments. These findings align with the results made by Kuroda et al. [29] in their study on GTAW of Ti-15-3, which indicates an increase in weld metal hardness after PWHT. It is assumed that PWHT reduces the residual stresses in the weldments compared to the as-welded samples. However, any decrease in hardness associated with reducing residual stresses is expected to be insignificant compared to the hardness increase resulting from precipitate strengthening.

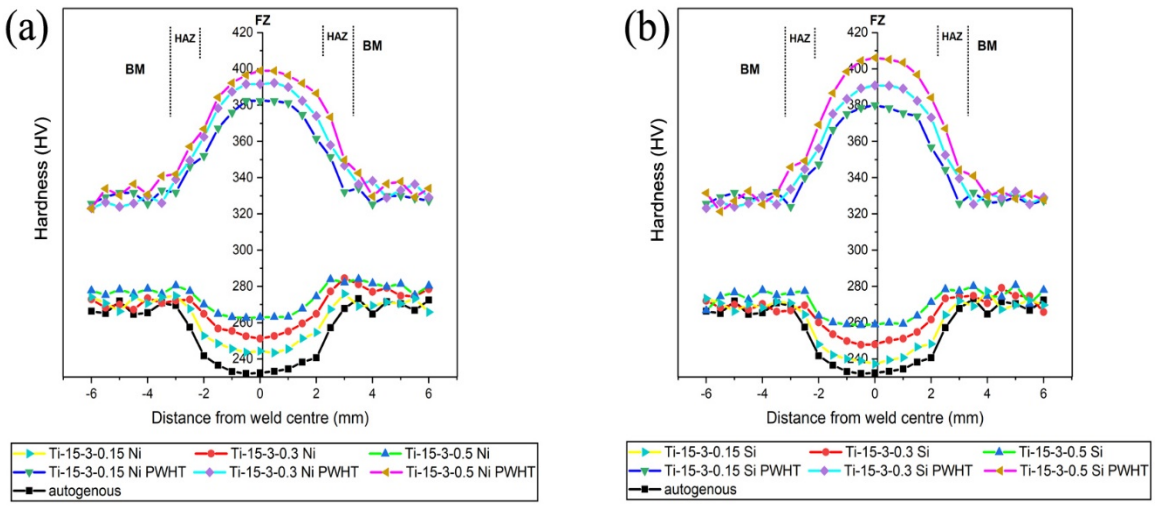

Fig 6.12: Hardness profiles across the GTA Ti-1533 welds prepared using (a) Ni-modified fillers and (b) Si-modified fillers in as-welded and PWHT conditions.

6.5.2 Tensile properties:

Results of tensile tests in as-welded and PWHT condition of the BM, Ti-15-3 autogenous weld, welds made with Ti-15-3-x wt.% Ni (x = 0.15, 0.3, 0.5) and Ti-15-3-x wt.% Si (x = 0.15, 0.3, 0.5) fillers are compared in Table 6.4. The results obtained from tensile tests conducted on transverse tensile welds made with Ti-15-3-xNi (x = 0.15, 0.3, 0.5) and Ti-15-3-xSi (x = 0.15, 0.3, 0.5) fillers are graphically represented in Fig 6.13a and b, respectively. The presented tensile data for each condition represents an average of measurements taken from three welded specimens. The BM exhibits YS of 706 ± 4 MPa, UTS of 747 ± 5 MPa, and %E of 16 ± 0.5. It is noteworthy that autogenous welded tensile samples exhibited lower YS (575 ± 4 MPa), UTS (597 ± 4 MPa), and %E (11 ± 0.5) than BM due to coarse grain formation in FZ. In other words, the higher strength of BM compared to weldments is due to fine gain size and cold-worked microstructure. While Fig 6.13a demonstrates the welds fabricated using Ti-15-3-xNi (x = 0.15, 0.3, 0.5), fillers showed enhanced strength compared to the autogenous welds. Among all the as-welded welds made of Ni-modified fillers, the welds made using Ti-15-3-0.5 Ni filler exhibited the highest strength (YS = 688 ± 6 MPa, UTS = 721 ± 5 MPa, %E = 9 ± 0.5%) compared to those made with Ti-15-3-0.3 Ni (YS = 664 ± 4 MPa, UTS = 698 ± 4 MPa, %E = 7 ± 0.4%) and Ti-15-3-0.15 Ni filler (YS = 619 ± 4 MPa, UTS = 632 ± 5 MPa, %E = 5 ± 0.5%). This improvement can be attributed to higher grain refinement and more equiaxed grain formation in FZ due to the higher concentration of Ni. As discussed earlier, a greater GRF value (0.858) of high Ni concentration (0.5 wt%Ni) in Ti leads to strong segregation ahead of

the advancing S/L interface. This results in increased constitutional undercooling leading to the survival of more nuclei and the formation of more equiaxed grains. Moreover, the possibility of the formation of Ti-Ni intermetallic compounds could introduce hindrances to dislocation mobility during plastic deformation. These dislocations would need to either bend around or pass through these precipitates to continue deformation, to necessitate higher forces [89]. In another case, the welds made with Ti-15-3-xSi (x = 0.15, 0.3, 0.5) filler also showed a similar trend of tensile properties as welds prepared using Ni-modified fillers. Among all the as-welded welds made of Si-modified fillers, the welds made using Ti-15-3-0.5 Si filler exhibited the highest strength (YS = 693 ± 6 MPa, UTS = 725 ± 5 MPa, %E = 8 ± 0.5) compared to welds made with Ti-15-3-0.3 Si (YS = 656 ± 4MPa, UTS = 676 ± 4 MPa, %E = 7 ± 0.4) and Ti-15-3-0.15 Si filler (YS = 608 ± 4 MPa, UTS = 621 ± 5 MPa, %E = 6 ± 0.5). The higher strength in welds made with Ti-15-3-0.5 Si filler due to the higher GRF value of Si (at 0.5 wt% Si) in Ti resulted in a greater extent of constitutional undercooling leading to refinement of grains in the FZ.

The UTS and YS of the weldments significantly increase after PWHT compared to the as-welded conditions, as demonstrated by the graph presented in Fig 6.13. The strengthening mechanism behind this enhancement may be ascribed to the precipitation of the α phase within the β matrix [29]. In the two-step aging process, the initial step at 300°C leads to the formation of the ω phase, which subsequently acts as a nucleation site for the subsequent formation of α fine precipitates. Among the different weld conditions considered, the weldments prepared with Ti-15-3-0.5 Ni filler exhibit superior strength but low elongation compared to those fabricated with low Ni content under the PWHT condition. A similar trend has been observed in the case of Si-added fillers. This improvement can be attributed to the higher density of α precipitates within the β matrix at higher content of Si and Ni because of the smaller grain size. However, an increased quantity of α precipitates along the grain boundaries in PWHT welds might lead to observable embrittlement, consequently reducing ductility.

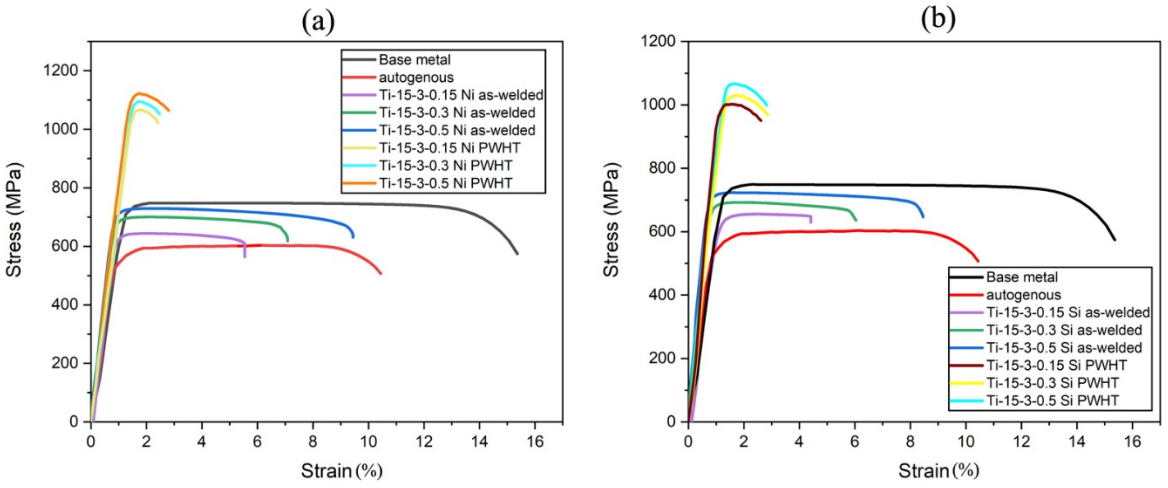

Fig 6.13: Strain-strain curves for the GTA Ti-15-3 welds prepared using (a) Ni-modified fillers and (b) Si-modified fillers in as-welded and PWHT conditions compared with the BM and autogenous weld.

Table 6.4: Variation in tensile properties of as-welded and PWHT of welds prepared using Ni and Si-modified fillers in comparison with BM and autogenous

Condition	Yield Strength (YS), MPa	Ultimate Tensile Strength (UTS), MPa	Elongation (%E)
Ti15333 Base metal	706 ± 4	747 ± 5	16 ± 0.5
Autogenous	575 ± 4	597 ± 4	11 ± 0.5
Ti-15-3-0.15 Ni filler	619 ± 4	632 ± 5	5 ± 0.5
Ti-15-3-0.3 Ni filler	664 ± 4	698 ± 4	7 ± 0.4
Ti-15-3-0.5 Ni filler	688 ± 6	721 ± 5	9 ± 0.5
Ti-15-3-0.15 Ni filler PWHT	1042 ± 2	1054 ± 4	2 ± 0.2
Ti-15-3-0.3 Ni filler PWHT	1074 ± 2	1082 ± 2	2 ± 0.4
Ti-15-3-0.5 Ni filler PWHT	1112 ± 4	1125 ± 8	2 ± 0.5
Ti-15-3-0.15 Si filler	608 ± 4	621 ± 5	6 ± 0.5
Ti-15-3-0.3 Si filler	656 ± 4	676 ± 4	7 ± 0.4
Ti-15-3-0.5 Si filler	693 ± 6	725 ± 5	8 ± 0.5
Ti-15-3-0.15 Si filler PWHT	1012 ± 7	1018 ± 4	2 ± 0.2
Ti-15-3-0.3 Si filler PWHT	1056 ± 2	1061 ± 2	2 ± 0.4

Ti-15-3-0.5 Si filler PWHT	1084 ± 4	1092 ± 8	2 ± 0.5

Fig 6.14(a-c) depicts fractured tensile specimens in as-welded conditions, where Fig 6.14a represents the autogenous weld, Fig 6.14b and c display the weld made using Ti-15-3-0.5 Si filler and Ti-15-3-0.5 Ni filler, respectively. The autogenous welds failed in the middle of the FZ while the failure location shifted close to the fusion boundary for the welds prepared using Si and Ni-modified fillers. In contrast, Fig 6.14(d-f) showed the PWHT conditions of respective welds in a similar sequence. All PWHT conditions have failed in the HAZ/BM region, indicating higher hardness in the FZ than in BM.

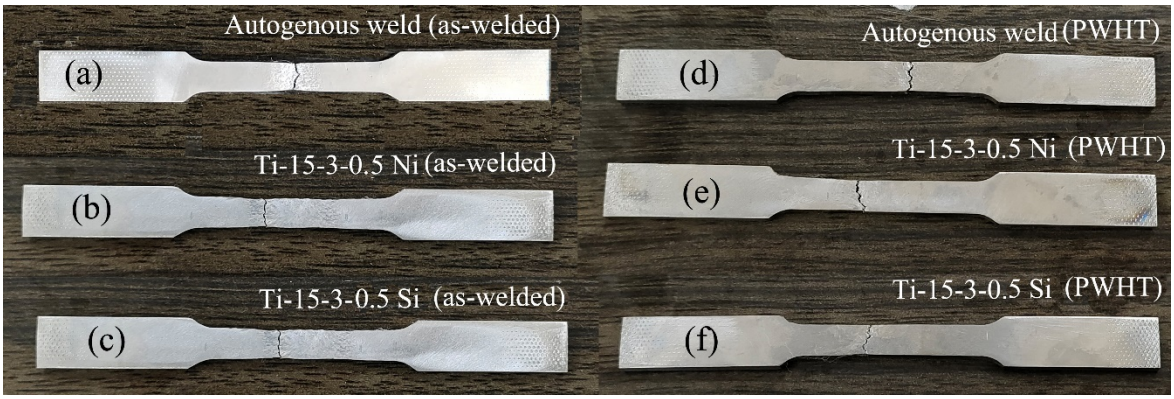

Fig 6.14: The Failure location of GTA (a) autogenous weld (b) Ti-15-3-0.5 Ni filler weld and (c) Ti-15-3-0.5 Si filler weld in the as-welded condition; (d-f) respective welds in PWHT condition.

Fig 6.15(a-c) illustrates the tensile fracture surfaces of the as-welded condition in all the specimens, where Fig 6.15a indicates the autogenous weld, Fig 6.15b and c depict the weld made using Ti-15-3-0.5 Si filler and Ti-15-3-0.5 Ni filler, respectively. In comparison, Fig. 6.15(d-f) showcases distinct characteristics of PWHT specimens for the respective welds in the same sequential order. The fractured surfaces of autogenous weld showed larger dimples with some river marks, as shown in Fig. 6.15a. In contrast, the welds made using Ti-15-3-0.5 Si filler (Fig 6.15b) and Ti-15-3-0.5 Ni filler (Fig 6.15c) displays areas of fine dimple features surrounded by cleavage morphology. During the aging process of welds, the formation of a hard α-phase strengthens the soft β-phase, resulting in fracture surfaces with reduced ductility characteristics and the presence of interdendritic cracks. Consequently, potential necking instability and fracture can manifest near the relatively pliable parent material at the end of the HAZ in the PWHT samples of Ti-15-3 welds. These findings align with the investigations conducted by Becker et al.[97].

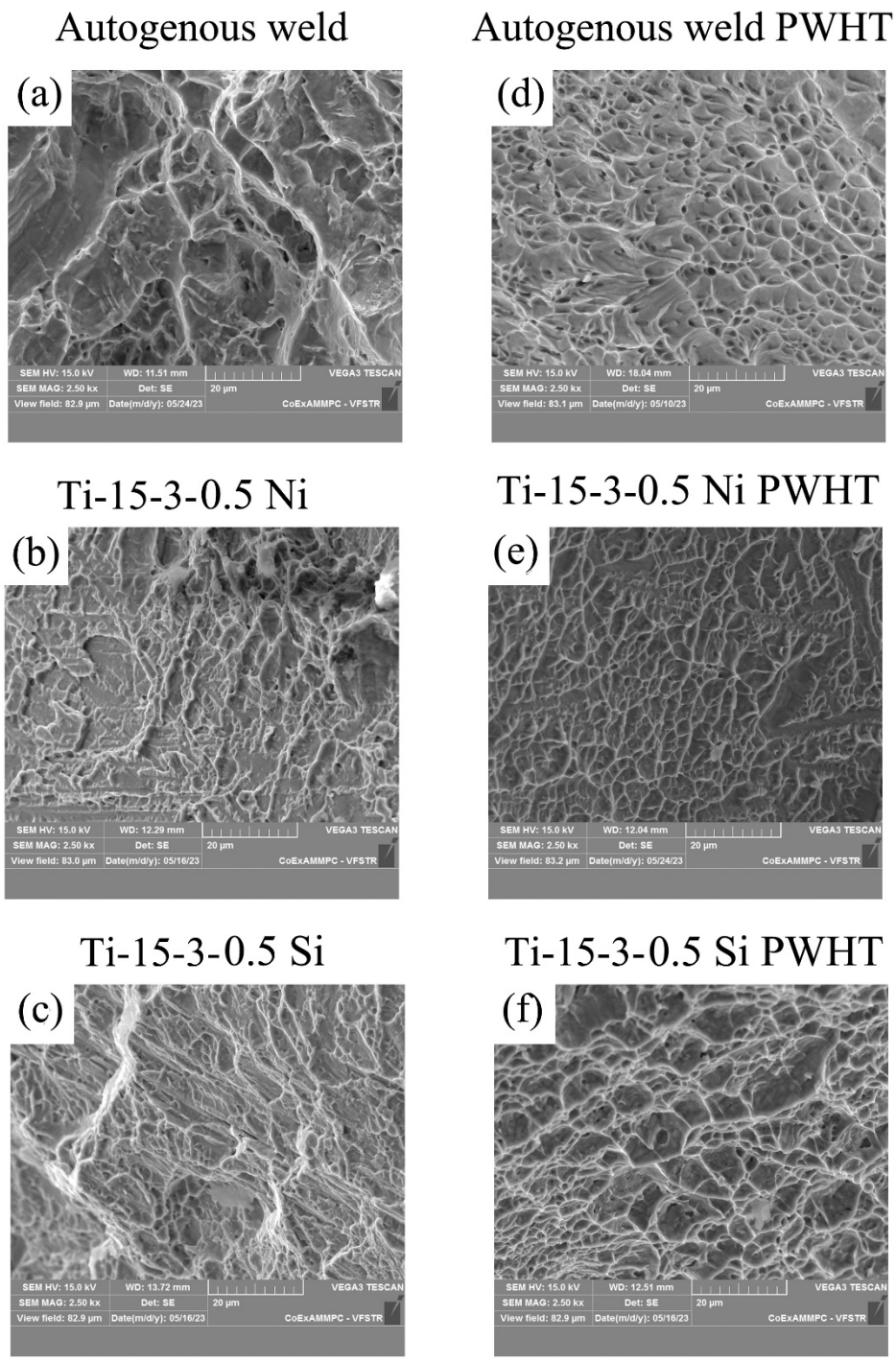

Fig 6.15: The Fracture surfaces of GTA (a) autogenous weld (b) Ti-15-3-0.5 Ni filler weld and (c) Ti-15-3-0.5 Si filler weld in the as-welded condition; (d-f) respective welds in PWHT condition.

7. CONCLUSIONS

Based on the results obtained in the present study on Ti-15-3 weldments, the following conclusions were drawn.

1. In both GTAW and EBW processes, with an increased welding speed, the average width of the FZ decreased, which is due to lower heat input and higher welding speed.
2. The microstructure of FZ in both the welding processes consists of coarse columnar β grains. The width of these columnar β grains decreased with increased welding speed.
3. In both welding processes, the welds prepared with higher welding speed led to faster cooling rates, resulting in lower heat input, reducing the thermal gradient (G) and increasing the solidification rate (R), thereby greater constitutional supercooling; Hence more nuclei will survive thereby, resulting in fine equiaxed grains at the weld root and centre.
4. In EBW, the welds at 800 mm/min welding speed (higher speed) showed higher UTS (751 MPa), and hardness (245 HV) compared to welds prepared with 500 mm/min welding speed (lower speed) (UTS 670 MPa; hardness 235 HV). The higher strength at 800 mm/min welding can be attributed to the lower columnar width of β grains and the formation of equiaxed grains at the weld root and centre.
5. A similar trend is observed in GTAW, the welds at 25 cm/min welding speed (higher speed) showed higher UTS (654 ± 5 MPa) and hardness (240 HV) compared to 15 cm/min welding speed (lower speed) (UTS 593 ± 5 MPa; hardness 230 HV).
6. However, the Ti-15-3 BM showed good ductility and strength values compared with all the as-welded samples due to fine equiaxed grains and cold worked microstructure.
7. The welds prepared using Ti-15-3-0.5 Ni and Ti-15-3-0.5 Si fillers exhibited equaixed grains while solidification, primarily due to higher constitutional supercooling caused by the low solubility of these solutes (Ni and Si) in Ti. This refinement can be attributed to the growth restriction mechanism resulting from the partitioning of Ni and Si during solidification. In contrast, the autogenous welds and welds prepared displayed columnar solidification.
8. The welds produced using Ti-15-3-0.5 Ni filler and Ti-15-3-0.5 Si filler showed higher strength compared to autogenous weld. The higher strength at welds prepared with Ti-15-3-0.5 Ni filler and Ti-15-3-0.5 Si filler can be attributed to the reduced columnar width of β grains and the development of equiaxed grains in the FZ.

9. The welds prepared with modified filler exhibited a reduction in ductility compared to autogenous weld. This decrease in ductility can be attributed to the embrittlement caused by the significant presence of Ti-Ni and Ti-Si precipitates along the grain boundaries.
10. All welds subjected to PWHT showed higher YS and UTS than as-welded samples because of the uniform precipitation of α-phase in a matrix of β grains. The precipitation of the α phase in the PWHT samples has been confirmed through TEM analysis.

8. SUGGESTIONS FOR FUTURE WORK

1. Exploring the other welding parameters like arc manipulation, vibrational techniques, and electromagnetic stirring may also result in modifying the microstructure of Ti alloys.

2. Studying the grain restriction mechanism of Ti alloy welds by the addition of various elements like Sc, La, Zr, etc., which may also result in a β grain refinement in FZ.

3. Subjecting to different post-weld aging conditions of weldments may result in a higher density of finer size α in the weldments, providing higher strength and ductility.

REFERENCES:

[1] H. Inoue, "Welding and joining of titanium and titanium alloys," *Welding International*, vol. 10, no. 2, pp. 160–163, 1996, doi: 10.1080/09507119609548973.

[2] A. B. Short, "Gas tungsten arc welding of α + β titanium alloys: A review," *Materials Science and Technology*, vol. 25, no. 3, pp. 309–324, 2009, doi: 10.1179/174328408X389463.

[3] A. Safdar, L. Y. Wei, A. Snis, and Z. Lai, "Evaluation of microstructural development in electron beam melted Ti-6Al-4V," *Materials Characterization*, vol. 65, no. Dld, pp. 8–15, 2012, doi: 10.1016/j.matchar.2011.12.008.

[4] R. I. Jaffee, "General Physical Metallurgy of Titanium Reviewed," *Jom*, vol. 7, no. 2, pp. 247–252, 1955, doi: 10.1007/bf03377488.

[5] J. D. Cotton *et al.*, "State of the Art in Beta Titanium Alloys for Airframe Applications," vol. 67, no. 6, pp. 1281–1303, 2015, doi: 10.1007/s11837-015-1442-4.

[6] B. J. Kutelu, S. O. Seidu, G. I. Eghabor, and A. I. Ibitoye, "Review of GTAW Welding Parameters," pp. 541–554, 2018, doi: 10.4236/jmmce.2018.65039.

[7] R. P. Naik, M. Samatham, and H. Kumar, "Review on different welding techniques of Titanium and its alloys," no. March, 2020, doi: 10.32628/IJSRSET207150.

[8] M. Balasubramanian, V. Jayabalan, and V. Balasubramanian, "Effect of pulsed current gas tungsten arc welding parameters on microstructure of titanium alloy welds," *Journal of Manufacturing Science and Engineering, Transactions of the ASME*, vol. 131, no. 6, pp. 0645021–0645024, 2009, doi: 10.1115/1.4000373.

[9] N. K. Babu, S. G. S. Raman, C. V. S. Murthy, and G. M. Reddy, "Effect of beam oscillation on fatigue life of Ti-6Al-4V electron beam weldments," *Materials Science and Engineering A*, vol. 471, no. 1–2, pp. 113–119, 2007, doi: 10.1016/j.msea.2007.03.040.

[10] X. Cao and M. Jahazi, "Effect of welding speed on butt joint quality of Ti-6Al-4V alloy welded using a high-power Nd:YAG laser," *Optics and Lasers in Engineering*, vol. 47, no. 11, pp. 1231–1241, 2009, doi: 10.1016/j.optlaseng.2009.05.010.

[11] V. Subravel, G. Padmanaban, and V. Balasubramanian, "Effect of welding speed on microstructural characteristics and tensile properties of GTA welded AZ31B magnesium alloy," *Transactions of Nonferrous Metals Society of China (English Edition)*, vol. 24, no. 9, pp. 2776–2784, 2014, doi: 10.1016/S1003-6326(14)63409-9.

[12] S. To, T. H. E. Welding, and B. Y. R. W. Messler, "Electron Beam Weldability of Advanced Titanium Alloys," no. May, pp. 79–84, 1981.

[13] R. R. Boyer and R. D. Briggs, "The use of β titanium alloys in the aerospace industry," *Journal of Materials Engineering and Performance*, vol. 14, no. 6, pp. 681–685, 2005, doi: 10.1361/105994905X75448.

[14] W. A. B. I. I. I. P. S. Liu and T. Paskellt, "Weld Solidification and HAZ Liquation in a Metastable-Beta Titanium AIIoy-Beta-21S," vol. 154, pp. 147–154, 1993.

[15] R. W. Messler, "Electronic Beam Weldability of Advanced Titanium Alloys.," *Welding Journal (Miami, Fla)*, vol. 60, no. 5, pp. 79–84, 1981.

[16] K. Balachandar, V. S. Sarma, and B. Pant, "Microstructure and Mechanical Properties of Gas-Tungsten- Arc – Welded Ti-15-3 Beta Titanium Alloy," vol. 40, no. November, pp. 2685–2693, 2009, doi: 10.1007/s11661-009-9952-8.

[17] T. Pasang, Y. Tao, F. J. Botana, J. C. Sabol, W. Z. Misiolek, and O. Kamiya, "Comparison of Ti-5Al-5V-5Mo-3Cr welds performed by LBW , EBW and GTAW," no. June, pp. 3–9, 2013.

[18] J. M. Oh *et al.*, "Grain refinement and hardness increase of titanium via trace element addition," *Materials Transactions*, vol. 51, no. 11, pp. 2009–2012, 2010, doi: 10.2320/matertrans.M2010175.

[19] M. J. Bermingham, S. D. McDonald, D. H. StJohn, and M. S. Dargusch, “Beryllium as a grain refiner in titanium alloys,” *Journal of Alloys and Compounds*, vol. 481, no. 1–2, pp. 20–23, 2009, doi: 10.1016/j.jallcom.2009.03.016.
[20] M. J. Bermingham, S. D. McDonald, M. S. Dargusch, and D. H. StJohn, “The mechanism of grain refinement of titanium by silicon,” *Scripta Materialia*, vol. 58, no. 12, pp. 1050–1053, 2008, doi: 10.1016/j.scriptamat.2008.01.041.
[21] M. J. Bermingham, S. D. McDonald, K. Nogita, D. H. St. John, and M. S. Dargusch, “Effects of boron on microstructure in cast titanium alloys,” *Scripta Materialia*, vol. 59, no. 5, pp. 538–541, 2008, doi: 10.1016/j.scriptamat.2008.05.002.
[22] I. Adli *et al.*, “Effects of Boron and Carbon Added Titanium Filler on Microstructure and Mechanical Properties of Ti-15-3 Alloy Weldments,” vol. 7, pp. 538–543, 2018.
[23] T. Deng, S. Li, Y. Liang, L. Sun, and Y. Zhang, “Effects of scandium and silicon addition on the microstructure and mechanical properties of Ti-6Al-4V alloy,” *Journal of Materials Research and Technology*, vol. 9, no. 3, pp. 5676–5688, 2020, doi: 10.1016/j.jmrt.2020.03.092.
[24] H. C. Lin and L. M. Wang, “Improved mechanical properties of Ti – 15V – 3Cr – 3Sn – 3Al alloy by electron beam welding process plus heat treatments and its microstructure evolution,” *Materials Chemistry and Physics*, vol. 126, no. 3, pp. 891–897, 2011, doi: 10.1016/j.matchemphys.2010.12.019.
[25] W. A. B. Iii, D. W. Becker, and F. H. Froes, “Advances in Titanium Alloy Welding Metallurgy,” no. May, pp. 46–58, 1984.
[26] N. Yumak and K. Aslantaş, “Effect of Heat Treatment Procedure on Mechanical Properties of Ti-15V-3Al-3Sn-3Cr Metastable β Titanium Alloy,” *Journal of Materials Engineering and Performance*, vol. 30, no. 2, pp. 1066–1074, 2021, doi: 10.1007/s11665-020-05445-x.
[27] N. Yumak, K. Aslantaş, and A. Çetkin, “Cryogenic and aging treatment effects on the mechanical properties of Ti-15V3Al-3Cr-3Sn titanium alloy,” *Journal of Testing and Evaluation*, vol. 49, no. 5, 2020, doi: 10.1520/JTE20200078.
[28] N. Yumak and K. Aslantaş, “Effect of Heat Treatment Procedure on Mechanical Properties of Ti-15V-3Al-3Sn-3Cr Metastable β Titanium Alloy,” *Journal of Materials Engineering and Performance*, vol. 30, no. 2. pp. 1066–1074, 2021. doi: 10.1007/s11665-020-05445-x.
[29] T. Kuroda, F. Matsuda, and I. Iwagi, “Effects of two - step ageing and thermomechanical treatments on age - hardening properties of welded β titanium alloy Effects of two-step ageing and thermomechanical treatments on age-hardening properties of welded β titanium alloy,” vol. 7116, no. June, 2016, doi: 10.1080/09507119409548536.
[30] R. Santhosh, M. Geetha, V. K. Saxena, and M. Nageswararao, “Studies on single and duplex aging of metastable beta titanium alloy Ti-15V-3Cr-3Al-3Sn,” *Journal of Alloys and Compounds*, vol. 605, pp. 222–229, 2014, doi: 10.1016/j.jallcom.2014.03.183.
[31] J. C. Lütjering, G. and Williams, *Titanium*. 2014. doi: 10.1016/B978-0-12-386454-3.00942-8.
[32] M. J. Bermingham, S. D. McDonald, M. S. Dargusch, and D. H. StJohn, “MIcrostucture of cast titanium alloys,” *Materials Forum*, vol. 31, no. January 2007, pp. 84–89, 2007.
[33] X. Wu, “Review of alloy and process development of TiAl alloys,” *Intermetallics*, vol. 14, no. 10–11, pp. 1114–1122, 2006, doi: 10.1016/j.intermet.2005.10.019.
[34] H. Matsumoto, S. Watanabe, and S. Hanada, “α′ Martensite Ti-V-Sn alloys with low Young’s modulus and high strength,” *Materials Science and Engineering: A*, vol. 448, no. 1–2, pp. 39–48, 2007, doi: 10.1016/j.msea.2006.11.022.

[35] H. Okamoto, “Sn-Ti (tin-titanium),” *Journal of Phase Equilibria and Diffusion*, vol. 31, no. 2, pp. 202–203, 2010, doi: 10.1007/s11669-010-9663-2.
[36] H. C. Hsu, S. C. Wu, Y. S. Hong, and W. F. Ho, “Mechanical properties and deformation behavior of as-cast Ti-Sn alloys,” *Journal of Alloys and Compounds*, vol. 479, no. 1–2, pp. 390–394, 2009, doi: 10.1016/j.jallcom.2008.12.064.
[37] B. Soediono, *Titanium: Physical Metallurgy Processing and Application*, vol. 53. 1989.
[38] M. Q. Ian Polmear, David StJohn, Jian-Feng Nie, *Light alloys meturgy of light metals*. doi: 10.1016/B978-0-08-099431-4.00007-5.
[39] L. Bolc, R. Tadeusiewicz, L. J. Chmielewski, and K. Wojciechowski, “Preface,” *Lecture Notes in Computer Science (including subseries Lecture Notes in Artificial Intelligence and Lecture Notes in Bioinformatics)*, vol. 7594 LNCS, no. September 2014, 2012, doi: 10.1007/978-3-642-33564-8.
[40] S. K. Kim and J. K. Park, “In-situ measurement of continuous cooling β → α transformation behavior of CP-Ti,” *Metallurgical and Materials Transactions A: Physical Metallurgy and Materials Science*, vol. 33, no. 4, pp. 1051–1056, 2002, doi: 10.1007/s11661-002-0206-2.
[41] M. J. Donachie, *Titanium - A Techincal Guide*, vol. 99, no. 5. 2000.
[42] J. A. Ballor, T. Li, F. Prima, C. J. Boehlert, and A. Devaraj, “A review of the metastable omega phase in beta titanium alloys: the phase transformation mechanisms and its effect on mechanical properties,” *International Materials Reviews*, vol. 68, no. 1, pp. 26–45, 2023, doi: 10.1080/09506608.2022.2036401.
[43] T. S. Kuan, R. R. Ahrens, and S. L. Sass, “The Stress-induced omega phase transformation in Ti-V alloys,” *Metallurgical Transactions A*, vol. 6, no. 9, pp. 1767–1774, 1975, doi: 10.1007/BF02642306.
[44] M. P. Christoph Leyens, *Titanium and titanium alloys*. 2018. doi: 10.1007/978-3-319-69743-7_7.
[45] R. P. Kolli and A. Devaraj, “A review of metastable beta titanium alloys,” *Metals*, vol. 8, no. 7, pp. 1–41, 2018, doi: 10.3390/met8070506.
[46] R. Santhosh, M. Geetha, and M. Nageswara Rao, “Recent Developments in Heat Treatment of Beta Titanium Alloys for Aerospace Applications,” *Transactions of the Indian Institute of Metals*, vol. 70, no. 7, pp. 1681–1688, 2017, doi: 10.1007/s12666-016-0985-6.
[47] H. W. Rosenberg, “Ti-15-3 : A New Cold-Formable Sheet Titanium Alloy,” pp. 30–34, 1983.
[48] H. . and J. W. M. Kokanson, “Electron beam welding of aircraft materials and components,” *Welding journal*, vol. 41, pp. 999 – 1001, 1962.
[49] C. L. M. Cottrell, “Electron beam welding - a critical review,” *Materials and Design*, vol. 6, no. 6, pp. 285–291, 1985, doi: 10.1016/0261-3069(85)90009-3.
[50] M. Çam, G., Dos Santos, J. F., & Koçak, “Laser and Electron Beam Welding of Titianium Alloys,” *Laser and Electron Beam Welding of Titianium Alloys*, 1997, [Online]. Available: https://www.osti.gov/etdeweb/servlets/purl/595200
[51] S. Kou, *Welding Metallurgy*, vol. 4, no. 3. 1972. doi: 10.22486/iwj.v4i3.150243.
[52] B. Y. D. W. Becker, “Investigation of Pulsed GTA W e l d i n g Parameters,” 1978.
[53] G. H. Mcelhinney and E. L. Pruitt, “An Investigation of Pulsed GTA Welding Variables”.
[54] N. K. Babu and S. G. S. Raman, “Influence of current pulsing on microstructure and mechanical properties of Ti-6Al-4V TIG weldments,” *Science and Technology of Welding and Joining*, vol. 11, no. 4, pp. 442–447, 2006, doi: 10.1179/174329306X120750.
[55] P. K. Palani and N. Murugan, “Selection of parameters of pulsed current gas metal arc

welding," vol. 172, pp. 1–10, 2006, doi: 10.1016/j.jmatprotec.2005.07.013.
[56] W. Unkel, "Arc and Weld Pool Behavior for Pulsed Current GTAW High-frequency current pulsing can be used to control the".
[57] S. Kou and Y. Le, "Welding Parameters and the Grain Structure of Weld Metal - a Thermodynamic Consideration.," *Metallurgical transactions. A, Physical metallurgy and materials science*, vol. 19 A, no. 4, pp. 1075–1082, 1988, doi: 10.1007/bf02628392.
[58] J. C.Lippold, *Welding metallurgy and weldability*.
[59] J. Xiong, S. Li, F. Gao, and J. Zhang, "Microstructure and mechanical properties of Ti6321 alloy welded joint by GTAW," *Materials Science and Engineering A*, vol. 640, pp. 419–423, 2015, doi: 10.1016/j.msea.2015.06.022.
[60] N. Kishore Babu, S. Ganesh Sundara Raman, R. Mythili, and S. Saroja, "Correlation of microstructure with mechanical properties of TIG weldments of Ti-6Al-4V made with and without current pulsing," *Materials Characterization*, vol. 58, no. 7, pp. 581–587, 2007, doi: 10.1016/j.matchar.2006.07.001.
[61] "Postweld Heat Treatment of GTA Welds in a High-Strength Metastable Titanium Alloy-Beta-CTM," pp. 469–476, 1993.
[62] S. Mishra and T. DebRoy, "Measurements and Monte Carlo simulation of grain growth in the heat-affected zone of Ti-6Al-4V welds," *Acta Materialia*, vol. 52, no. 5, pp. 1183–1192, 2004, doi: 10.1016/j.actamat.2003.11.003.
[63] G. J. Davies and J. G. Garland, "Solidification Structures and Properties of Fusion Welds," vol. 20, 1975.
[64] F. Karimzadeh, M. Salehi, A. Saatchi, and M. Meratian, "Effect of microplasma arc welding process parameters on grain growth and porosity distribution of thin sheet Ti6Al4V alloy weldment," *Materials and Manufacturing Processes*, vol. 20, no. 2, pp. 205–219, 2005, doi: 10.1081/AMP-200041857.
[65] T. Mohandas and G. Madhusudan Reddy, "Effect of frequency of pulsing in gas tungsten arc welding on the microstructure and mechanical properties of titanium alloy welds: A technical note," *Journal of Materials Science Letters*, vol. 15, no. 7, pp. 626–628, 1996, doi: 10.1007/BF00579271.
[66] C. O. and T. F. B. Poorganji, A. Kazahari, T. Narushima, "Effect of yttrium addition on grain growth of α, β and α+β titanium alloys .pdf."
[67] C. Li, D. Lee, X. Mi, W. Ye, S. Hui, and Y. Lee, "Effect of Al Addition on ω Precipitation and Age Hardening of Ti-Al-Mo-Fe Alloys," *Metallurgical and Materials Transactions A*, vol. 47, no. 5, pp. 2454–2461, 1954, doi: 10.1007/s11661-016-3386-x.
[68] Y. Ohmori, T. Ogo, K. Nakai, and S. Kobayashi, "Effects of ω -phase precipitation on β to α , α" transformations in a metastable β titanium alloy," vol. 312, pp. 182–188, 2001.
[69] O. B. A.W.Sommer, S.Motokura, K.Ono, "relaxation process in metastable beta titanium alloys".
[70] H. P. Ng, E. Douguet, C. J. Bettles, and B. C. Muddle, "Age-hardening behaviour of two metastable beta-titanium alloys," vol. 527, pp. 7017–7026, 2010, doi: 10.1016/j.msea.2010.07.055.
[71] C. Angelier, S. Bein, and J. Be, "Building a Continuous Cooling Transformation Diagram of NL - CEZ Alloy by Metallography and Electrical Resistivity Measurements," 1997.
[72] W. A. B. Iii, "Cooling Rate Effects in Ti-6AI-2Sn-4Zr-2Mo Weldments," vol. 15, no. OCTOBER, pp. 3–7, 1984.
[73] M. J. Bermingham, D. H. StJohn, J. Krynen, S. Tedman-Jones, and M. S. Dargusch,

"Promoting the columnar to equiaxed transition and grain refinement of titanium alloys during additive manufacturing," *Acta Materialia*, vol. 168, pp. 261–274, 2019, doi: 10.1016/j.actamat.2019.02.020.
[74] A. Sattar *et al.*, "Optimization of TIG Welding Parameters for Ti-6Al-4V Titanium Alloy using the Taguchi Design of Experiment," *NUST Journal of Engineering Sciences*, vol. 15, no. 2, pp. 22–34, 2022, doi: 10.24949/njes.v15i2.731.
[75] C. J. Tsai and L. M. Wang, "Improved mechanical properties of Ti-6Al-4V alloy by electron beam welding process plus annealing treatments and its microstructural evolution," *Materials and Design*, vol. 60, pp. 587–598, 2014, doi: 10.1016/j.matdes.2014.04.037.
[76] D. Hallum and W. Baeslack, "Nature of grain refinement in titanium alloy welds by microcooler inoculation," *Welding Journal*, vol. 9, no. September, pp. 326–336, 1990.
[77] S. Sundaresan, G. D. Janaki Ram, and G. Madhusudhan Reddy, "Microstructural refinement of weld fusion zones in α-β titanium alloys using pulsed current welding," *Materials Science and Engineering A*, vol. 262, no. 1–2, pp. 88–100, 1999, doi: 10.1016/s0921-5093(98)01010-7.
[78] S. Rohatgi, M. Tiwari, A. Rathi, and A. Sharma, "Role of Undercooling and Effect of Solute Particles on Grain Refinement of Aluminium Alloys," *Indian Foundry Journal*, vol. 61, no. 2, pp. 31–37, 2015.
[79] X. Zhan, Q. Peng, Y. Wei, and W. Ou, "Experimental and simulation study on the microstructure of TA15 titanium alloy laser beam welded joints," vol. 94, pp. 279–289, 2017.
[80] P. S. Liu, W. A. Baeslack, and J. Hurley, "Dissimilar alloy laser beam welding of titanium. Ti-6Al-4V to beta-C," *Welding Journal (Miami, Fla)*, pp. 175–181, 1994.
[81] I. A. M. Arif, M. K. Talari, A. L. Anis, M. H. Ismail, and N. Kishore Babu, "Grain Refinement, Microstructural and Hardness Investigation of C Added Ti-15-3 Alloys Prepared by Argon Arc Melting," *Transactions of the Indian Institute of Metals*, vol. 70, no. 3, pp. 861–865, 2017, doi: 10.1007/s12666-017-1048-3.
[82] A. Lutfi, A. Mahesh, K. Talari, I. Adli, M. Arif, and N. K. Babu, "Microstructure and Mechanical Properties of Ti-15-3 Alloy Gas Tungsten Arc Welds Prepared Using CP-Titanium Filler," *Transactions of the Indian Institute of Metals*, vol. 70, no. 3, pp. 685–690, 2017, doi: 10.1007/s12666-017-1049-2.
[83] M. J. Bermingham, S. D. McDonald, M. S. Dargusch, and D. H. St.John, "Grain-refinement mechanisms in titanium alloys," *Journal of Materials Research*, vol. 23, no. 1, pp. 97–104, 2008, doi: 10.1557/jmr.2008.0002.
[84] M. J. Bermingham, S. D. McDonald, D. H. StJohn, and M. S. Dargusch, "Segregation and grain refinement in cast titanium alloys," *Journal of Materials Research*, vol. 24, no. 4, pp. 1529–1535, 2009, doi: 10.1557/jmr.2009.0173.
[85] M. Bermingham, "Grain refinement of cast titanium alloys," The university of queensland, 2009.
[86] D. Cascadan and C. R. Grandini, "Structure, Microstructure, and Some Selected Mechanical Properties of Ti-Ni Alloys," in *Recent Advances in Engineering Materials and Metallurgy*, 2019.
[87] S. Hellberg, J. Hummel, P. Krooß, T. Niendorf, and S. Böhm, "Microstructural and mechanical properties of dissimilar nitinol and stainless steel wire joints produced by micro electron beam welding without filler material," *Rivista Italiana della Saldatura*, vol. 73, no. 4, pp. 449–463, 2021.
[88] J. Seretsky and E. R. Ryba, "Laser Welding of Dissimilar Metals: Titanium To Nickel.," *Welding Journal (Miami, Fla)*, vol. 55, no. 7, 1976.
[89] S. Sui, Y. Chew, F. Weng, C. Tan, Z. Du, and G. Bi, "Achieving grain refinement and ultrahigh yield strength in laser aided additive manufacturing of Ti−6Al−4V alloy by

trace Ni addition," *Virtual and Physical Prototyping*, vol. 16, no. 4, pp. 417–427, 2021, doi: 10.1080/17452759.2021.1949091.
[90] M. Fiore, F. B. Neto, and C. R. de F. Azevedo, "Assessment of the Ti-rich corner of the Ti-Si phase diagram using two sublattices to describe the Ti5Si3 phase," *Revista Escola de Minas*, vol. 70, no. 2, pp. 201–207, 2017, doi: 10.1590/0370-44672016700073.
[91] S. Sabooni, F. Karimzadeh, and M. H. Abbasi, "Thermodynamic aspects of nanostructured Ti 5Si 3 formation during mechanical alloying and its characterization," *Bulletin of Materials Science*, vol. 35, no. 3, pp. 439–447, 2012, doi: 10.1007/s12034-012-0298-2.
[92] K. M. Ibrahim, A. H. Hussein, and M. Abdelkawy, "Effect of Si-addition as a grain refiner on microstructure and properties of Ti-6Al-4V Alloy," *Transactions of Nonferrous Metals Society of China (English Edition)*, vol. 23, no. 7, pp. 1863–1874, 2013, doi: 10.1016/S1003-6326(13)62671-0.
[93] A. Lut *et al.*, "Grain re fi nement of Ti-15V-3Cr-3Sn-3Al metastable b titanium alloy welds using boron-modi fi ed fi llers," vol. 749, pp. 320–328, 2018, doi: 10.1016/j.jallcom.2018.03.286.
[94] S. Mereddy, M. J. Bermingham, D. H. StJohn, and M. S. Dargusch, "Grain refinement of wire arc additively manufactured titanium by the addition of silicon," *Journal of Alloys and Compounds*, vol. 695, pp. 2097–2103, 2017, doi: 10.1016/j.jallcom.2016.11.049.
[95] R. S. Funderburk, "Postweld Heat Treatment," *Welding innovation*, vol. XV, no. 2, 1998.
[96] M. P. M.A.Greenfield, "Postweld Aging of a Metastable Beta Titanium Alloy".
[97] W. A. B. I. D.W.Becker, "Property-Microstructure Relationships in Metastable-Beta Titanium Alloy Weldments," vol. 124, no. 855, pp. 85–92.
[98] P. Taylor, T. Kuroda, F. Matsuda, and I. Iwaki, "Effects of ageing treatment on hardening characteristics in the HAZ of beta - type Effects of ageing treatment on hardening characteristics in the HAZ of beta-type Ti-15V-3Cr-3Sn-3AI alloy welds," no. January 2015, pp. 37–41, 2009, doi: 10.1080/09507119209548321.
[99] C. Fu, Y. Wang, S. He, C. Zhang, and X. Jing, "Microstructural characterization and mechanical properties of TIG weld joint made by forged Ti–4Al–2V alloy," *Materials Science and Engineering A*, vol. 821, no. June, p. 141604, 2021, doi: 10.1016/j.msea.2021.141604.
[100] S. H. Wang and M. D. Wei, "Tensile properties of gas tungsten arc weldments in commercially pure titanium, Ti-6Al-4V and Ti-15V-3Al-3Sn-3Cr alloys at different strain rates," *Science and Technology of Welding and Joining*, vol. 9, no. 5, pp. 415–422, 2004, doi: 10.1179/136217104225021599.
[101] J. C. Sabol, T. Pasang, W. Z. Misiolek, and J. C. Williams, "Journal of Materials Processing Technology Localized tensile strain distribution and metallurgy of electron beam welded Ti – 5Al – 5V – 5Mo – 3Cr titanium alloys," *Journal of Materials Processing Tech.*, vol. 212, no. 11, pp. 2380–2385, 2012, doi: 10.1016/j.jmatprotec.2012.06.023.
[102] T. Pasang, Y. Tao, M. Azizi, O. Kamiya, M. Mizutani, and W. Misiolek, "Welding of titanium alloys," *MATEC Web of Conferences*, vol. 123, pp. 1–8, 2017, doi: 10.1051/matecconf/201712300001.
[103] R. Santhosh, M. Geetha, V. K. Saxena, and M. N. Rao, "Effect of duplex aging on microstructure and mechanical behavior of beta titanium alloy Ti – 15V – 3Cr – 3Al – 3Sn under unidirectional and cyclic loading conditions," *INTERNATIONAL JOURNAL OF FATIGUE*, vol. 73, pp. 88–97, 2015, doi: 10.1016/j.ijfatigue.2014.12.005.
[104] W. Ting, Z. Bing-gang, and C. Guo-qing, "Electron beam welding of Ti-15-3 titanium

alloy to 304 stainless steel with copper interlayer sheet," *Transactions of Nonferrous Metals Society of China*, vol. 20, no. 10, pp. 1829–1834, 2010, doi: 10.1016/S1003-6326(09)60381-2.

[105] C. J. Marvel, J. C. Sabol, T. Pasang, M. Watanabe, and W. Z. Misiolek, "Improving the Mechanical Properties of the Fusion Zone in Electron-Beam Welded Ti-5Al-5Mo-5V-3Cr Alloys," *Metallurgical and Materials Transactions A: Physical Metallurgy and Materials Science*, vol. 48, no. 4, pp. 1921–1930, 2017, doi: 10.1007/s11661-017-3968-2.

[106] A. Muthuchamy, M. Rajadurai, A. R. Annamalai, and D. K. Agrawal, "Effect of Nickel Addition on Microstructure and Mechanical Properties of the Spark Plasma Sintered Ti–6Al–4V Alloy," *Transactions of the Indian Institute of Metals*, vol. 72, no. 8, pp. 2127–2134, 2019, doi: 10.1007/s12666-018-1550-2.

LIST OF PUBLICATIONS

1. **K. Vamsi Krishna**, M. K. Talari, Bharath Bandi, Sriharitha Rowthu, M. I. Khan, P. Mastanaiah, and N. Kishore Babu, "Effect of welding speed on microstructural and mechanical properties of EB Ti-15V-3Al-3Cr-3Sn welds", **Materials Science and Technology**, 39(11), 1402-1413 (2023) (Impact factor: 2.060).

2. **K. Vamsi Krishna,** Sriharitha Rowthu, Vijay N. Nadakuduru, Ganesh Pilla and N. Kishore Babu**,** "Effect of Welding Speed and Postweld Heat Treatment on Microstructural Characterization and Mechanical Properties of Gas Tungsten Arc Welded Ti-15V-3Al-3Cr-3Sn Joints", **Fusion Science and Technology**, 1-14 (2023). (Impact factor: 1.235).

3. **K. Vamsi Krishna,** Gopi Krishna C, Ateekh Ur Rehman, Kishore Babu Nagumothu, Mahesh Kumar Talari and Prakash Srirangam**,** "Effect of Welding Speed and Post-Weld Heat Treatment on Microstructural and Mechanical Properties of Alpha+Beta Titanium Alloy EB Weld"**, Fusion Science and Technology,** 1-12 (2023). (Impact factor: 1.235).

4. **K. Vamsi Krishna,** Gopi Krishna C, Nagendra Polamarasetty, Mahesh Kumar Talari, Vijay N. Nadakuduru & Kishore Babu Nagumothu**,** "Microstructural Characterization and Mechanical Properties of Metastable Beta and α+β Titanium Alloy Electron Beam Weldments", **Fusion Science and Technology,** 1-16 (2023). (Impact factor: 1.235).

International and national conferences:

1. Poster Presentation on "**Study on weld bead morphology of electron beam welded Ti-6Al-4V at different welding speeds**" under the "Non-Ferrous" theme in the Indian Institute of Metals 75 Annual technical meeting (**IIM ATM 2021**), held in online on 13 to 15 November 2021.

2. Poster Presentation on "**Experimental investigation on weld bead morphology of Ti-15V-3Al-3Cr-3Sn weldments using gas tungsten arc welding**" under the "Non-Ferrous" theme in the Indian Institute of Metals 76 Annual technical meeting (**IIM ATM 2022**), held at Ramoji film city, Hyderabad on 13 to 16 November 2022.

3. Paper presentation on "**Effect of welding speed and post-weld heat treatment on microstructural and mechanical properties of Ti-6Al-4V EB welds**" in "2nd International Conference on Advanced Materials and Manufacturing Processes (**ICAMMP-2023**)" during 3rd and 4th March 2023 organized by the department of Metallurgical Engineering, College of Engineering Vizianagaram, Jawaharlal Nehru Technological University Gurajada Vizianagaram, (JNTUGV), Andhra Pradesh, India